



TECHNISCHE UNIVERSITÄT
MÜNCHEN

DEPARTMENT OF PHYSICS

Dissertation

Molecular adsorption on *h*-BN

Domenik Matthias Zimmermann





TECHNISCHE UNIVERSITÄT MÜNCHEN

DEPARTMENT OF PHYSICS

Dissertation

Molecular adsorption on *h*-BN

Vollständiger Abdruck der von der Fakultät für Physik der Technischen Universität München zur Erlangung des akademischen Grades eines Doktors der Naturwissenschaften (Dr. rer. nat.) genehmigten Dissertation.

Author:	Domenik Matthias Zimmermann
Supervisor:	Prof. Dr. Wilhelm Auwärter
Submission Date:	TODO: Submission date
Chairman:	TODO: Chairman
1. Examiner:	TODO: 1. Examiner
2. Examiner:	TODO: 2. Examiner

I assure the single handed composition of this dissertation only supported by declared resources.

Munich, TODO: Submission date

Domenik Matthias Zimmermann

Acknowledgments

A lot of people are invoked in the course of the thesis and I like to thank them for their support. First and foremost I like to thank Prof. Dr. W. Auwärter for the opportunity to work in his research group. The wide field of molecular assembly and functionalization opened up many interesting insights that would never be possible without him. The time dedicated to experiments under his leadership was very exciting and his review challenged my ambition to further improve. Together with Prof. Dr. J. Barth a very pleasant professional environment was created with retreats and group activities framing our day-to-day work.

Besides them, many people were incorporated at different levels, starting from introducing technical aspects and measurement techniques used at the different setups via result discussion through to proof-reading and concept validation.

Dr. A. Wiengarten was the operator of the low temperature scanning tunneling microscope and I started under her supervision with the first measurements. Her profound understanding of the setup shared with me was consolidated by Dr. K. Seufert whose deep commitment nurtured my engagement. His enjoyment of work eased many hours in the lab.

Measurements at the low temperature atomic force microscope are supported by M. Pörtner and S. Synkule. Their fruitful result discussion together with Dr. A. Riss clarified topics in technical and scientific aspects easily.

The combined room temperature STM and X-Ray photoelectron spectroscopy setup was assembled by Dr. M. Schwarz whose continuous efforts in setup details enabled the use of this machine. Together with discussion and operational help of A. Baklanov, many measurements were done smoothly.

Further XPS measurements were done at the machine operated by the Nanosystems Initiative Munich represented by **LALALA** and advocated by Dr. J. Reichert. Scientific discussion with him, K. Eberle and Prof. Dr. Feulner often lead to meaningful outcomes and was always a pleasure.

The few measurements at the scanning electron microscope were done under supervision of Dr. P. Deimel and Y. Gong.

Please let me thank all member of E20 for a nice time together that showed me the value of social interaction combined with consuming delights and limits.

Thank you.

Dedicated to the beloved ones that made me who I am. Without you these endless lines of text would never end.

Abstract

Good quality, two dimensional, hexagonal boron nitride (*h*-BN) islands require a clean and flat surface to grow on. Techniques to chemically polish the surface are shortly reviewed. After polish the growth of sub-monolayer *h*-BN islands is investigated on poly crystalline copper surfaces by means of STM and XPS. The use of *h*-BN grown on polycrystalline copper foils as insulating and electronically decoupling substrate is shown by reproducing molecular adsorption known on *h*-BN grown on single crystalline copper.

Different molecular species are investigated with regard to their electronic properties and structures formed by self-assembly on metallic and insulating 2D *h*-BN substrates.

Bis- & Tetra-pyridin-4-ylethynyl functionalized pyrene molecules are adsorbed on *h*-BN/Cu(111) to show the diversity of self-assembled molecules structures that can be steered by the number and position of functional groups. It is shown that their opto-electronic properties and assembly after adsorption are well determined by the chemical design of the molecule and show the same trend as gas-phase calculations: An decrease in electronic band gap with increasing number of functional groups. Frontier orbital resolution in STM with modified tip conditions and a wide band gap in STS show efficient decoupling from the metallic substrate by the *h*-BN layer. It modifies the substrate surface potential, so that the band gap is changed locally in a well defined, periodic manner, following the periodicity of *h*-BN's superstructure on Cu(111).

Furthermore coronene molecules are used to determine the influence of a BN modified molecular center on the self-assembly and electronic structure on Ag(111) and Au(111) substrates and shows the importance of the side groups in the formation process of self-assembled structures. Investigation with nc-AFM is used to clarify sub-molecular structure and the formation of linked structures after annealing treatment in UHV.

Single and bis- nitro functionalized porphine molecules are adsorbed on Cu, Ag and *h*-BN/Cu(111). Additional di-tert-butyl-phenyl side groups are used to further decouple the molecule from the substrate layer and increase mobility at low temperatures. The molecular self-assembly is controlled by the number of functional groups, so that bis-functionalized molecules adsorbed on Ag(100) form superstructures with hexagonal symmetry, mismatching its 2-fold symmetric substrate symmetry.

Helicene molecules are used to investigate the influence of chiral properties in conjunction

Abstract

with a dipole moment introduced by functionalization with two cyano groups at the helicene's central carbon ring. Depending on the substrate, molecular assembly varies from chains formed with specific orientation to the metal substrate's high symmetry directions to dense packed islands formed after adsorption on *h*-BN/Cu(111). Annealing after adsorption on Ag resulted in a ring-closure reaction at the helicene's spiral terminations that lifts chirality.

At last a design for a peltier cooling unit is given, which is used to store liquids with a volume of severral mL at temperatures around 0 °C.

Contents

Acknowledgments	iii
Abstract	v
1. Introduction	1
2. Experimental methods	3
2.1. Scanning Tunneling Microscopy	3
2.1.1. An historic overview	3
2.1.2. Basic principles	4
2.1.3. Scanning Tunneling Spectroscopy	6
2.1.4. Machine description and experimental details	7
Experimental details	10
Limitations	11
2.2. X-ray Photoelectron Spectroscopy	15
2.2.1. Theory	15
2.2.2. Experimental details	17
2.2.3. Limitations	17
Beam damage	17
Space averaging technique	18
2.3. Atomic Force Microscopy	18
2.3.1. Theory	18
2.3.2. Experimental details	20
3. Substrates, ad layers and sample preparation	21
3.1. Substrates and adlayers	21
3.1.1. Single crystal substrates	21
3.1.2. Polycrystalline copper foils	23
3.1.3. <i>h</i> -BN	23
<i>h</i> -BN on Cu(111)	24
Stoichiometry	24
Moiré geometry	24

Periodic change in work function	26
3.1.4. Molecular assembly on <i>h</i> -BN	29
3.2. Sample preparation	30
3.2.1. Etching copper foils	30
Electrochemical cell	30
Aqueous etching solution	30
Redox reaction	32
Voltage-current-characteristic or polarization curve	33
Leveling mechanisms	34
After etching treatment and storage	35
3.2.2. Sample cleaning	35
3.2.3. <i>h</i> -BN growth	35
3.2.4. Molecule deposition	36
4. Epitaxial hexagonal boron nitride on copper foils	37
4.1. Pre-treatment of Cu-foils: Polishing	37
Experiment realization	37
4.1.1. RT-AFM	38
4.1.2. LT-STM characterization	39
4.1.3. SEM characterization	40
4.2. CVD-Growth of <i>h</i> -BN with borazine	42
4.2.1. LT-STM characterization	42
4.2.2. XPS characterization	43
Commercial <i>h</i> -BN sample	44
O1s	45
C1s	45
N1s/B1s	45
Cu3p	45
4.2.3. Application: Molecular adsorption of TPCN	46
4.3. Summary & Outlook	49
5. Pyridin-4-ylethynyl functionalized pyrene molecules on <i>h</i>-BN/Cu(111)	51
5.1. Abstract	51
5.2. Introduction	51
5.3. The molecule	53
5.4. Results & Discussion	54
5.5. Summary	62

5.6. Conclusion	63
6. Borazine functionalized coronene	65
6.1. Abstract	65
6.2. Introduction	65
6.3. The molecule	66
6.4. Results	68
6.4.1. On Ag(111)	68
6.4.2. On Au(111)	76
6.5. Summary & Discussion	77
7. Nitro functionalized Porphine	79
7.1. Abstract	79
7.2. Introduction	79
7.3. The molecule	80
7.4. Results: Single leg functionalization	81
7.4.1. on Cu(111)	81
“head-to-head”	81
“head-to-tail”	83
Flexible tert-butyl-groups	83
7.4.2. on Ag(111)	83
Annealing	84
Assembly	84
Flexible Tert-Butyl-Functions	86
Spectroscopy	86
7.4.3. on <i>h</i> -BN	86
<i>h</i> -BN grown on Cu(111)	86
<i>h</i> -BN grown on Cu-foil	86
7.5. Results: Double leg functionalization	87
7.5.1. on Cu(111)	87
7.5.2. on Ag(100)	90
Unit cell	90
Molecular orientation	91
Contrast within single molecule	91
Domain boundaries	91
7.6. Summary & Discussion	95
7.7. Conclusion	95

8. Cyano functionalized helicene molecules on Ag(111), Ag(100) and <i>h</i>-BN supports	97
8.1. Abstract	97
8.2. Introduction	97
8.3. The molecule	99
8.4. Results & discussion	101
8.4.1. on Ag(111)	101
8.4.2. on <i>h</i> -BN on Cu(111)	103
8.4.3. on Ag(100)	103
8.4.4. Molecular orbital energy shift and tip-dipole	106
8.5. Conclusions	110
Appendices	110
A. Polycrystalline copper foils	111
A.1. Surface structure of <i>h</i> -BN on Cu-foil	113
B. Pyrene	117
B.1. Extended Hückel theory calculations	123
C. TBP	129
C.1. How to determine molecules' distance	129
C.2. Ordered areas	130
C.3. TBP on Ag(100) - Symmetry relations	130
D. HBBNC	131
D.1. Extended Hückel theory calculations	138
E. Helicene	141
F. Peltier cooling unit	145
Bibliography	145

1. Introduction

Science strives to achieve more and more detailed information on matter at the smallest length scales. Understanding interaction between atoms and molecules resulted in the development of applications in sizes that would never be reached by engineers without applying the knowledge gained by foundational research. These applications are used in our every day life, often behind the scenes without need of the consumer knowing the physical details (LED lights, self-cleaning window glasses, gas sensors to detect explosives or harmful gas concentrations with very low detection levels (down to low ppm concentrations)).

While atomically precise structures were created by single atom manipulation [1] this process is not applicable at larger scales. Here the forces between adsorbates and between adsorbate and substrate is used to form regular structures. Inter-molecular links are specified by the chemical design of the molecule and result in structures that assemble themselves without the need to manipulate every single molecule with the STM tip.

Metal substrates interact with the molecules and influence electronic properties and molecular assembly. An investigation of these properties can be decoupled from the substrate by introducing a insulating layer to adsorb the molecules on. Development of on surface synthesis on metal substrates lead to 2D-materials like *h*-BN that show wide band gap insulating properties. This is used here to electronically decouple the molecule from the metal substrate.

Molecular chemistry evolved to a point where molecules can be designed on the drawing table and synthesized with demanded properties so that assembly at atomic level is predetermined by synthesis.

This work is placed at the interface between chemistry and computational physics to provide experimental insights into molecular interactions present at atomic levels that are used to benchmark theoretical calculations.

2. Experimental methods

Several experimental methods are used within this work to determine different physical properties. All of them are well known in surface science and used to analyze thin films on different substrates with respect to their geometric, electronic and chemical properties. In this chapter the principles, benefits and limitations for scanning tunneling microscopy (section 2.1), X-Ray photoelectron spectroscopy (section 2.2) and atomic force microscopy (section 2.3) are reviewed.

2.1. Scanning Tunneling Microscopy

The tunneling effect occurs when a particle faces a potential barrier. In the classical picture the particle is prohibited to move across the potential barrier if the particle's energy is lower than the barrier height. In quantum mechanics however, the particle is described as wave. When this now faces the potential barrier, a fraction of the wave package is transmitted through the barrier - an effect called tunneling.

2.1.1. An historic overview

The tunneling effect was first observed by Hund in 1926 in molecules, where he explained the sharing of an electron between atoms, each separated by a potential well.[2] A principle fundamental for an understanding of covalent chemical bonds.

The first quantitative expression of the tunneling current between two vacuum separated metals was introduced by Bardeen in 1961.[3]

This lead to an early experiment build by Russell Young, John Ward and Fredric Scire in 1972.[4] Here tunneling with metal tip was shown already. The concept was further improved by Binning & Rohrer in 1981 when they were the first to report experimental evidence for the tunneling through an vacuum gap.[5] They showcased the excelled resolution capabilities by resolving the (7×7) reconstruction of the Si(111) surface [6] and received the noble prize in 1986 for "their design of the scanning tunneling microscope" (STM).[7]

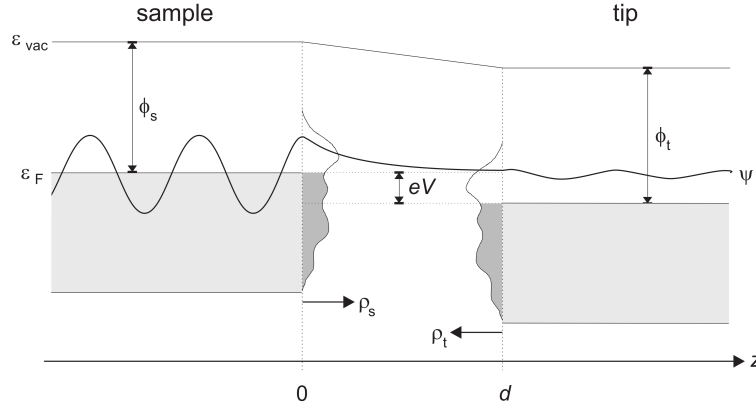


Figure 2.1. – Energy diagram to visualize the tunneling process between sample (left) and tip (right) separated by a distance d . Work functions of sample and tip (Φ_s and Φ_t) separate the filled states (shaded regions) and the vacuum level (ϵ_{vac}). Since sample (ρ_s) and tip DOS (ρ_t) may not be uniform, a fictional DOS is sketched in darker colors between both. The samples energy is lifted by eV after a bias is applied and results in a net electron current from the sample into the tip. One tunneling process is indicated by a wave function Ψ . After overcoming the vacuum barrier its amplitude decreased and the corresponding electron occupies a free state (white background) in the tip material. Adopted from [8]

2.1.2. Basic principles

In the following the tunneling process through a vacuum gap between metallic tip and sample will be summarized, addressed theoretically and used to describe the basic concept of STM.

Consider a system where two metals (sample and tip) are separated by a vacuum gap.

The amount of energy needed to remove an electron from the metals highest occupied energy level (E_F , Fermi energy) is called work function Φ . It depends on the electrostatic potential ϕ_E that has to be overcome by an electron with charge e at the surface.

$$\Phi = -e\phi_E - E_F$$

Figure 2.1 shows an energy diagram for tip and sample. The work function Φ_s (sample) and Φ_t (tip) separates the vacuum level ϵ_{vac} and Fermi energy E_F .

If sample and tip are in thermodynamic equilibrium, their Fermi energies are equal. When both are brought in close contact, electrons from the sample tunnel into unoccupied states of the tip and vice versa with the same probability. Hereby electrons close to E_F have the largest decay length and contribute strongest to the tunneling current. This current can be modeled and calculated in simple systems.

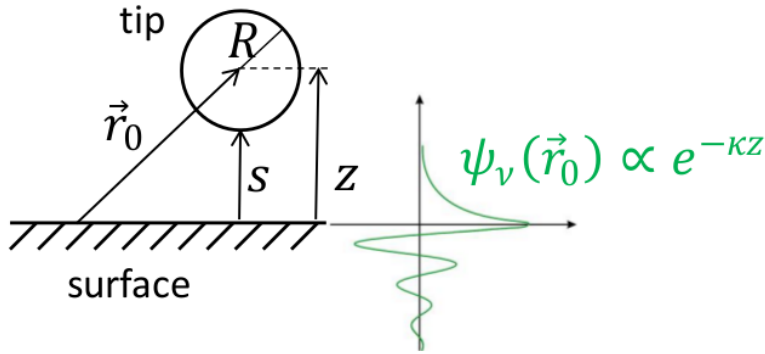


Figure 2.2. – Left: Tersoff-Hamann geometry model for a tip with radius R positioned at a distance s above the sample at position \vec{r}_0 . Right: Exponential decay of electronic states at the sample surface into the vacuum. Image adopted from [11].

In the model of Tersoff-Hamann the tip is atomically sharp and its electrons waveform is s-like.¹ Further assuming low temperature and a constant band structure for the tip with apex radius R , it is possible to calculate the tunneling current I

$$I \propto \frac{2\pi e^2}{\hbar} \cdot U \cdot \rho_t(E_F) \cdot e^{2\kappa R} \rho_s(E_F, \vec{r}_0)$$

where $\rho_s(E_F, \vec{r}_0)$ is the LDOS of the sample at E_F , evaluated at position \vec{r}_0 .

With this theory constant current STM images the surface density of states for a given voltage U .

$$\rho_s(E_F, \vec{r}_0) = \rho_s(E) \cdot \exp(-2\kappa \underbrace{(s + R)}_Z)$$

The exponential decay ($\propto e^{-\kappa Z}$) of an electron wave function into vacuum is characterized by $\kappa = \frac{\sqrt{2m\Phi}}{\hbar}$. It limits the current, which is proportional to the squared amplitude of it.

$$I \propto e^{-2\kappa Z}$$

Like in one dimension the current depends on the barrier height Φ through κ . Increasing the distance exponentially decreases the tunneling current. This exponential relation is the reason for the excellent topography resolution capabilities of STM. While its a good first approximation of the system, in many cases more than just the electrons near Fermi contribute. Also a uniform $\rho_t(E)$ may not be accurate in all cases.

¹Please's note that there are more models and corrections to them. An evolution from Bardeen's approach to the one done by Tersoff-Hamann can be found here [9, 10] including Chen's expansion.

2. Experimental methods

Using Wentzel-Kramers-Brillouin (WKB) theory[12–14] the tunneling current is given by

$$I = \int_0^{eU} \rho_s(r, E) \rho_t(r, eU + E) T(E, eU, r) dE \quad (2.1)$$

where T is the tunneling transmission probability

$$T(E, eV) = \exp \left(-\frac{s\sqrt{2m}}{\hbar} \sqrt{\frac{\Phi_s + \Phi_t}{2} + \frac{eU}{2} - E} \right) = \exp(-2\kappa_{eff}(E, U)s) \quad (2.2)$$

describing the probability of an electron tunneling event between tip and sample.

The samples potential can be changed by applying a voltage $V = U_b$ (bias) to it. This lifts its Fermi energy with respect to the tips and leads to a net electron current from the sample into the tip. Inverting the voltage results in electrons tunneling from the tip into the sample. If $eV < 0$ the tunneling current is largest for $E = 0$ (electrons on the Fermi-level of the sample), if $eV > 0$ the tunneling current is largest for $E = eV$ (electrons on Fermi level in tip).

Due to the fact that the tunneling current is proportional the density of states in the tip and the sample one can deduce its band structure within a range of several volts in the vicinity of the Fermi energy. Investigation of this behavior led to the establishment of a new measurement technique, called scanning tunneling spectroscopy (STS).

2.1.3. Scanning Tunneling Spectroscopy

Changes of the tunneling current with the bias voltage were observed by Tromp et al. in 1986 [15]. They discovered a change in contrast when scanning a Si(111) surface with either positive or negative bias. The change in contrast is most apparent in semiconductors and semi metals[16], but adsorbates and charged areas of the sample change the DOS locally and therefore the contrast in STM. While simple results may be already obtained by comparing two images recorded at different biases, more detailed information can be achieved.

If tunneling conditions are such that $eV \leq \Phi$, observed features in dI/dV are associated with the surface DOS. Critical points in the surface projected DOS give rise to features in dI/dV . Interpretation of these features with the WKB theory (i.e. differentiating equation (2.1)) gives

$$dI/dV = \rho_s(r, eV) \rho_t(r, 0) T(E, eV, r) + \int_0^{eV} \rho_s(eV) \rho_t(r, E - eV) \frac{dT(E, eV, r)}{dV} dE \quad (2.3)$$

The first term $\rho_s(r, eV) \rho_t(r, 0) T(E, eV, r)$ contains the DOS of tip/sample and the trans-

mission function. It describes the dependence on the DOS in the sample for energies eV - our desired spectrum. While T is usually unknown, a closer look to (2.2) indicates a smooth, monotonically increasing function in V . This mannered dependence on V gives a smooth background described by the second term $\int_0^{eV} \rho_s(eV) \rho_t(r, E - eV) \frac{dT(E, eV, r)}{dV} dE$. As for STM topography images, bias voltage can be chosen to either probe occupied ($U_b < 0$ V) or unoccupied states ($U_b > 0$ V). At low temperatures the vanishing lateral movement of adsorbates makes them also accessible to tunneling spectroscopy with sub molecular lateral resolution.

2.1.4. Machine description and experimental details

The success of STM and STS is promoted by good mechanical engineering. Since distances down to the atomic length scales are investigated, the experiment needs a careful set up. This is true especially for damping of external vibration that would otherwise conflict with the measurement. Sufficiently low partial pressures are needed to achieve small contaminant adsorption rates and the long investigation times associated with them. To conduct experiments in the most controlled environment possible, sample preparation and investigation is done in ultrahigh vacuum (UHV) chambers.

Since all used UHV chambers have many common parts, a typical setup is described with the low temperature (LT) STM setup, where most experiments were carried out.

The central part of the LT-STM setup is the commercial **Beetle-type STM scanner** [17] as shown in **Figure 2.3**. Here a helicoidal ramp carries the central scan piezo with attached STM tip. Three outer piezo tubes are used in slip-stick motion to circularly move on the ramp. Because the ramp is cut with an inclination of 2° the circular motion of the piezos results in the STM tip moving up and down. This is used to control the height above the sample during tip approach and macroscopic lateral movement.

Not only the macroscopic movement of the STM stage is controlled with a set of piezos, but the position of the tip (x, y, z) during scanning, too (see **Figure 2.5**). In this work a segmented tubular piezo is used to control the tips position. The piezos elongation can be controlled with the voltage applied to them, which is used to choose not only the tip-sample distance. Lateral movement is controlled by addressing its four segments. Each is used to control movement along $\pm x$ and $\pm y$ direction. For recording an topographic image the area is raster scanned in consecutive lines, applying a sawtooth voltage to the fast scan direction. The next lines are chosen by stepwise increasing the voltage along the slow scan direction. Other parameters like image size and scan speed are controlled with the piezos as well.

The measured current is translated into a voltage (I/U converter) and processed in a 20

2. Experimental methods

Bit analog → digital (A/D) converter. The current intensity is feed into the Digital signal processor (**DSP**) board. Here the STM Software's current set point is compared with the measured value. The tips position is controlled with a feedback loop. If the tips position needs to be corrected, a voltage is applied to the corresponding piezo element.

Differentiation of the current signal is done with an **Lock-In Amplifier**. Here the spectrum is not recorded directly by sweeping the bias and numerically differentiating the measured current. A sinusoidal modulation on top of the bias voltage is used. The modulated bias leads to a tunneling current modulation with the same frequency. The differentiation is performed by reading the AC current signal with the same frequency as the modulation which directly gives the dI/dV signal and therefore the DOS of the sample at U_b . Because the Lock-In Amplifier then only takes signals with the same frequency than the excitation frequency into account, the results are much less suspect to noise. Compared to numerical differentiation, a Lock-In needs less computing effort, too. It is important to note that the DSP does not recognize the bias/current modulation as topographic feature and regulates as without modulation. If the modulation frequency is too low, the feedback tries to compensate the modulation by changing the distance to the sample. If the modulation frequency is too high, the capacitance between tip and sample leads to an 90 deg phase shifted current which increases with modulation frequency. One usually chooses the modulation frequency slightly above the cutoff frequency for the feedback loop.

The UHV setup for the LT-STM is shown in [Figure 2.4\(a\)](#). With a base pressure of $\approx 5 \times 10^{-10}$ mbar these stainless steel chambers are almost free of contaminants. Since the rate at which residual gas contaminates the sample is proportional to the residual partial pressure, the time needed to cover the surface is proportional to it. When the base pressure is lowered by a factor of 1×10^{-13} (1 bar → 1×10^{-10} mbar), the time needed to cover the sample is increased by a factor 10^{13} .

To maintain UHV conditions, a set of pumps is used. For the preparation chamber, where high partial pressures occur during sample cleaning and preparation, a combination of roughening and turbo molecular pumps is used. First a roughening pump lowers the atmospheric pressure to 1 mbar. With this pressure on the outlet side a turbo molecular pump is used to decrease the pressure even further to the 1×10^{-8} mbar range. The remaining pressure is caused by adsorbate covered chamber walls where continuous ad-/desorption takes place and maintains a pressure equilibrium. After heating the entire chamber to temperatures above 120 °C while constantly pumping, most of the water is desorbed from the walls and pumped. After cooling down to room temperatures, the pressure settles in the 10^{-10} mbar regime.

As the pumping efficiency of turbo molecular pumps decreases for low pressures, each

chamber is equipped with an ion getter pump. Here a high voltage 1 kV to 7 kV is applied between two getter materials. Residual gas particles ionize in the strong electric field and are accelerated towards the plates. Here they impinge with high velocity and are buried deep in the plate material that they can't leave. The reduced number of residual gas particles results in a lower pressure.

To further reduce the number of potential contaminations, parts of the chamber can be cooled down with liquid nitrogen. Because of the great temperature gradient, gaseous residuals condense on the much cooler surface of the cooling trap and remain adsorbed while the temperature is kept low. Without refilling with liquid nitrogen the temperature slowly increases over time, so that the cooling trap loses pumping efficiency over time (usually after 1 h to 2 h) and starts to release trapped contaminants.

A titanium sublimation pump is installed to evaporate titanium on demand. This covers the chamber walls and, due to its reactivity, binds residual gas molecules. After some time the reactivity diminishes and a new layer has to be evaporated. With short operation intervals once a day the base pressure of the UHV system can be improved permanently.

While LT-STMs may be operated with solely helium as coolant, it is more resource saving to only cool the direct proximity of the sample and the STM with He (boiling point: 4.2 K) and to suppress the heat flow out of the He cryostat with a second, surrounding nitrogen cryostat (boiling point: 77 K) as shown in [Figure 2.4\(b\)](#)). This diminishes consumption of globally limited He. To maintain a temperature of 5 K to 7 K, one to two liters of liquid helium are evaporated a day, plus an additional amount of three to four liters liquid nitrogen. Evaporated helium is reclaimed in a closed circuit with a system of purifying and storage/cooling steps so that only a small amount of helium escapes the circuit and is lost.

Sample temperatures down to 5 K to 7 K allow for observations not possible at elevated temperature. Cooling not only reduces thermal drift in the piezo elements that are used to control the tip's position on the sample. Thermal energy at low temperature is not high enough for atoms or molecules to move on most substrates. Species mobile at room temperature (and therefore not representable at room temperature in the sub-ML regime)

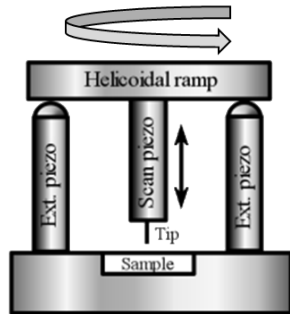


Figure 2.3. – STM sample stage to control the tip position. The coarse movement is controlled by exterior piezos. Each moves on a heliocoidal ramp with slip-stick motion. The precise positioning during scan is done with a central piezo to which the tip is attached. Modified from [18].

2. Experimental methods

become immobile and accessible for ST microscopy and spectroscopy. ST spectra resolution is better at low temperatures.

Two damping stages are used, one for the chamber and a sequential one for the STM.

First the whole UHV system is build within a frame that is placed on air pressurized cylinders. These can be lifted on demand, so that the chamber floats on four dampers and external vibrations/shocks are damped. Three legs are adjustable in height to level the whole setup properly.

A second stage decouples the sensitive STM scanner from the rest of the setup. First the complete STM stage hangs on springs to further limit the direct influence of vibrations. Second the remaining oscillation amplitude is damped by a eddy current damping. It is made of three magnets in close proximity to a surrounding conductor so that eddy currents are induced for each movement. The eddy current is typically larger at cryogenic temperatures, that results in a damping that works best at low temperatures. The kinetic energy of the oscillating system is transferred by the eddy currents into heat within the surrounding support. The heat is then mitigated by the external cooling of the cryostat.

Experimental details **Topography images** are created by raster scanning the surface pixel by pixel. We use the constant current (cc-STM) operating mode where the tips height is controlled to achieve a constant tunneling current as shown in [Figure 2.5](#). The regulating voltage on the height control piezo is recorded and plotted in a color-scale for each pixel. The brighter the color, the more the piezo had to retract the tip to maintain the constant tunneling current setpoint. Regions with the same DOS thus appear in the same contrast.

Differential conductance measurements are performed in two ways - on single points (spectrum) and on areas (map). The feedback loop that controls the tip vertical position is not in use, so that the tip maintains a constant height that is set before measurement.

Single point spectra are used to measure electronic properties like molecular orbital energies and electronic band gaps. Spectroscopic information is obtained by sweeping the bias voltage while recording the tunneling current ($I(V,z)$ -spectroscopy) at constant tip-sample distance. Differentiation results in a term proportional to the DOS (see [Equation 2.3](#)).

Spectral maps at a fixed bias show real space distribution of electronic states at the DOS that corresponds to the chosen bias. The signal intensity represents the differential conductance \propto DOS. Differentiation is done with a Lock-In.

For both types it is important to eliminate lateral and vertical drift, to ensure a fixed tip position above the point of interest during the measurement. This is even more important for spectral maps, since they take a long time to record.

Lateral manipulation of atoms and molecules is possible with the STM tip. With a matching current/voltage set point, the tips vertical position can be chosen such that the tip interacts with the adsorbate. Lateral displacement of single molecules within molecular assemblies is only possible if molecule-molecule interactions are weak, e.g. no covalent bonds are formed between molecules. If molecule-molecule interactions dominate, clusters of molecules are moved.

Experiments based on STM were done at different experimental chambers: (1) The described LT-STM chamber [21–23] and (2) a RT-STM with XPS capabilities described elsewhere.[22].

The tip termination was changed in different ways. 1. **Voltage pulse:** A voltage pulse ($U_b \leq 10$ V) is given for a short time ($t \leq 1$ s) when the tip is in tunneling contact. The intense current pulse reorders the tip termination often leaving some tip adsorbates on the sample surface. While small pulses often only slightly change the tip geometry, larger pulses may lead to heavy rearrangements in tip and sample. 2. **Vertical over-approach:** The tip is pushed into the sample surface in order to remove tip adsorbates and aggregate sample surface atoms at the tip. While this works best for metallic samples, it should be avoided to accidentally cover the tip with insulating adsorbate layers as present for *h*-BN preparations. 3. **Field emission:** An external power supply is used to apply a voltage ($U_b = 100$ V to 500 V) between tip and sample. A serial resistor limits the current through the connected internal wires. Tip and sample are brought in close proximity to enable the tunneling process. Because of high electrical field strengths at the tip apex strong forces occur. Depending on the polarity the tip can either expel tip atoms or aggregate sample surface atoms. With a careful distance increase a new tip apex can be build up. The above mentioned ways are done with the tip remaining inside the STM. 4. **Tip sputtering:** To reorder the tip structure and to remove adsorbates accelerated Ar^+ ions are used. Because of higher partial pressures needed for sputtering the sample is transferred from the LT-STM into the preparation chamber. Here the tip is bombarded with Ar^+ ions ([PARAMETERS](#)), annealed ([PARAMETERS](#)) and transferred back into the STM.

2.1.5. Limitations

The accuracy of a STM is very high with spatial resolution down to the atomic scale.

Lateral resolution with the STM depends on the tip shape and termination. A tip with single atom termination records sharp topography images. When there is more than one atom in the tip apex participating in the tunneling process, lateral resolution decreases and an image for each tip termination is created. This is often recognized by blurry step edges and artifacts that repeat several times within a single image.

2. Experimental methods

Spectral resolution is influenced most by the tip DOS. Before each measurement a reference spectrum is recorded on the metal surface to ensure the the DOS of the tip is metallic and does not show unexpected additional states that are typically induced by a modified tip.

Due to the fact that the tips motion is controlled with different piezos, one has to take different elongations in different directions into account. For example, if the STM scans the fast scanning direction just a bit further than the slow scan direction, the resulting image (although pixel wise square) is no longer physically square anymore. For moderate shear below 5 % however, conformity is almost conserved and the angular uncertainty below 1.5°.

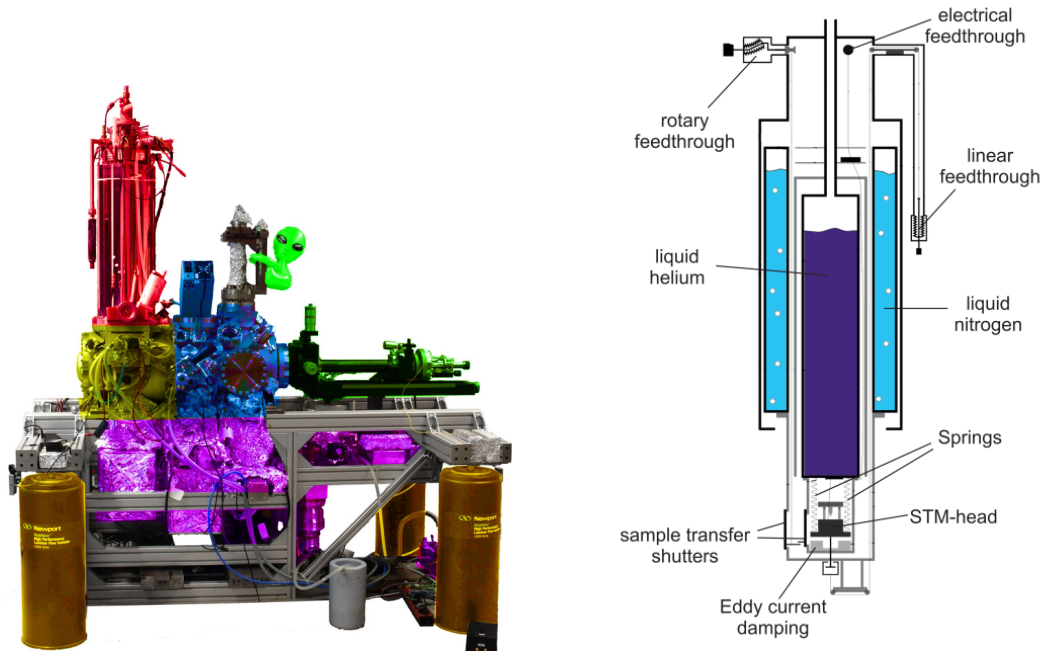
Because STM is sensible to electronic changes, it may change the footprint of an adsorbed compound [24]. Laterally approaching an adsorbate results in an additional tunneling current, because now electrons do not only tunnel directly into the substrate but through the adsorbate as well. Interferences between both tunneling processes depend on the adsorbate's orbital-symmetry and tip-shape. Local density of states calculations [25–27] are not adapted to grasp this effect since the tip is considered far away from the surface. Moreover, the tip radius or the tip-substrate distance is often optimized to fit the lateral size of the adsorbate print with the experimental image [25, 27].

Mechanical and thermal vibrations limit the resolution of STM and STS, too. Therefor the damping stages that decouple the STM from the surrounding are important but may not always filter all mechanical vibrations.

Signal wires (coax) are well shielded against electromagnetic radiation. Since the signal is transmitted with cables an external radio signal may otherwise couple into the wire and tamper with the signal.

Although STM works at room temperature, additional cooling may be applied to reduce the thermal vibrations.

STM is not capable to discern different elements. As complimentary method, X-Ray photoelectron spectroscopy is used for convenient chemical identification of adsorbates.



(a) LT-STM setup. Different functional groups are highlighted by colors. A low base pressure is achieved with a combined pumping system comprised of ion pumps and turbo molecular pumps (cyan). Sample holders are operated with a rotatable, variable temperature manipulator (green). Sample preparation is done in the preparation chamber (blue). After transfer to the LT-STM chamber (yellow) a gate valve is used to seal the LT-STM from remaining residual gas that may be present in the preparation chamber. The liquid helium/nitrogen bath cryostat (red) is used to maintain low temperatures (see (b)). Vibration isolation of the frame is achieved with legs floating on pressurized cylinders (orange).

(b) Scheme of a liquid bath cryostat. While in the inner stage a temperature of 5 K to 7 K is achieved with a liquid helium reservoir, an outer liquid nitrogen cryostat is used to isolate the inner cryostat from the surrounding room temperature and to reduce the amount of liquid helium used to maintain cryogenic temperatures.

Figure 2.4. – Typical setup for low temperature measurements. A vibration isolated UHV chamber is used to prepare samples and investigate them in a separable chamber with either STM or AFM. A liquid bath cryostat is used to maintain low temperatures. Images adopted from [19]

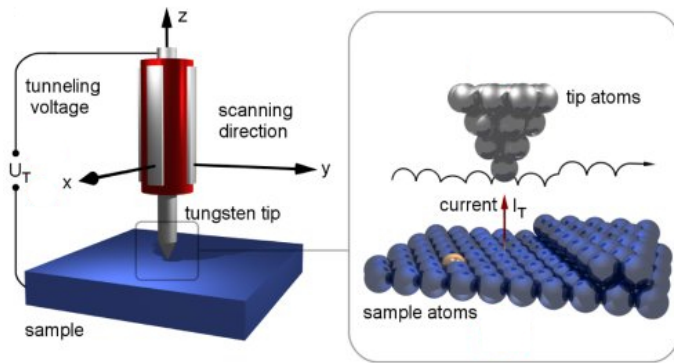


Figure 2.5. – Operating principles of a STM. A macroscopic sketch shows the central piezo that controls the tip position on the sample. The piezo is divided in four parts to control movement in the x - y plane and tip-sample distance. A microscopic sketch shows the tips movement in constant current mode while moving across a atomic step edge. Here the tip is retracted to maintain a constant current, which in turn leads to a larger apparent height in STM. Note the single incorporated alien atom. Although its height is the same as its neighbors, STM records the change in DOS. Less electrons tunnel and the apparent height on the terrace is reduced above the alien atom. Adopted from [20]

2.2. X-ray Photoelectron Spectroscopy

X-Ray photoelectron spectroscopy (XPS) is a tool to achieve information of the samples chemical structure. When X-rays with sufficient energy hit metals, electrons are emitted. This effect is called photoelectric effect and was first discovered by Heinrich Hertz in 1887 through the fact that electrodes illuminated with ultraviolet light create electric sparks more easily.[28] 18 years later Albert Einstein received the Nobel Price for his discovery of the law of the photoelectric effect[29] and a scientific explanation which Hertz was missing. For a fixed X-ray energy the emitted electron's kinetic energy depends on the element the electron was emitted from and allows for exact identification of the atomic species on the sample. XPS is used in a wide field of investigations[30] and awarded Kai M. Siegstein with a nobel prize in 1981[31].

2.2.1. Theory

As the X-rays hit and penetrate the sample surface they excite electrons at the surface and on the lower lying atomic energy level along their path.

For the **core-level excitation** the X-ray removes a single electron strongly bound to the core. Energy conservation due to elastic scattering of the electron out of the bulk results in the relation

$$E_B = h\nu_{\text{X-ray}} - E_{\text{kin}} - \Phi_{\text{analyzer}} \quad (2.4)$$

$h\nu_{\text{X-ray}}$ is the energy of the incident X-ray beam, E_B the binding energy of the excited electron and Φ_{analyzer} the work function of the analyzer. The larger the electrons binding energy, the less energy is left for kinetic energy which is recorded by the analyzer.

The **chemical surrounding** of atoms changes their binding energy, making XPS an ideal tool to investigate chemical bonds and stoichiometry. Although the analysis is averaged over the area of the incident X-rays its results are very precise. This makes it possible to distinguish differently bound atoms within single atomic species and therefore gives rise to otherwise not directly observable processes like growth, intercalation, etching and binding of for example graphene islands on Ir(111)[33, 34]. The binding energies of some atomic transitions are given in Table 2.1.

The shape of the peaks typically resembles the line shape of the used X-rays (Gauss width $\approx 1\text{eV}$). In case of s-states ($l = 0$) ($\text{B}\,1s$, $\text{N}\,1s$, $\text{C}\,1s$) the peaks are singlets. With increasing $j = l + s$, the spin-orbit (j - j) coupling introduces a 'parallel' and 'anti-parallel' nature of the spin, resulting in two different $j = \frac{1}{2}(\frac{3}{2})$ and therefore two different energies. The ratio of the two peak areas is given by their degeneracy $(2j + 1)$ [36, p. 113], so that

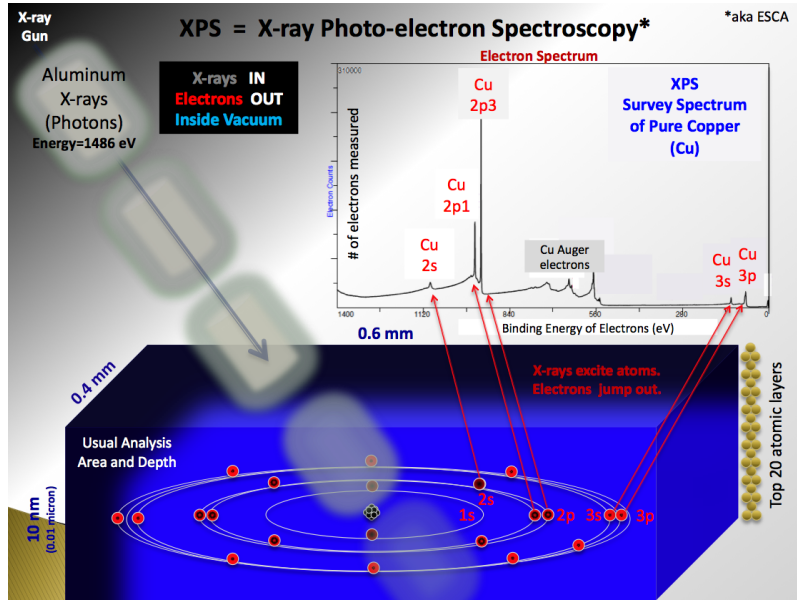


Figure 2.6. – Representation of a XPS process. A scheme of a X-ray gun illuminating a sample area of about $0.4 \text{ mm} \times 0.6 \text{ mm}$ is shown. X-rays are used to excite core level electrons. Excited electrons within the first 20 layer escape the sample. After leaving the sample these show element specific signatures in their kinetic energies. A detailed analysis of the peak shift allows for identification of the chemical environment. See [32]

Table 2.1. – Element specific transitions and binding energies for some chosen elements as reported in [35]

Element	Ground state	E_B [eV]
O	$1s$	531
N	$1s$	398.1
C	$1s$	285
B	$1s$	189.4
Cu	$3s$	123
Cu	$3p \frac{1}{2}(\frac{3}{2})$	77 (75)

the Cu $3p_{\frac{3}{2}}$ peak is two times larger than Cu $3p_{\frac{1}{2}}$.

2.2.2. Experimental details

The **X-ray sources** used are supplied with aluminum and magnesium anodes. With these, electrons are accelerated with typically 15 keV onto the anode of choice. Most of the created radiation is made up of the principal characteristic line ($K\alpha_{1,2}$). Higher ones ($K\alpha_{3,4}$, $K\beta$) are also observed but with much lower intensities. In addition there is a continuous background called Bremsstrahlung extending up to the energy of the incident electron energy. This background is of no use for the XPS measurement and has to be subtracted in a more or less artificial way. For XPS measurements the Mg $K\alpha = 1253.6$ eV and Al $K\alpha = 1486.6$ eV are used situationally to shift the core level spectra with respect to Auger transitions at occur at constant kinetic energy.

The more atoms of a specific kind are present, the larger the signal gets. Therefore the signal intensity resembles the amount of atoms on the topmost surface layers(≈ 10 nm). As each irradiated atomic species has a different **cross section** for adsorption of X-rays with a certain energy they emit spectra with a different intensity. Comparing the cross section of e.g. N and B, one can see that it is roughly 4 times as large (B: 6.87×10^3 b/atom, N: 25.82×10^3 b/atom) for Al $K\alpha$ [37]. Meaning that the signal from the N is much stronger than that of the B, although their number of atoms is equal.

Gracing and normal emission are two operational modes in XPS. The maximum information depth in XPS measurements is mainly limited by the escape length of excited core level electrons (≈ 10 nm). The mean free path of electrons with energy E in a solid is approximated by $\lambda = \frac{143}{E^2} + 0.054\sqrt{E} \stackrel{E=1\text{ keV}}{\approx} 1.7$ nm.[38] This is much smaller than the penetration depth of X-Rays which is in the order of 10 nm. An increasing angle between sample normal and detector entrance increases the path the electrons have to travel through the bulk to reach the analyzer. Because the mean free path of the electrons stays the same, a longer route in the bulk attenuates the signal of lower lying substrate atoms. Electrons leaving the surface adsorbate are not attenuated and gain in signal strength relative to the bulk atoms. Some supporting measurements are done in gracing emission to increase an otherwise small signal of an surface adsorbate but are not shown in this work.

The spectra used in this work are recorded without monochromator. Experiments are done at two different XPS setups. (1) The RT-STM/XPS and (2) the NIM-XPS chamber.

2.2.3. Limitations

Beam damage Since the X-Rays carry considerable energy other effects than the excitation of core electrons are possible. Especially for long analyzer integration times (for

elements with small cross section or little surface coverage) the amount of deposited energy results in unwanted side reactions on the surface. It is possible to trigger a change in the chemical surrounding of the investigated element, causing chemical shifts that are not present in the pristine sample and change the XPS spectrum over time.

Space averaging technique XPS is a space averaging technique. First the X-Ray beam has an inherent width, the analysis area can't be chosen arbitrarily small. Second, X-Rays do excite electrons not only directly within the illuminated area, but penetrate the bulk and cause a cascade of transitions in the sample. The resulting information is always a mix between surface adsorbates and bulk elements.

2.3. Atomic Force Microscopy

Atomic force microscopy (AFM) is like STM another scanning probe tool. To scan the surface of the sample, one uses a small oscillating tip to interact with it on short distance where forces between sample and tip occur. If the tip interacts with the sample, its oscillation is hindered/amplified and the frequency of the oscillation shifts. From this shift one can estimate the strength of the acting force. Since every type of adsorbate atom acts in different ways with the tip, AFM is element specific. When the tunneling current through the AFM tip is recorded, simultaneous AFM and STM measurements are possible.

2.3.1. Theory

Amongst others, forces between AFM tip and sample are made up of attractive forces like van der Waals (vdW) forces and repulsive forces like mechanical contact force and Pauli repulsion.

vdW interaction is always attractive and described by

$$F_{vdW} = -\frac{A_H R}{6z^2} \quad (2.5)$$

Here A_H is the ?, R ? and z ?. Although the strength quickly diminishes with distance z , vdW interaction is long range and thus always present in AFM measurements.

Mechanical contact force, Pauli repulsion and chemical bonding are given in the Lennard Jones (LJ) model.[39]

$$F_{LJ} = -\frac{12E_{min}}{z_0} \left(\left(\frac{z_0}{z}\right)^{13} - \left(\frac{z_0}{z}\right)^7 \right) \quad (2.6)$$

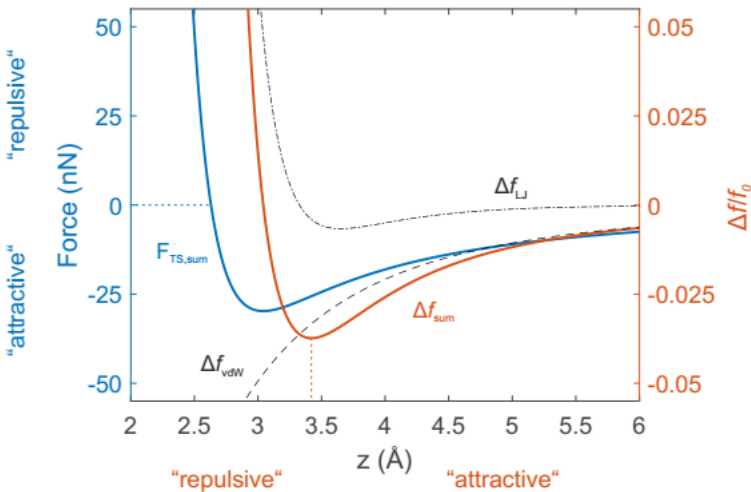


Figure 2.7. – Sketch of tip-sample interaction force (blue) together with relative frequency shift. Contributions of vdW and Lennard Jones like forces result in two separable frequency shifts Δf_{LJ} and Δf_{vdW} (black) that add up to a total of Δf_{sum} (orange) from where the total force is derived. From [22]

E_{min} is ?.

The typical resulting force between tip and sample $F_{TS,sum}$ is artistically shown in Figure 2.7. The sum of interaction $F_{TS,sum}$ between tip and sample is shown as blue line. The attractive vdW force is plotted in dashed black curve. A typical frequency shift Δf_{sum} is given as orange graph. The frequency shift Δf is proportional to the force gradient acting on the tip.

$$\Delta f = -\frac{f_0}{2k_0} \frac{\delta F_{TS}}{\delta z}$$

One can distinguish different regimes as indicated by the labels. When tip and sample are in considerable distance to each other, the attractive vdW forces are the dominant part in the sum. While the tip approaches the sample, more and more interactions with the surface and adsorbate add to this force, increasing F_{TS} . When the separation reaches z_0 , the distance becomes so small that repulsive forces overcome the attractive one at the border to the repulsive regime.

AFM measures does not measure a mix of electronic and geometric information projected onto a 2D-map like in STM.

To increase the lateral resolution the tip can be functionalized with CO. This method is widely used [40–46] to investigate not only geometric features that are not directly accessible in STM, but also chemical differences on the sample.[47]

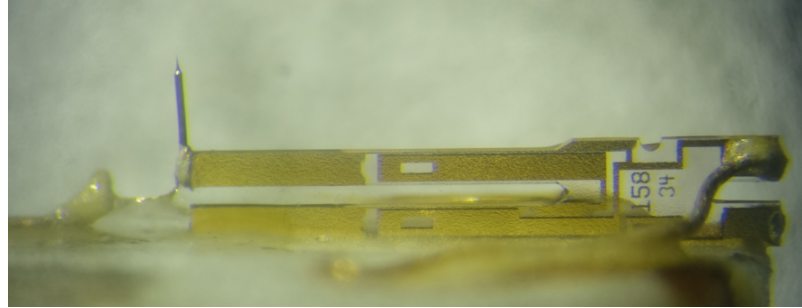


Figure 2.8. – Photograph of the tuning fork and cantilever. The tip is glued to the tuning fork on the left side. From [48]

2.3.2. Experimental details

The used LT-AFM features a tuning fork sensor, as shown in Figure 2.8. Here the tip is positioned below an oscillating fork. A piezo element that continuously stimulates oscillations in a quartz crystal is used to drive the forced oscillation of the tuning fork (f_0, k_0). To its end the AFM/STM tip is attached and follows the oscillation with a fixed amplitude.

Measurements are done in the frequency modulated mode, meaning that the shift in resonance frequency, by an amount Δf proportional to the force gradient, is recorded in constant height to show the proportional local force gradient. The image is created by raster scanning the surface like in LT-STM. The best images were recorded where repulsive contributions to $F_{TS,sum}$ arise. This is because repulsive forces are short range while attractive vdW interaction is long range and thus does not provide atomic contrast.

AFM experiments are done under ambient conditions (see copper foil characterization subsection 4.1.1) and in UHV at 5 K at the LT-AFM (see functionalized coronene chapter 6).

3. Substrates, ad layers and sample preparation

Experiments are mainly done with single crystalline substrates of copper and silver, terminated by (111) and (100) surfaces. Polycrystalline copper foils and gold evaporated on mica are used as well. Experiments are done to investigate molecules on *h*-BN/Cu(111) and *h*-BN/Cu(foil).

3.1. Substrates and adlayers

The following section will describe the relevant physical properties of the various substrates. First single crystal (subsection 3.1.1) and polycrystalline copper foil substrates (subsection 3.1.2) are discussed briefly. Geometric properties of lattice mismatched system are discussed briefly (see section 3.1.3). Later molecular adlayers on *h*-BN are exemplified by 2H-Porphine and NCPh₄CN on *h*-BN (subsection 3.1.4). A method to prepare polycrystalline copper foils to grow *h*-BN on is discussed in subsection 3.2.1. Preparation details for cleaning metal substrate samples (subsection 3.2.2), CVD growth recipe for *h*-BN dosage (subsection 3.2.3) and molecular beam epitaxy (subsection 3.2.4) will be summarized at the end of this chapter.

3.1.1. Single crystal substrates

Single crystals show a nicely ordered, clean surface - two properties important for accurate and reproducible experiments. We have chosen silver and copper as bulk crystalline substrates. Both metals form fcc lattices and their surface termination can be fixed by precise cutting along a symmetry plane of choice. For the course of this thesis, experiments are conducted mainly on (111) and (100) terminated surfaces as depicted in Figure 3.1.

The lattice constants a at room temperatures for Cu(3.61 Å), Ag(4.09 Å) and Au(4.07 Å) [49] are related to the nearest neighbor (NN) distances by multiplication with $\frac{\sqrt{2}a}{2}$. This makes the NN distances $NN : Cu_{111}(2.55 \text{ \AA}), Ag_{111}(2.89 \text{ \AA})$ and $Au_{111}(2.88 \text{ \AA})$. 2nd NN distance is a . When the surface facet is (100), nearest neighbor distances remain the same, only the 2nd NN distance is increased by multiplication with $\sqrt{2}a \cos(30)$ (see Table 3.1).

Lattice constants are related to environment temperatures by their expansion coefficients. Linear expansion coefficients of $16.5 \times 10^{-6} \text{ K}^{-1}$ (Cu), $18.9 \times 10^{-6} \text{ K}^{-1}$ (Ag) and

Table 3.1. – Inter atomic distances for Cu and Ag with respect to different surface termination. a denotes the lattice constant and $\beta = 60 \text{ deg}$ the angle within the (111) unit cell

	Lattice constant a [\AA]	Nearest neighbors [\AA]	diagonal [\AA]
	fcc(100)	$\frac{\sqrt{2}a}{2}$	a
Cu	3.61	2.55 2.55	3.61
Ag	4.09	2.89 2.89	4.09
	fcc(111)	$\frac{\sqrt{2}a}{2} < 110 >$	$\sqrt{2}a \sin(\frac{\beta}{2}) \sqrt{2}a \cos(\frac{\beta}{2})$
Cu	3.61	2.55 2.55	2.55 4.42
Ag	4.09	2.89 2.89	2.89 5.01

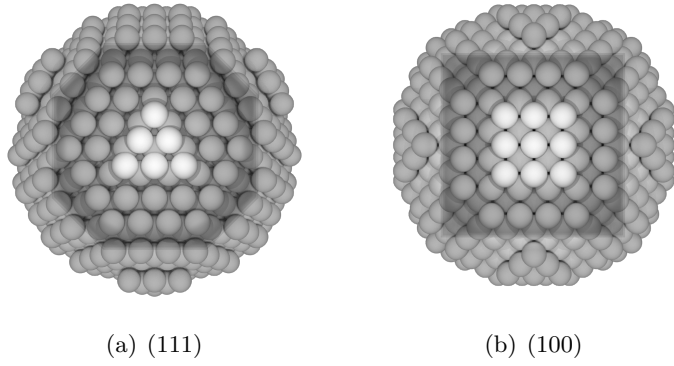


Figure 3.1. – Identical crystalline balls with fcc lattice and thus $[\text{ABC}]_n$ stacking configuration of crystal planes. The surface termination is determined by the direction of the intersecting plane (parallel to the paper plane) relative to the lattice and forms (111) and (100) surfaces.

$14.2 \times 10^{-6} \text{ K}^{-1}$ (Au) make the substrate lattice shrink by $\approx 0.5\%$ when it is cooled down from RT to low temperature measurement conditions (5 K to 7 K) in STM/AFM. This is negligible for bulk materials that are not heated and cooled over large temperature ranges. When an adlayer is adsorbed, different thermal expansion coefficients cause strain in the adlayer when the temperature changes. The effect is amplified when metal substrate and adlayer (*h*-BN) have thermal expansion coefficients with opposite sign (**Give expansion coefficient and lattice constant for h-BN**).[50]

The surface free energy increases from the (111) surface with increasing angle of the (hkl) planes of interest with

$$\cos(\phi) = \frac{h + k + l}{\sqrt{3(h^2 + k^2 + l^2)}}$$

[51]. Thus, the (111) surface is the one with lowest energy, followed by (110) and (100).

3.1.2. Polycrystalline copper foils

As was mentioned before, clean, highly ordered surfaces are desirable to perform experiments on. In case a systems order and functionality does not heavily depend on the substrates crystalline properties, single crystals loose most of their unique selling point. Instead of choosing a expensive bulk single crystal, thin polycrystalline copper foils are an alternative. The mass produced foils, although chemically pure, were never meant to be atomically flat and show considerable height variation.

Copper foils are manufactured by ...

A representation of a mechanically polished copper surface can be seen in **Figure 3.2**. Here the layered structure is apparent and shows different sizes of grains. Small sub grains constitute the uppermost layers, while deeper lying layers consist of larger grains with grain boundaries becoming more and more diffuse with increasing distance to the surface. For polycrystalline foils it is expected to observe the lowest energy facet (111) more often than the less favorable (110) and (100) facet. More properties like work function, surface state and chemical reactivity depend on facet orientation.

Large grains are preferred for growing 2D materials on copper foils because grain boundaries are subject to inhomogeneities within the 2D layer and provide a route for unwanted surface chemistry (copper oxidation for example).

To overcome the limitation of small grain size and heavily corrugated surface, etching of the copper foil is performed as described in subsection 3.2.1.

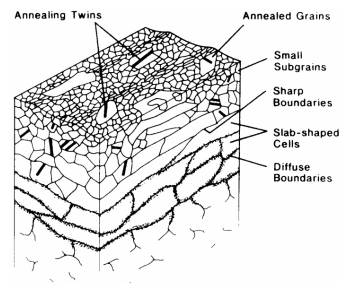


Figure 3.2. – Sketched bulk structure of a OFHC copper foil after abrasion with P1200 silicon carbide paper. Adopted from [52]

3.1.3. *h*-BN

In the last years, a new family of 2D materials arose. Its most known member, graphene, already attracted much attention in the research community. Graphene, a sp^2 -bonded carbon honeycomb lattice, has shown remarkable electronic and mechanic features determined by the atomic type and bond configuration. With careful preparation methods, large layers of defect free graphene are grown on a variety of substrates. Within this layer, a linear band dispersion is formed at the corners of the Brillouin zone (Dirac cones), that promote high charge carrier mobilities (cite).

Hexagonal boron nitride (*h*-BN) is isostructural and -electronical to graphene, but every second lattice site is occupied by nitrogen, every other by boron. The nitrogens larger electrochemical negativity - withdrawing electrons from the boron side - results in an ionic bond character between B & N. Compared to the covalent bond formation in graphene that facilitates its conductivity, the ionic bond character makes *h*-BN a wide band gap (≈ 6 eV) insulator. [53–55]

Free standing *h*-BN is investigated with *ab-initio* calculations [56–59]. Together with experiments [60] a RT crystal lattice constant of $a_{h-BN,RT} = 2.504 \text{ \AA}$ is derived. It can be grown on a variety of metal surfaces.[46, 50, 61–86]

Depending on the substrates used, different lattice mismatches can be achieved. Many geometric corrugations can be achieved with increasing lattice mismatch and substrate-*h*-BN interaction. Since this interaction is believed to have its origin in the partially filled d-states of the substrate,**citation** transition metal substrates are widely used. While substrates exist where the lattice constant are virtually identical (Ni: $\Delta \leq 0.5\%$), other substrates show large mismatches (Ag(111): $\Delta \approx 14\%$).

The growth of *h*-BN on nearly lattice matched Ni(111) resulted in uniform commensurate layers. With increasing lattice mismatch, moiré patterns are formed on Pd and Pt. The stronger interaction of *h*-BN and Rh(111) results in a corrugated nanomesh to be formed on the substrate.**citation** Even 1D structures are reported on Fe(110) [67] and Cr(110) [62].

Here we consider *h*-BN on Cu(111) ($\Delta \approx 2\%$) as example system of self-limited growth and highlight most relevant insights reported in literature.[46, 65, 87]

***h*-BN on Cu(111)**

Stoichiometry XPS measurements (see Figure 3.3) show B1s and N1s components in a 1:1 ratio, indicating that the layer retains the precursor stoichiometry during growth, but all hydrogens are cleaved from the precursor prior to layer formation and desorp from the sample.[88]

Moiré geometry The properties of various moiré superstructures are well described in literature and Hermann gives a comprehensive overview in his paper.[89] A moiré is always present if an over layer shows a lattice mismatch with respect to the substrate. Here the two most important examples are given, i.e. for an overlayer with the substrate Bravais lattice (hexagonal) either aligned with the substrate basis or rotated by an angle α .

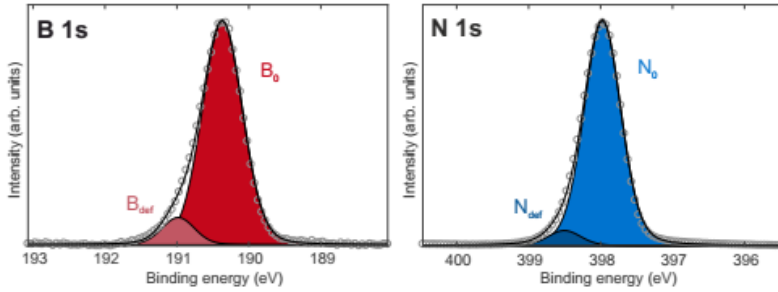


Figure 3.3. – XPS of a full ML h-BN on Cu(111) grown with CVD of borazine. Fit components B_0 ($E_b = 190.4$ eV), N_0 ($E_b = 398.0$ eV) and B_{def} ($E_b = 191.0$ eV) and N_{def} ($E_b = 398.5$ eV) are assigned to pristine h-BN layer and defective components respectively. Adopted from [22]

For **isotropically scaled and aligned over layers** one can calculate the scaling factor

$$p = \frac{R'_{O1}}{R_{O1}}$$

which gives the size of the over layer lattice R'_{O1} in units of the substrate lattice R_{O1} . The moiré pattern shows the same bravais lattice type than the substrate[89, p. 10]. If moiré and ad layer lattice are aligned ($\alpha = 0^\circ$) the direction of moiré and substrate is aligned. The period of the moiré calculates to

$$a_{\text{moiré}} = \underbrace{\frac{p}{|p - 1|}}_{\kappa} a_{\text{substrate}}$$

With $a_{\text{moiré}}$ and $a_{\text{substrate}}$ are experimentally available, the ad layer lattice can be calculated with high precision (usually one order of magnitude more accurate than direct measurement of its period).[50]

Depending on the relative orientation of h-BN and substrate the moiré period changes. Although large domains with uniform orientation can be grown on single crystal substrates (Figure 3.4(a,c)), rotational domains exist(Figure 3.4(b,d,e)). The model representation nicely shows the change in moiré period when Figure 3.4(c) shows a case where the h-BN ad layer has the same unit cell orientation than the copper. For a **isotropically scaled and rotated over layer** the angle between substrate and moiré (γ [rad]) scales with the angle between over layer and substrate (α [rad]) as $\alpha = (1 - p)\gamma$. In this case, one can determine α and p from experimental observables γ (moiré angle to substrate) and κ (scaling

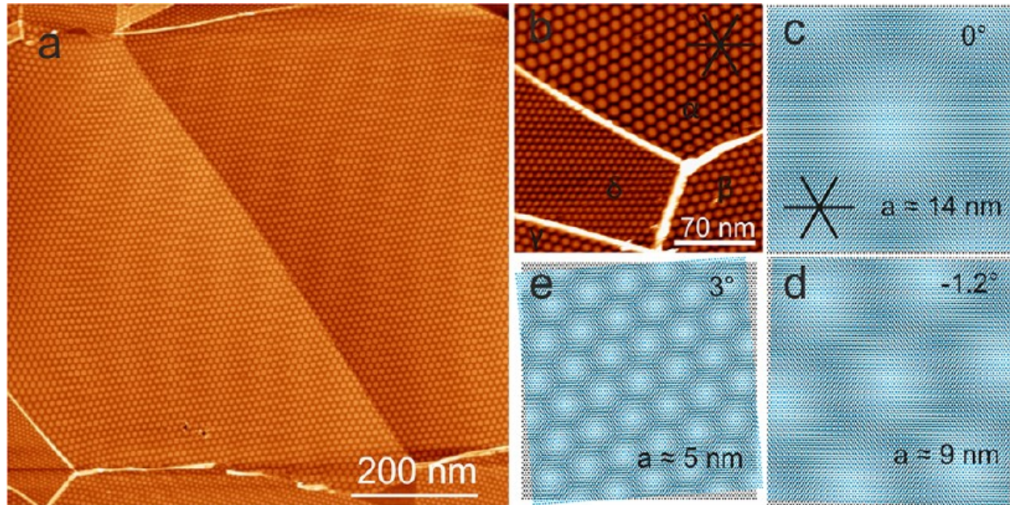


Figure 3.4. – (a) STM topography of h-BN on Cu(111). Large domains with uniform orientation and moiré period are formed after CVD growth. (b) Different rotational domains are observed that show different moiré periods, reproduced by three models (c-e) where different h-BN rotations are shown together with the resulting moiré periods a . Adopted from [65]

factor) through relations

$$\alpha = \arctan \left(\frac{\sin(\gamma)}{\cos(\gamma) + \kappa} \right) \quad p = \frac{\kappa}{\sqrt{1 + \kappa^2 + 2\kappa \cos(\gamma)}}$$

As mentioned above the orientation of the moiré superstructure is determined by the relative ad layer rotation alone, while its period is determined by lattice mismatch, too. This results in a variety of moiré superstructure orientations and periods, strongly related to the used substrate.

Periodic change in work function A direct result of the lattice mismatch between h-BN and Cu(111) is the changing registry of ad layer atoms and substrate. The periodic modulation of B/N registry to the substrate atoms results in regions of stronger and weaker interaction between h-BN and substrate and is the reason for the nano templating effect of h-BN on many substrates. **citation** In the following some effects are discussed that lay the foundation for a nano patterning effect of h-BN and its influence on the electronic structure of adsorbates.

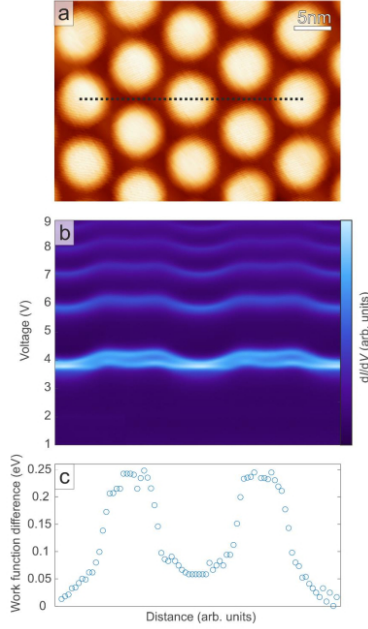
While a first report in 2004 [84], pointed to the formation of a complicated two layer structure, later experiments [90, 91] including ours [46, 65] proved a single layer of B & N atoms in a regular hexagonal lattice when grown on Cu(111). It evolved as well investigated

system to perform experiments on. After CVD growth it adsorbs on Cu(111) as a flat layer. Due to its lattice mismatch, "hill" regions (corresponding to a $N_{top}B_{fcc}$ registry) and "valley" regions (corresponding to a $N_{fcc}B_{hcp}$ registry) are formed. In these regions the work function is altered in opposite directions. While larger at the hill/pore regions, the work function reduces continuously to its lowest value in the valley/wire regions.¹

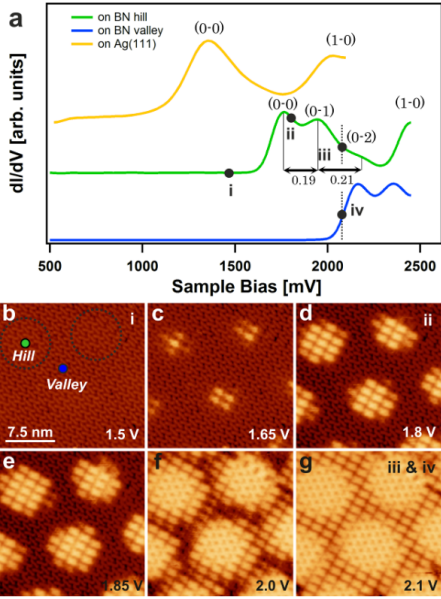
After growth of *h*-BN the substrates total work function is reduced [e.g. Rh: 5.1 eV to 3.07 eV [70]. Therefor a dipole moment μ pointing from the bulk to the surface is necessary, rather likely created by a negative charge transfer from the bulk into the ad layer.[92]

Everywhere two regions with different work functions meet, local electrostatic fields arise to compensate for the vacuum level misalignment.

¹Please note that the notation is not uniform throughout the literature. Sometimes hills are referred to as pores and valley regions are denoted as wire regions.



(a) Work function variation along *h*-BN/Cu(111) moiré. (a) STM image showing the *h*-BN moiré with a periodicity of 8.4 nm. Scan parameter: $U_b = 4.0$ V, $I_t = 40$ pA. (b) Field emission resonances acquired along the black dotted line in a) revealing a variation of the peak positions. (c) Work function differences between bright (“hill”/pore) and dark (“valley”/wire) regions obtained from the dI/dV curves of the field emission resonances displayed in b). Adopted from [46]



(b) Position dependent energy level alignment of $NC - Ph_4 - CN$ on *h*-BN/Cu(111). Three spectra are compared, recorded on molecules at valley (blue) and hill positions (green). A spectrum of the bare Ag(111) is shown as reference (yellow). STM images at different bias voltages are shown (b-g). While at low bias (b) all molecules appear in the same contrast, molecules residing at the hill positions contribute at lower bias (b-d) to the tunneling current than molecules in the valley regions where molecular orbital energies are shifted to higher energies. Increasing the bias (e-g) incorporates molecules at valley positions into the the tunneling process. Taken from [93]

Figure 3.5. – Workfunction change for pristine *h*-BN/Cu(111) ((a)) and for adsorbed molecules on *h*-BN/Cu(111) ((b)). For pristine *h*-BN/Cu(111) the position depended change in workfunction is shown by a variation in the field emission resonances. (b) After adsorption of molecules a shift in molecular orbital energy is emphasized by single point spectra taken at different positions within the moiré unit cell. This spatial variation can be visualized by STM images taken at the right bias voltages.

3.1.4. Molecular assembly on *h*-BN

With changing work function, a lateral electric field emerges. For gr/Ru(0001) lateral dipole pointing from valley to pore sites arise.[94] It can be used to trap adsorbates with dipole moment along the field lines. This was shown for FePc and pentacene molecules on a graphene/Ru(0001) substrate. Here FePc molecules adsorp first on regions with high lateral dipole along top-fcc direction (valley), followed by regions with lower lateral dipole (on the hill). Pentacene molecules are trapped along the top-fcc direction, too.[94] This general adsorption mechanism is applicable for other systems with periodic modulation of the work function.

Figure 3.5 depicts the work function change measured with STS (Field emission resonances) indicating a similar modulation of the work function. In this theses TBP molecules (chapter 7) and helicene molecules (chapter 8) are used as sample molecules for specific adsorption site or orientation alignment.

It was shown that this moiré superstructure influences molecular assembly. **Explain the Porphine adsorption on metal and on *h*-BN**

Molecules are electronically decoupled when adsorped on a *h*-BN spacer layer on top of a metal. The insulating *h*-BN hinders the metal to influence molecular properties by charge transfer, image potentials etc.**citation**. As a result, molecular orbitals are unperturbed and can be imaged in STM/STS.

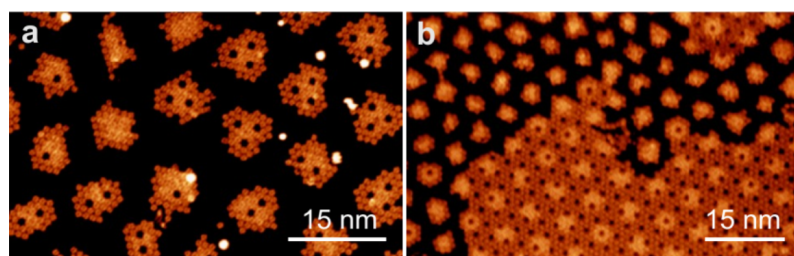


Figure 3.6. – STM topography of 2H-P adsorped on *h*-BN/Cu(111). (a) A large moiré domain guides the formation of small 2H-P islands with off center vacancies. (b) High coverage overcomes the template effect of the *h*-BN support. Adopted from [93]

3.2. Sample preparation

3.2.1. Etching copper foils

Growing high quality *h*-BN ad layers on polycrystalline copper foils requires a smooth surface, but as ordered Cu foils exhibit a root-mean-square (RMS) surface roughness S_q of up to 218 nm[95]. Steep, linear depressions, called striations are fabrication remnants due to the cold rolled foils and are observed on the surface[96]. Also some manufacturers apply a thin layer of chromium oxide for corrosion protection[95], that has to be removed prior *h*-BN growth. A common procedure to reduce the roughness of a material is to mechanically polish the surface. When an even smaller RMS of height irregularities

$$RMS \doteq S_q = \frac{1}{N} \sum_{n=1}^N (z_n - \bar{z}) \quad z : \text{height at point n}, \quad \bar{z} = \text{mean height}$$

is needed, electrochemical polishing is an alternative.

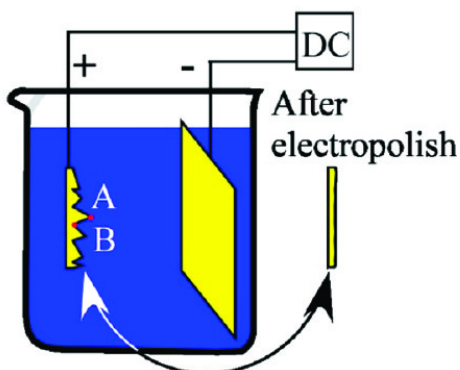
What are typical values for single crystal and foils? Check [97] and experimental images in STM of Cu(111).

The following gives a short introduction in chemical polishing as used for preparation of thin copper foils.[98–100]

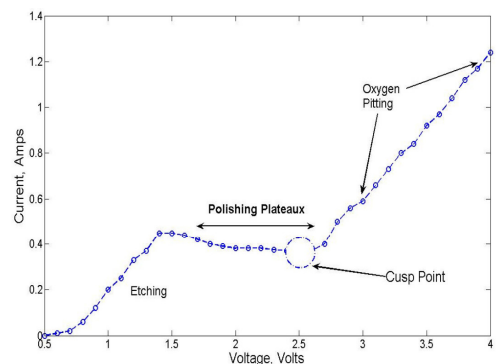
Electrochemical cell The electrochemical cell, used to etch copper foils, is sketched in Figure 3.7(a). A beaker is filled with etching solution and two electrodes are immersed. One electrode is the material to be polished (copper foil, working electrode), the other one is the counter electrode (copper in this case, counter electrode). Both are placed with 3 cm apart and are oriented parallel. In this setup the working electrode has a surface of about 1 cm², the counter electrode of about 16 cm². The beaker is filled with etching solution until both electrodes are immersed.

An electric connection is made between working electrode ($0 \text{ V} < U < 2 \text{ V}$) and the power supply. The counter electrode acts as ground. Both electrodes are fixed with alligator clamps to the wires. The current through the etchant depends on the applied potential and the etchant composition. The larger the current carried by the ionized copper atoms, the more material is transported from the working to the counter electrode.

Aqueous etching solution Many different etching solutions are presented in literature, the most widely ones are summarized by Jinshan et al. in [97]. Since the main goal is to achieve a flat surface, the resulting roughness of the surface is the most important parameter.



(a) Sketch of a typical setup used for electro polishing. A beaker is used to hold the aqueous cell medium. The copper foil and a counter electrode are immersed and connected a the + and - connections of a DC power supply. Image reproduced from [101]



(b) Current-voltage characteristic indicating different phases in the etching and polishing process. While at low voltage etching is the dominant process, a polishing plateau is formed at intermediate voltages. Exceeding a threshold (cusp point) leads to increased formation of excess oxygen in the oxygen pitting regime. [102]

Figure 3.7. – Experimental setup and voltage characteristic used for electrochemical polishing of copper foils. (a) In the process the foil is connected as working electrode (+) and opposed by a counter electrode (-). Material is then transported from the working to the counter electrode resulting in a polished foil surface. (b) Choosing proper voltage and current values within the polishing plateau is important for good results.

Table 3.2. – Used etching solutions (compare [97, p. 130]). Note the change in the removal rate due to higher limiting currents in the solution after adding ethylene glycol to the solution.

	I	II
85 % H_3PO_4	70	100
Ethylene-glycol	5	0
Deionized water	25	0
Potential [V]		1.2
Current [mA]	46	12
Roughness [nm]		5
Removal rate [$\mu\text{m min}^{-1}$]	1.0	0.26

Table 3.3. – Volume and mass fractions for copper foil etching solution.

	unit	H_3PO_4 (85%)	EG	H_2O
Dichte ρ	[g/cm^3]	1.87	1.11	1.00
Anteil	%	70	5	25
Menge gesamt	[cm^3]		150	
Menge anteilig	[cm^3]	105.00	7.50	37.50
Gewicht	[g]	196.35	8.33	37.50

Here two simple but efficient etching solutions that both result in a smooth surface and little etch pits are compared in Table 3.2. First, pure aqueous ortho-phosphoric acid (85 %) was investigated as etchant [97] with a anode-cathode potential of 1.2 V. The limiting current is 12 mA. If now Ethylene-glycol (EG) (5 % of solutions volume) and deionized water (25 %) are added, the potential range to etch at remains the same, but the critical current is increased. Although the etching rate increases by a factor of 4, the resulting roughness remains the same 5 nm, so foils etched with one of both recipes are of comparable quality. In contrast to etching recipes without EG where oxygen pitting is an issue (see ??) and more complex etching recipes (with reduced etching time but larger RMS) the chosen etchant composition (see Table 3.3) is reported to give the best results.

Redox reaction Electrons and atoms at the solid surface have higher energy states. Thus some of the atoms on the metal surface may lose electrons to form ions. These ions may also recombine with electrons and become atoms at another moment. Depending on the electronic structures, some metals (such as sodium) are easier than others (such as platinum) to ionize. Copper is relatively stable. Still, some of the surface atoms may be expected to ionize at a moment. The ionization process may be promoted when the metal is in touch with an aqueous solution because:

- Metal ions can not move in the metal electrode but can move through the solution, generating an electric current in solution when a potential is applied.
- Electrons can move freely in metal solid (electric current in a metal) but can not survive in solution because they will quickly recombine with positive ions
- Water dipoles and negative ions in solution may form a shell around the metal atom and drag the surface metal ions into the solution.

The electrode connected to the positive pole of the power supply is called anode, the one connected to the negative pole of the power supply is called cathode. When the applied voltage is high enough, electrons in the anode may be pumped out and the metal atoms on the anode surface will be oxidized (e.g., $Cu - 2e = Cu^{2+}$) and dissolved into the electrolyte solution. Under electrical field, the positive ions (cations) move to the cathode and negative ions (anions) move towards the anode. The cations may fetch electrons here and are reduced to neutral atoms (e.g., $Cu^{2+} + 2e = Cu$) at the cathode surface. Therefore, charge transfer between the two electrodes is carried out via the ion drift in the electrolyte and electron conduction in metal wire. When the copper foil to be polished is connected to the anode, dissolution is processed at certain potential. Likewise, when the foil is connected to the cathode, it will result in deposition. For electro polishing of copper, the copper part to be polished is set to be anode while the cathode can be any conductive material (e.g. copper).

The critical potential at which the oxidation / reduction starts to occur is related to the standard redox potential for a specific anode material. The redox potential E_O is a measure (in volts) of the electron affinity of a substance - its electro negativity - compared with hydrogen (which is set at 0 V). Substances more strongly electronegative (i.e., capable of oxidizing or accepting electrons) than hydrogen have positive redox potentials (e.g., Cu/Cu^{2+} : $E_O = 0.34$ V). Substances less electronegative (i.e., capable of reducing or giving up electrons) than hydrogen have negative redox potentials (e.g., Cr^{3+}/Cr^{2+} : $E_O = -1.07$ V)[97]

Voltage-current-characteristic or polarization curve On a polycrystalline metal surface there are sites, such as defects and grain boundaries, where atoms are at higher energy states. In addition, due to arbitrary crystal orientation, there are different crystalline planes with different energy states of atoms on the electrode surface. Therefore, atoms at all these different sites and planes have different standard redox potential E_O , and as a result, have different dissolution rates. Such an anodic dissolution will not lead to polishing. Instead, a crystallographic etching is produced (reference [9, 33-35] within [97]).

This is true at lower current (or applied potential). This refers to the **etching regime** in Figure 3.7(b) with $U < 1.5$ V. The plateau where the current remains almost constant with increasing voltage is referred to as **polishing plateau**.

With continuing increase of applied potential, other reactions than Cu oxidation and reduction may occur and contribute to the increasing current. These reactions produce H_2 and O_2 bubbles, which occur at or reach the anode surface. This is known as **oxygen pitting**. Gas (oxygen or hydrogen) bubbles may block Cu^{2+} ion transport and therefore terminate the electrochemical dissolution process on the area inside the bubbles. However, the residual solution on the surface area inside the bubbles may react with Cu atom and result in chemical etching. Depending on the chemical property of the electrolyte solution and the value of current density at which the electrochemical dissolution is occurring, the etching speed can be higher than the rate of electrochemical dissolution. In this case, pits will be produced on the anode and produce a rough surface. If etching does not occur inside the bubbles, or if its speed is slower than that of electrochemical dissolution process, the area inside the bubbles will remain and appears as protruding particles after the electrochemical dissolution process. In either case, a rough surface is produced. Approaches to reduce the effect of oxygen bubbling are done by altering the etching solution with different additives.

Overall, the values of the current plateau and the shape of a polarization curve depends on electrolyte solution, anode material, solution circulation, temperature, and the distance between anode and cathode. Of all the factors, the electrolyte is the most important one determining the polarization curve.

Leveling mechanisms Up to now, only the dissolution of copper surface atoms into solution and their deposition at the counter electrode was discussed. If the surface is polished evenly depends on several processes that are known as leveling mechanisms. First of all, the etching process relies on the fact that the current density (and thus the etching rate) is higher in protruding regions of the copper foil (Ohmic leveling). For an evenly wetted copper foil surface, protruding regions have less electrolyte solution between the electrodes. The lower electrical resistance causes a larger current density and thus larger dissolution rates at protruding regions.

Second, the surface geometry determines the shape of the electrostatic potential created at the working electrode. Convex regions at the surface have higher normal electric fields than concave ones, so that the force acting on a ionized copper surface atom is largest at protruding regions. Since the dissolution rate is proportional to the electric field strength, protrusions will be dissolved faster than cavities.[97, 102, 103]

It was shown that best results are achieved with following points fulfilled.[104]

- The polarization curve shows a wide limiting current plateau (polishing plateau) with low limiting current.
- Etching is performed voltage regulated.
- Good circulation of the electrolyte solution to ensure even electro polishing.
- Prevent oxygen and hydrogen bubbles created in the etching process to reach the anode surface. Parallel aligned, vertical electrodes are preferred.
- Extremely close electrodes increase the effect of ohmic leveling, though gas bubbles reach the anode surface quicker.

After etching treatment and storage After etching, the samples are rinsed with deionized water to neutralize and remove the remaining etching solution. To seal the samples from ambient moisture and oxygen, they are stored in isopropanol.

3.2.2. Sample cleaning

Contaminations are removed by repeated sputter² and anneal cycles³ in UHV. While sputter and anneal times are very similar for all substrates ($t_{sputter} \approx 20$ min to 30 min and $t_{anneal} \approx 5$ min respectively), the annealing temperature is chosen well below the melting point of the substrate but high enough to allow contamination segregation from the bulk to the surface and atomic reordering at the surface. Typical cool down temperatures $\leq 5 \frac{K}{s}$ result in a smooth, atomically flat surface with large terrace size.

Before CVD growth of *h*-BN on copper the last cleaning cycle uses annealing temperature in the *h*-BN growth regime to remove contaminations present at growth temperatures.

3.2.3. *h*-BN growth

h-BN is grown by catalytic decomposition of the precursor on hot copper substrates in UHV. Typical borazine partial pressures of 1×10^{-7} mbar and evaporation times of ≈ 5 min are used to dose 22 L while the sample is kept at 750 °C. After dosage, the temperature is kept constant for another 5 min to ensure complete transition of the precursor into the 2D *h*-BN layer and self-healing of defects created at growth. The sample is cooled down with cooling rates $\leq 5 \frac{K}{s}$ so that no wrinkles are observed at STM investigation temperatures of ≈ 5 K.

Borazine is used as chemical precursor. It is stored in an evacuated liquid cooler to maintain temperatures below 5 °C and to ensure no water contaminants are present. Both,

² $U_{accel} = 800$ V to 1000 V, $T_{sample} \approx 300$ K

³Cu: $T_{sample} = 750$ °C, Ag: $T_{sample} = 450$ °C, Au\ Mica: $T_{sample} = 450$

Table 3.4. – Evaporation and degas temperatures used for different molecules.

Name	Configuration	Degas [°C]	Evaporate [°C]
TPCN	—	—	490
TBP	single	4 h @ 200	390
	cis	—	400 °C
	trans	4 h @ 200 + 1 h @ 270	370
pyrene	cis	2 h @ 180 + 1 h @ 200 + 10 min @ 235 + 1 h @ 220	250
		1 h @ 230	265
	trans	1h @ 100 to 150 +10 min @ 170 + 25 min @ 200 + 40 min @ 220	220 to 240
Helicene	—	1h @ 100 to 150	

elevated temperature and water contaminants, cause the precursor to degenerate quickly in the storage to form boric acid H_3BO_3 , ammonia NH_3 and hydrogen. Boric acid is a white, solid powder easily recognizable in the storage. A second indication of borazine decomposition is the smell of ammonia. The design can be found in Appendix F.

3.2.4. Molecule deposition

Molecules are sublimated in UHV by organic molecular beam epitaxy (OMBE). The two/four pocket evaporators resistively heat small quartz crucibles to the chosen temperature while the unused ones are water cooled ($T \leq 20$ °C). Prior to deposition molecules undergo a degas procedure to remove unwanted chemicals from the powder. A shutter is used to choose the open pocket and allows for accurate timing of evaporation intervals.

4. Epitaxial hexagonal boron nitride on copper foils

In this chapter copper foils are first chemically polished and prepared for investigation in SEM (p. 40), AFM (p. 38) and STM (p. 39).

After CVD growth of *h*-BN with borazine, foils are investigated in STM (Figure 4.4) and XPS (compare Figure 4.5).

A commercially available *h*-BN/Cu-foil is investigated in XPS after stepwise annealing to 970 K (p. 44).

At the end of the chapter (p. 46) a use case shows that replacement of single crystals with polycrystalline foils is feasible for some applications.

4.1. Pre-treatment of Cu-foils: Polishing

Experiment realization The first attempt to etch the Cu-foil was performed with the 5%_{vol} EG, 25%_{vol} H₂O filled up with phosphoric acid. The etching was performed in a 200 ml beaker, filled with 150 ml etching solution. The potential was adjusted to be 1.2 V during the polishing process. The current through the solution changes and is typically highest when the polishing process started (120 mA).

After some minutes the foils reflectivity changes. The surface - shiny before etching - becomes hazy. After some more time the foils reflectivity improves again.

The time spend for polishing depends on the handling (like shaking the beaker or moving the foil in the solution). When no visual change to the surface is observed the etching process is interrupted.

During the etching process, as more and more copper settles on the counter electrode, the current and therefore the etching rate decreases continuously. When the beaker is moved, some of the debris on the electrode changes the electrode's surrounding and the etching rate (limiting current) increases again.

Front- and backside of the foil are suspect to different etching processes. The back side is generally more flat, the side facing the counter electrode always shows some additional protrusions.

The foil is cleaned from remaining etchants with purified water first and isopropyl alcohol afterwards in which they are stored in to avoid degradation under moist, oxygen rich ambient conditions.

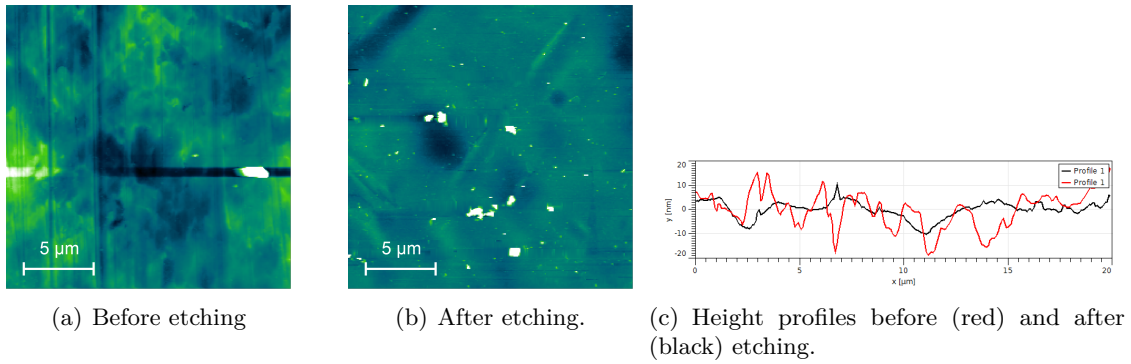


Figure 4.1. – RT-AFM topography image of copper foil as bought from Alfa Aesar (a) before and (b) after etching. (c) Height profile averaged across the lower 10 lines of (a) and (b). Roughness along the line profiles decreases after etching ($Rq_{before} = 7.3 \text{ nm} \rightarrow Rq_{after} = 3.6 \text{ nm}$). Color scale for both AFM images 100 nm, Image width: 20 μm

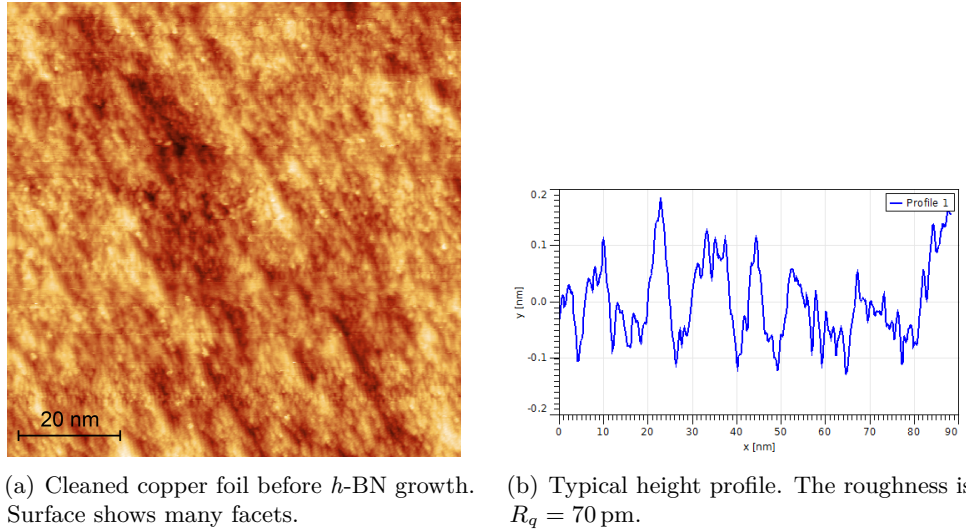
4.1.1. RT-AFM

To investigate the sample roughness for as-bought and polished foils, AFM measurements are done under ambient conditions and shown in Figure 4.1(a).

The surface of the copper foil is imaged with an uneven height distribution. As expected for a mechanically rolled foil, remnants of the production process can be seen. These striations run parallel from top to bottom and are typically narrower than 1 μm . Their depth is in the range of 10 nm to 20 nm and thus comparable to the height variation present in between them. A line profile ((c), red) averages the lowest 10 lines of the image and helps to assess the surface height. Unwanted adsorbates are imaged as bright spots and are ignored in roughness analysis that is 7.4 nm.

Figure 4.1 show RT-AFM images in the same size and contrast - before (a) and after (b) etching.

After etching ($U=1.2 \text{ V}$, $I=120 \text{ mA}$ to 250 mA for 5 h with solution shown in Table 3.3) the striations vanish and the RMS value decreases by 50 %. The over all structure changes from a heterogeneous sample height to an even height distribution with far less ridges. Those present are less steep and sufficiently separated in space to exhibit flat regions in between where h -BN may grow unperturbed. The circular depression is an result of bubbles affecting the rate of etching (compare Figure 4.3(b)).



(a) Cleaned copper foil before *h*-BN growth.
Surface shows many facets.

(b) Typical height profile. The roughness is
 $R_q = 70 \text{ pm}$.

Figure 4.2. – Cu-foil (a) after repeated sputtering and annealing cycles. (b) Height profile. Imaging parameters: (a) 3.6 V, 0.1 nA, color scale 0 pm to 600 pm, Image width: 88.6 nm,

4.1.2. LT-STM characterization

The bought and chemically polished foils are mounted on a sample holder and loaded into the load lock. It is evacuated for 2 h to 3 h, afterwards the valve is opened to the chamber. During transfer, no notable increase in the base pressure is noted. The sample was initially degassed with slowly increasing temperatures to remove adsorbates like CO , CO_2 and H_2O . After some time of degassing, the sample was prepared with repeated sputter and anneal cycles. The annealing temperatures were increased up to 800°C . The sample was cooled down and observed in LT-STM.

Further experiments were carried out to increase the cleanliness of the *h*-BN on the polycrystalline copper foil. To reduce the amount of elements coming from the body of the foil, it is repeatedly sputtered and annealed to temperatures as high as 800°C . This may have also a positive influence on the grain size and amount of corrugation. Several attempts have been made which are described in summary below. After cleaning, the sample is investigated in STM. The foil shows a in-homogeneous topography, with parts of the sample showing very flat regions while others still remain heavily corrugated and not scan able in STM. A look onto the quite heterogeneous surface reveals flat areas with a typical roughness of $\approx 70 \text{ pm}$ exist (Figure 4.2(a)). Areas with very large corrugations $\geq 100 \text{ nm}$ exist and are hard to scan in STM and certainly bad places for *h*-BN growth. Although being flat, the poly-crystalline foil shows a faceted surface with no long range order.

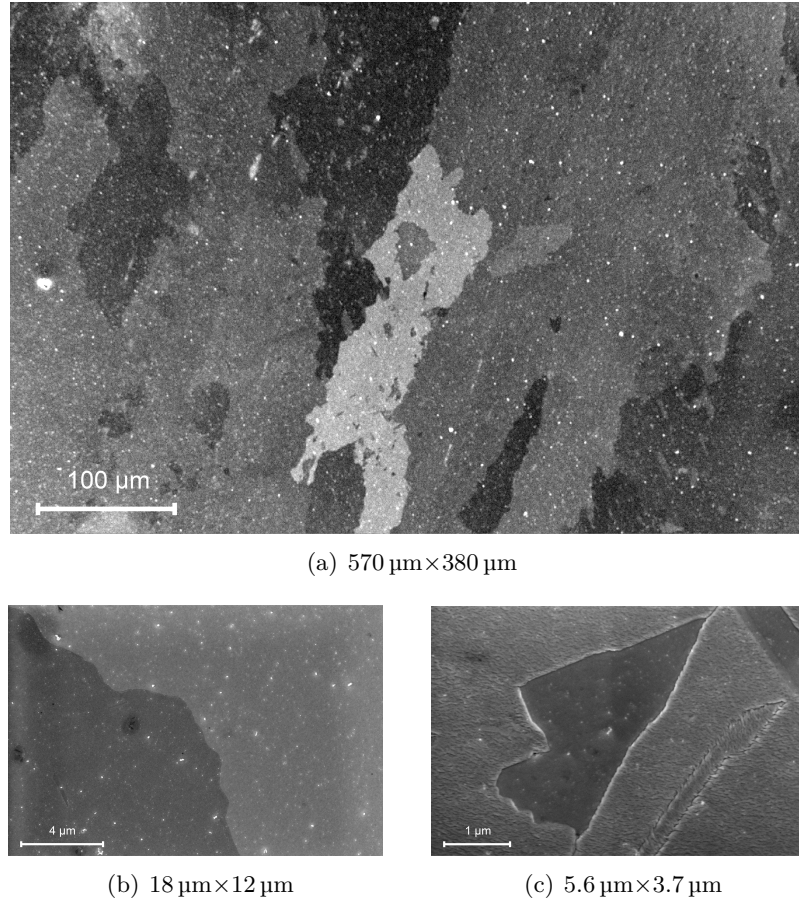


Figure 4.3. – SEM image of etched copper foil. Different contrast suggests different grain-orientation within the surface. (a) Larger image showing the contrast of different grains in the copper-foil, (b) zoom to an area with two different contrasts and their border. (c) A dark grain is embedded in an otherwise curly surface. On both, bright small features are visible and attributed to an inhomogeneous etching process. Recorded with $U=5$ keV.

4.1.3. SEM characterization

One of the foils is blown dry with nitrogen to remove isopropyl alcohol remnants and is put into the loading stage of a scanning electron microscope (SEM). After operating conditions are met, a series of images is recorded to characterize the overall surface structure of the foil.

Figure 4.3(a) shows a typical surface area. It is apparent that it is imaged in different intensities. According to [106–108] these are attributed to the copper grain orientation within the foil due to their differing resistivity. The derived grain size ranges from a few μm to several hundred μm . Many grains show distinct intensity differences compared to

their neighbors, e.g. in the center region are several easily distinguishable grains. But there are regions where a similar grain intensity makes it hard to attribute different grains to a surface area.

A border region is shown in **Figure 4.3(b)** with larger magnification. Two grains are separated by a boundary running from top left to bottom center. It is irregularly shaped and does not show a preferred direction of propagation.

Three darker circles in the top left image indicate the presence of different etching rates. Their origin is attributed to the presence of gaseous bubbles that hinder the etchant to immerse the copper surface at all times. The different surface treatment results in a change in contrast in SEM. These features are not frequent enough to co-determine the surface structure.

Smaller bright spots are spread across the image area. Here the conductivity of the specimen is larger so that more electrons are accounted for in the detector. Their size is much smaller and they appear on every image. No long range order can be found but they show similarities to features present for crystal defects after etching.

The copper foil shows different surface morphologies. While some areas appear as wavy structure in SEM, others are much flatter. **Figure 4.3(c)** displays a grain that appears darker than its surrounding and incorporates some bright small spots. The outline shows no obvious corner geometry so that the overall shape of the grain appears asymmetric.

Although the contrast between neighboring grains is clearly visible for this first example, a second smaller, elongated grain is embedded in the lower right part of the image. Its contrast resembles the surrounding, but a border is visible as dark, fuzzy lines. In contrast to the first example, the inside of this grain merges with its surrounding via many small connections. These bridges across the boundary hinder the grain distinction from the embedding grain.

Although the contrast and morphology is very similar, one can see a change in the copper grain surface as it changes its orientation. One can see this as change in propagation direction of the wavy surface. While for the large grain the waves run from top to bottom, the inset grain appears to change their propagation direction to be more horizontal.

No direct determination of the grains' facet orientation has been done due to the lack of EBSD-data in the used SEM setup.

4.2. CVD-Growth of *h*-BN with borazine

The sample was sputtered and annealed several times to temperatures of 800 °C. Before the dosage it was held 5 minutes at 750 °C. Borazine was dosed with the same pressure as before (1×10^{-7} mbar) but for 1 min and at a lower temperature of 750 °C. After the preparation the sample was kept at 750 °C for another minute. It was cooled down slowly.

4.2.1. LT-STM characterization

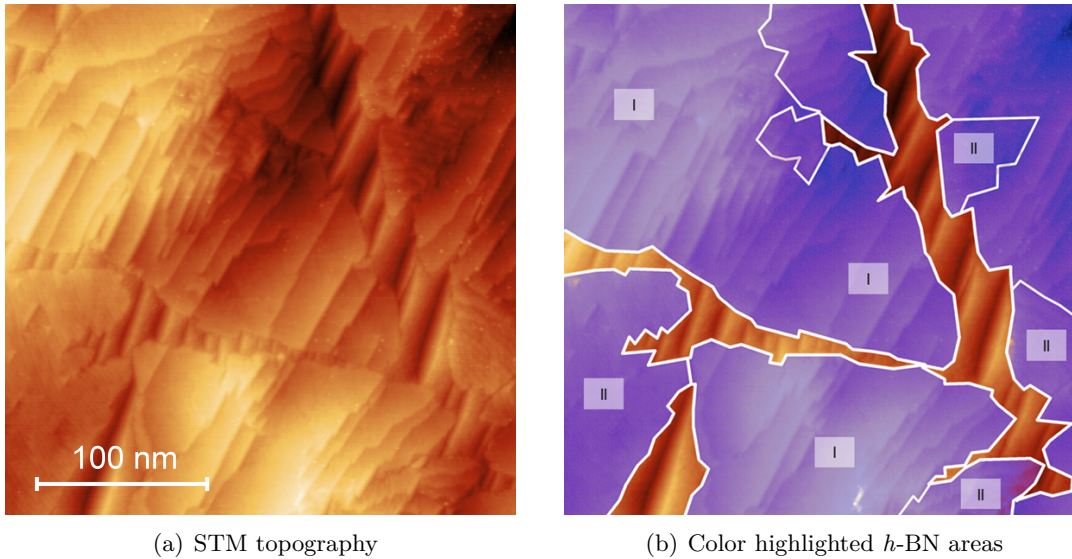


Figure 4.4. – STM topographies of *h*-BN islands that overgrow Cu-foil facets. Imaging parameters: 4.7V, 0.2nA, color scale 0 nm to 7 nm, Image width: 295 nm

Figure 4.4 shows an area with sub-ML *h*-BN coverage. As a guide to the eye, the *h*-BN islands are overlaid with a blueish hue in Figure 4.4(b). In between flat, triangular *h*-BN domains the faceted copper surface can be seen.

It is apparent that the surface structure changes between free copper and *h*-BN regions. While the facets are clearly visible on free copper areas, the overgrowing *h*-BN creates a new surface where the faceted copper surface is not visible anymore. In most of the overgrown areas wider terraces are formed that are divided by almost straight step edges that roughly follow the facets orientation.

Different *h*-BN structures are visible in Figure 4.4(a). While most islands (I) do not show much internal structure, some (II) show some apparent height variations in STM. They overgrow the facets and mask their height profile like the structure-less islands but terraces are connected by unregular shaped step edges. These typically do not follow facet

orientation and two neighboring terraces are separated by a smaller height difference. No relation between island orientation and type (I / II) can be found.

The surface structure is varying across the image. Regions with square (top left corner) and hexagonal (center) symmetric step edges are found in close proximity but only occur below overgrown areas for island type (I).

Height profiles are taken for several facets. The angle between rising and falling facet fronts is compared with typical facet angles at single crystal surfaces but no clear assignment can be done. Higher order facet orientations are discussed in **Figure A.1**. The facet orientation varies slightly across the image.

4.2.2. XPS characterization

The sample is transferred to the XPS-STM chamber and again sputtered/annealed several times to clean it properly.

The needed dosage of borazine to assemble a full mono layer of *h*-BN is derived via a combined STM/XPS measurement. Several preparations were done to understand the growth behavior of *h*-BN on the copper foil. Coverage is measured in STM while the chemical composition of the sample was assessed with XPS.

Table 4.1. – Determination of the full mono layer borazine dosage. First a saturated sample was prepared (I) and measured in XPS/STM. A sub-mono layer (II) was grown and compared to the monolayer STM and XPS results.

Prep.	Position	Area [arb.u.] [eV]	FWHM (XPS)	Anode Element	Dosage [L]	Coverage (STM)
B1s	I	191.1	3776	1.35	Mg	4736
	II	191.1	1994	1.35	Mg	789
N1s	I	398.7	5875	1.45	Al	4736
	II	398.6	3183	1.43	Al	789

When comparing the resulting coverage (STM coverage/XPS signal) (II) to the (saturated) mono layer (I) one can derive the minimal amount of borazine needed to process a mono layer of *h*-BN on the copper foil. Comparing the coverages of a sample grown with CVD, 7×10^{-6} mbar for 15min (I) and one grown with CVD, 3.5×10^{-6} mbar for 5min (II), shows that reducing the dosage by a factor of 6 does not reduce the coverage by a factor of 6, but instead by a factor of 2. Therefore (I) features a full monolayer and (II) only half of it. It follows that a full monolayer may be achieved by dosing at least 1500 L borazine on a 800 °C hot copper foil surface. Because the growth rate may certainly not be linear (less and less free copper surface to decompose borazine into building fragments

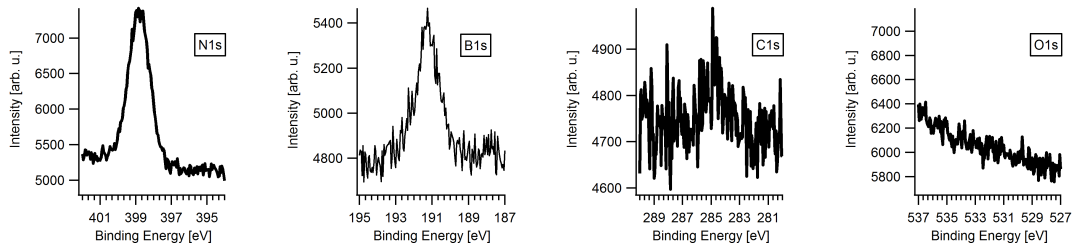


Figure 4.5. – XPS spectra for ML h-BN/Cu-foil. The peaks are at their expected positions[109] and show no additional features. No remnants of sulfur or remaining oxygen could be found.

while the layer assembles) the given dosage is a minimum estimation to achieve the mono layer.

Even though a much larger amount for borazine (4736 L) than needed for a mono layer (1500 L) has been dosed, the maximum coverage did not exceed the XPS signal of a mono layer. So the growth of *h*-BN on copper foil is self-limited (as in the case of many *h*-BN/metal systems) to a full mono layer. It is not possible to achieve layer growth with this type of preparation.

T and t dependence is not subject to investigation because the growth is supposed to follow the same mechanisms as on the single-crystal case. Quite some investigation has been done, [72, 73] to understand this process.

Commercial *h*-BN sample

The quality of the as-bought *h*-BN on copper foils[110] is examined in XPS. Results are shown in Figure 4.6.

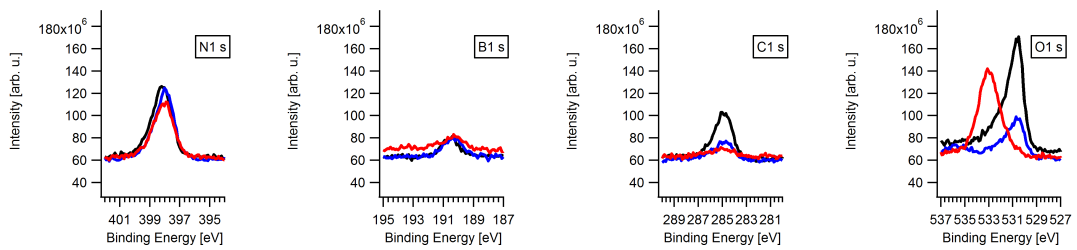


Figure 4.6. – XPS spectra of as-bought h-BN/Cu-foil sample[110]. All spectra are taken at room temperature in as-bought state (black) and after annealing to 630 K (blue) and 970 K (red).

The XPS spectra shows contribution of different atomic species. There are peaks for the

O-atoms (1s: 529 eV to 535 eV)), C-atoms (1s \approx 285 eV), N-atoms (1s \approx 398 eV), B-atoms (1s \approx 190 eV) and Cu-atoms ($3p_{1/2,3/2}$: 70 eV to 80 eV)). One would expect the shape of the 1s-peaks to be singlet-like (one peak, gauss shaped) and the 3p-peak to be a doublet (two close lying peaks with area-ratio 1/2:3/2=1:2).

There are different oxygen containing species expected to be present on the unprepared sample surface, including CO/CO_2 , CuO/Cu_2O and H_2O . They are possible surface contaminants due to sample storage under atmospheric conditions.

O1s Position varies with temperature. The signal at room temperature(black) stems from adsorbed water and CO. These desorb with increasing temperature(blue). When going to higher temperatures(red) this peak increases again and shifts to higher binding energies. Not present in self-grown *h*-BN (Figure 4.5)

C1s The C1s Peak decreases with increasing temperature and retains its position. This has the same reason as for the O1s peak (desorption of CO due to the heating). Some of the carbon remains on the surface - even at temperatures as high as 970 K.

N1s/B1s The nitrogen/boron peaks show some temperature related changes. There is little change upon annealing to 630 K, both peaks shrink, but stay almost constant in their position in binding energy (slightly shifted to lower binding energies by about 0.2 eV). Position is [N1s: 398.1 eV | B1s: 190.2 eV]. Further annealing leads to a intensity decrease.

Cu3p The copper peak exhibits an increase in area when increasing the temperature. This is because some of the water and CO adsorbate desorb and more and more copper is contributing to the signal. This peak is a doublet, so both signals come from the same chemical copper surrounding.

The $Cu(OH)_2$ O1s peak is expected to be at 531.3 eV to 531.7 eV[111] which may explain the shoulder of the O1s peak to higher binding energies (O 1s metal: 531 eV). Nitrates (NO_3) have binding energies in the range from 532.5 eV to 533.5 eV[35, p. 45]. This would imply either an replacement of nitrogen with oxygen, or some kind of oxygen on top or below the the BN layer. As proven by Simonov et al. in [112] the atomic oxygen tends to replace the nitrogen in the *h*-BN/Ir(111) system when it is annealed to 600 °C. Thus it forms $B_xN_yO_{1-x-y}$ over-layers. The longer the oxidation time the higher the amount of replaced nitrogen.

If this effect is responsible for the O1s peak at high temperatures is questionable, since the oxygen has to be cracked somehow - where no process can be thought of (no catalytic

cracking at metal surface possible - full ML, thermal energy to low to reach binding energies of O_2 .

An exchange of O with B or N would be easily visible in XPS (due to changed N/B surroundings. Not sure if the signal of oxygen is large enough for that.

4.2.3. Application: Molecular adsorption of TPCN

To test the use of polycrystalline copper foils in molecular adsorption experiments, the Cu(111) support for the *h*-BN growth is replaced by a polycrystalline copper foil. The *h*-BN layer has been prepared by a dose of 5×10^{-7} mbar borazine for 20 min (4500 L) at the LT-STM chamber. During dosage the foil has been kept at 820 °C.

Here carbonitrile-functionalized porphyrin (2H-TPCN) molecules are used as molecular building blocks, as these have been studied in the past with single crystalline supports.[113] After Co dosage they show regular metal-organic coordination networks on *h*-BN/Cu(111).

Unveiling the structure of the island beginning at its edges shows the orientation and lateral position of the molecules which is highlighted by dashed outlines in Figure 4.8(a). The molecular center is shown in black while the leg functionalization is shown in blue.

The molecules form a regular 2D network and arrange in a square unit cell with center-center distances of 2.43(5) nm. All molecules within are rotated the same and connected by their CN functions via Co atoms.

A Co atom connecting two neighboring molecules via their legs results in a distance of 2.81(5) Å between the N terminated leg and Co atom. Typical binding distances for Co-NC are reported [114, 115] and in good agreement.

Two defects are visible in Figure 4.8(b) as depressions in the otherwise regular cobalt lattice connecting the molecules. A missing Co atom leads to a symmetric, cross like depression in the apparent height. The four protrusions resemble the shape of intact functional groups.

A defect asymmetric in shape is visible in the lower half of Figure 4.8(b). Here the connection between four molecules is distorted. While three of four legs appear regular in shape and point to the central cobalt atom, a single leg appears different. This is attributed to an altered function of the leg, likely due to the loss of the pyridil group.

Few signs for porphyrin center metalization, neither many access cobalt ad atoms

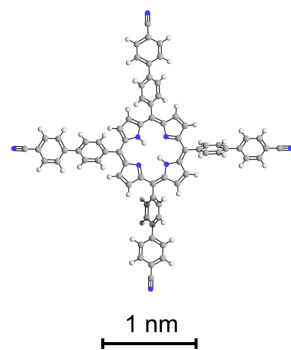


Figure 4.7. – TPCN

(additional bright spots in between the molecular assembly) are observed.

The same mechanisms are present for 2H-TPCN/*h*-BN/Cu(111)+Co [113] and show the resemblance of *h*-BN grown on Cu(111) and polycrystalline copper foils as molecular assembly support.

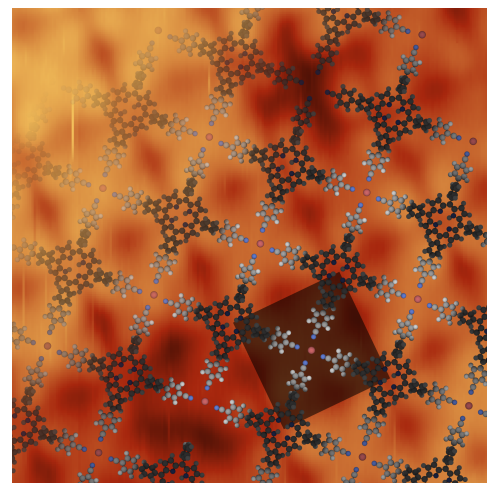
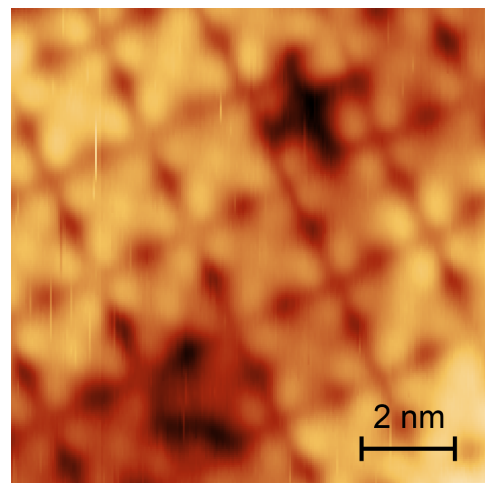
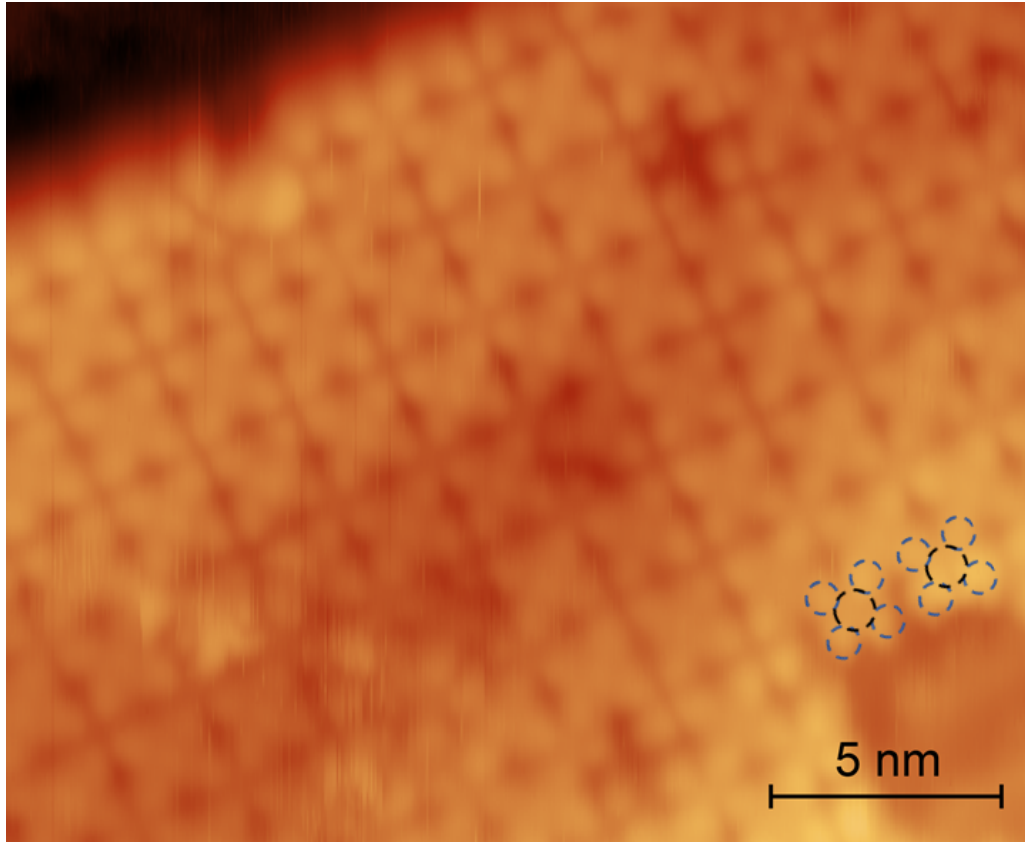


Figure 4.8. – Self-Assembled TPCN molecules after Co adsorption on h-BN/Cu-foil. Two moiré hills are partially visible in (a), imaged at 4.46 V, 0.04 nA. (c) The cobalt atoms sit between the TPCN molecules and facilitate a regular, ordered arrangement. The unit cell is shown as black square. Two defects are visible.

4.3. Summary & Outlook

- Look at Messzeit-April.ppt power point presentation
- Stufenhöhe
- Warum sehe ich kein moiré? Spannungsabhängigkeit [4V/1V] siehe 121542

The surface roughness of polycrystalline copper foils has been improved with the chemical polish approach. After polishing the foil a decrease in surface roughness of about 50 % is achieved. After several sputter and annealing cycles, *h*-BN can be grown on alike prepared foils. The quality of the grown *h*-BN is good and allows for molecular adsorption experiments, that reproduce experimental results on *h*-BN grown on Cu(111) as tested for TPCN + Co.

The prepared *h*-BN/Cu-foils were compared to bought *h*-BN/Cu-foils in XPS experiments. For the commercial available samples the binding energy for nitrogen and boron is lower by \approx 500 meV. Both show carbon peaks. While the C1s signal for the experimentally prepared sample is small, it is considerable for the bought samples and could not completely be removed via gentle heating. For the bought samples oxygen contamination is present and annealing did not show a complete removal of the contaminants.

Some foil has been mechanically polished with 4k paper and several hours of Syton polishing. The roughness of these samples has been investigated in AFM, too. It is comparable to the chemically polished ones, but always larger by \approx 10 %. Sometimes unwanted new scratches appear after mechanical polish.

To further improve the quality of the foil, one could follow the documented recipe for annealing the foil in a H₂ atmosphere (10 sscm, 1000 °C, 30min)[116] to increase the copper grain size and further smoothen the surface.

5. Pyridin-4-ylethynyl functionalized pyrene molecules on *h*-BN/Cu(111)

5.1. Abstract

The position and number of functional groups of pyridin-4-ylethynyl functionalized pyrene molecules control their self-assembly and electronic properties. To access these in UHV, decoupling of the underlying substrate (Cu(111)) is mandatory and achieved here with a *h*-BN spacer layer. As a result unperturbed HOMO and LUMO states are resolved in STM. While STS shows a band gap that decreases with increasing number of functional groups, it is not affected by their position and the molecular assembly observed STM. The gap between pronounced HOMO/LUMO states is modulated by the electronically corrugated *h*-BN/Cu(111) interface and predominantly determined by the larger shift of the LUMO states. UV/Vis measurements in solution reveal a high quantum yield of the fluorescence emission at wavelengths consistent with ab-initio DFT calculations. Finally, the ability of trans-pyrene to act as host system for cis-pyrene is shown.

5.2. Introduction

Pyrene's optical properties[117] make it a promising candidate for potential applications. 1,3,6,8-tetrasubstituted pyrenes are used in a variety of applications, including blue[118–120], yellow[119], green[121] and multilayered[122] OLEDs.

The emergence of these compounds in applications is based on fundamental research in (not only, but including) surface science conducted under conditions where unperturbed photophysical properties of the molecule can be controlled and tuned.

Optical properties are often investigated on transparent insulating bulk materials (Differential Reflectance Spectroscopy (DRS) - PTCDA/mica)[123], (Reflectance anisotropy spectroscopy - α -quaterthiophene/potassium hydrogen phthalate)[124] but are also possible on nontransparent HOPG(photoluminescence - quater – (4T) and sexithiophene (6T) films/HOPG)[125] or SiO₂ (pentacene, perfluoropentacene, and diindenoperylene/SiO₂)[126] surfaces.

These space averaging techniques are complemented with measurements on atomic length

scales where sub-molecular topographic and electronic structure are investigated by STM and STS in UHV. These need a conducting support for the molecules to adsorb on, making the choice of a suitable substrate important.

Molecules adsorbed on metal surfaces interact with their support, resulting in luminescence quenching (Photoluminescence - Quaterthiophene and PTCDA on Ag(111))[127] and broadened frontier molecular orbitals. Mediated by the presence of a metal, these exhibit considerable interaction with low-lying orbitals, changing their shape[128]. To minimize the interaction with a metallic substrate, spacer layers of insulating materials are used.

Recent years of research have increased the variety of these while a continuous decrease in layer thickness could be achieved. For example, ultrathin (6) layers of NaCl (pentacene/-NaCl)[129] and KCl[130] are utilized for direct imaging of unperturbed molecular orbitals in STM. The thinnest spacer (since it consists only of a single layer of atoms) is provided by a *h*-BN monolayer. Its large band gap is used to minimize interaction with the metallic substrate as shown experimentally[65] and theoretically (DFT – silicene/*h*-BN/Cu(111))[131]. Here self-assembly and electronic properties can be studied in STM/STS and compared with other unperturbed systems as well as with theory.

In this work we propose functionalized pyrene building-blocks[132, 133] for self-assembled regular molecular arrays on surfaces. Functionalization with pyridin-4-ylethynyl[117] makes pyrene an versatile agent for controlled self-assembly. Cis-, trans- and tetra functionalized pyridin-4-ylethynyl-pyrene was already investigated on Ag(111) system resulting in one-dimensional coordination chains, two-dimensional arrays and chiral, porous kagomé networks, where assembly is controlled by the number and position of substituents.[134] Hereinafter the influences of self-assembly, leg functionalization[135] and intra moiré position[136] on the band gap is investigated. Mandatory electronic decoupling is achieved either on *h*-BN/Cu(111) or in solution where the molecules' density of states is not influenced by a supporting metal.

Pyrenes show interesting optoelectronic properties [133, 135, 137–139] and their assembly was investigated [140–143]. Here they are used to investigate the influence of the number and position of functional groups on these properties. The very same species have been investigated on Cu(111) albeit data adsorbed on *h*-BN/Cu(111) was lacking up to this point. The nano-patterning effect of the *h*-BN substrate is used here to modulate the wide band gap of the species and therefor their optical properties.

5.3. The molecule

We investigate three different derivatives of pyridin-4-yethynyl substituted pyrenes shown in **Figure 5.1**: (a) Tetra-pyrene has four functional groups added at position 1,4,6 and 8. The point symmetric result is therefore neither chiral nor bears a dipole moment. (b) Trans-pyrene is substituted at the positions 1 and 6 (“equatorial” positions) resulting in a pro-chiral molecule. (c) Cis-pyrene is functionalized at longitudinal positions 1 and 8. With both electron rich groups being on the same side, they create a permanent dipole moment of 4.1 D in this non-chiral molecule.

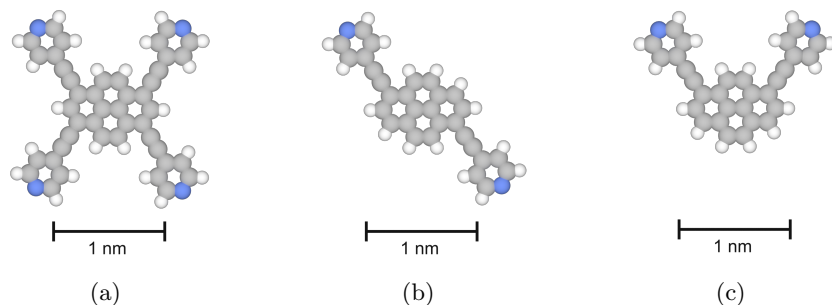


Figure 5.1. – AM1 relaxed functionalized pyrene species in gas phase. Structure of (a) tetra-, (b) trans- and (c) cis-pyridil functionalized pyrene molecule. All species are virtually flat.

The 4-yethynyl functionalization leads to a certain degree of freedom to rotate the group in plane or tilt the pyridil ring around the C-C bond connecting it to the rigid pyrene core.

As both the electronic and optical properties of molecules are quenched or at least altered upon adsorption on metal surfaces it is necessary to decouple the functional pyrenes from the metallic substrate. Therefor we grow a single layer of *h*-BN on a Cu(111) single crystal. Besides its insulating properties we have chosen this lattice mismatched system (**citation**) to make use of its spatially modulated surface potential (**citation**). Depending on the registry of adsorbate (B, N) and substrate (Cu) atoms the surface is divided in regions of larger (pore) and lower (wire) work function. This moiré is used here to fine tune the energy of molecular states. When choosing a bias voltage close to the onset of the LUMO one can easily note molecules in the pore region already contributing to the tunneling current resulting in a bright protrusion in STM although *h*-BN/Cu(111) forms a weakly corrugated layer (**citation**).

5.4. Results & Discussion

After deposition tetra-pyrene molecules assemble in dense packed islands shown in **Figure 5.2**. Every molecule within the island shows the same orientation. The unit cell is triclinic ($1.63\text{ nm} \times 1.50\text{ nm}$, 92°) and holds a single molecule. The binding motif is guided by the functional groups where a pyridil ring forms a bond with the adjacent pyridil ring of the neighboring molecule. Assuming flat pyridil groups parallel to the surface, the assembly is characterized by two intermolecular distances d_1 and d_2 between two pyridil groups, d_1 (d_2) pointing to the long (short) side of the pyrene core as indicated by black lines connecting neighboring nitrogen and hydrogen termini in the inset of **Figure 5.2(b)**.

d_1 and d_2 equal 0.288 nm and 0.254 nm respectively and are both comparable to experimental[134, p. 5] ($0.27(5)\text{ nm}$) and theoretical[144, p. 5] (0.27 nm) results (**find more of those!**). Though hard to address quantitatively in STM a small tilt of the pyridil termini is likely present to compensate for the close proximity of the H-terminated pyridil rings and is observed as minor contrast differences within the four legs of the molecule. This tilt may enable interactions between the N terminated pyridil group and the pi system of the neighboring pyridil group, giving rise to an additional binding component beside a strict N-H hydrogen bonding.

In addition to the topographic structure, STS reveals the electronic structure of the assembly. All spectra shown in **Figure 5.3(a)** are taken on the center of a molecule. Colored spectra and points (**Figure 5.3(b)**) indicate their distance to the *h*-BN pore that is recognized as bright protrusion in **Figure 5.3(a)**. The darker the color of the points/spectra the larger the lateral distance to the pore. Molecular orbital energies are indicated by yellow (HOMO) and blue (LUMO) boxes. A blue arrow illustrates the electronic gap between both. Spectra have been fitted with a gauss function after background subtraction to determine the corresponding electronic states. The energy onset of HOMO is located between -1541 mV to -1583 mV with a dependence on the position within the moiré unit cell of 42 mV . The LUMO emerges at 886 mV to 1198 mV with a notable shift of 312 mV that compares well to the reported change in work function of the *h*-BN/Cu(111) substrate.[69, 113, 136, 145] This is in good agreement with literature reporting different level alignment for occupied and unoccupied molecular orbitals where the larger shift of the LUMO mainly determines the electronic gap. It is smaller close to the pores.[146] The large gap between HOMO and LUMO (2.56 eV) benefits molecular orbital resolution (**Figure B.1**) and indicates efficient decoupling from the metallic substrate due to the insulating *h*-BN spacer.

In addition to the topographic structure, STS reveals the electronic structure of the assembly. All spectra shown in **Figure 5.3(b)** are taken on the center of a molecule. Colored

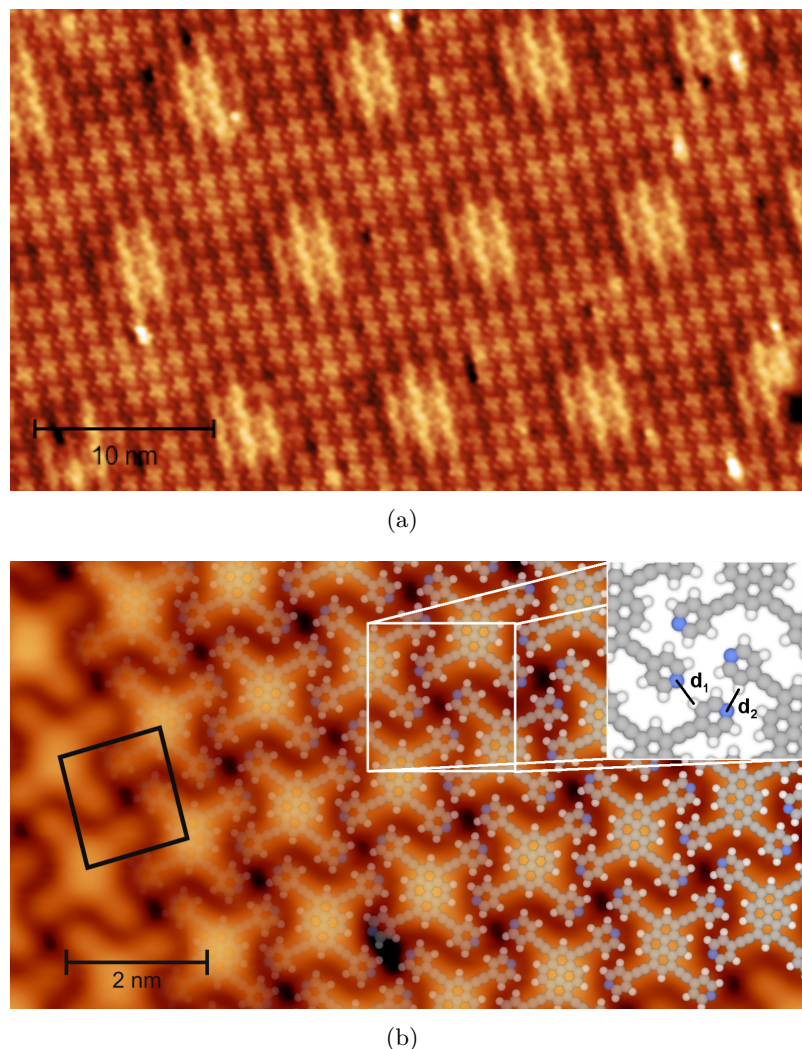


Figure 5.2. – STM topography of tetra-pyrene adsorbed on h-BN/Cu(111). (a) Hexagonal moiré superstructure visible as bright protrusions. (b) After RT deposition the molecules assemble in dense packed islands in a square unit cell (black square). Molecular model superimposed. Inset ($2\text{ nm} \times 2\text{ nm}$) shows inter molecular distances d_1 and d_2 . Imaging parameters: (a) 2 V , 0.1 nA , **Image width:** and (b) 0.1 V , 0.2 nA , **Image width:**

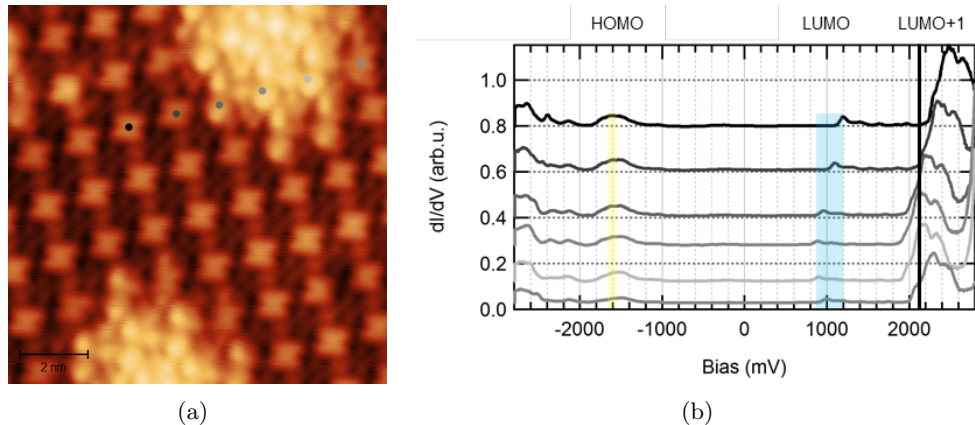


Figure 5.3. – Spatial variation of molecular energy states within the moiré of tetra-pyrene. (b) STS on varying positions within moiré unit cell. HOMO and LUMO are indicated by yellow and blue boxes connected by an arrow indicating the electronic gap. A black vertical line is drawn close to the onset of LUMO+1 states at which energy the topography in (a)) was recorded. (a) STM topography where colored points indicate positions of spectra shown in (b). Imaging parameter: 11.07 nm, 2.05 V, 0.8 nA

spectra and points indicate their distance to the *h*-BN pore that is recognized as bright protrusion in Figure 5.3(a). The darker the color of the points/spectra the larger the lateral distance to the pore. Molecular orbital energies are indicated by yellow (HOMO) and blue (LUMO) boxes. A blue arrow illustrates the electronic gap between both. Spectra have been fitted with a gauss function after background subtraction to determine the corresponding electronic states. The energy onset of HOMO is located between -1541 mV to -1583 mV with a dependence on the position within the moiré unit cell of 42 mV. The LUMO emerges at 886 mV to 1198 mV, with a notable shift of 312 mV that compares well to the reported change in work function of the *h*-BN/Cu(111) substrate.[69, 113, 136, 145] This is in good agreement with literature reporting different level alignment for occupied and unoccupied molecular orbitals where the larger shift of the LUMO mainly determines the electronic gap. It is smaller close to the pores.[146] The large gap between HOMO and LUMO (2.56 eV) benefits molecular orbital resolution (Figure B.1) and indicates efficient decoupling from the metallic substrate due to the insulating *h*-BN spacer.

Reducing the number of substituents by depositing trans-pyrene onto the *h*-BN/Cu(111) surface results in a drastic change in assembly. Now the molecules form open porous networks with a kagomé pattern (**citation**) as shown in Figure 5.4. The pro-chiral character of the molecule directly translates to the on surface assembly. A result is the formation of mirror domains (??). Each of the two consists of molecules with the same

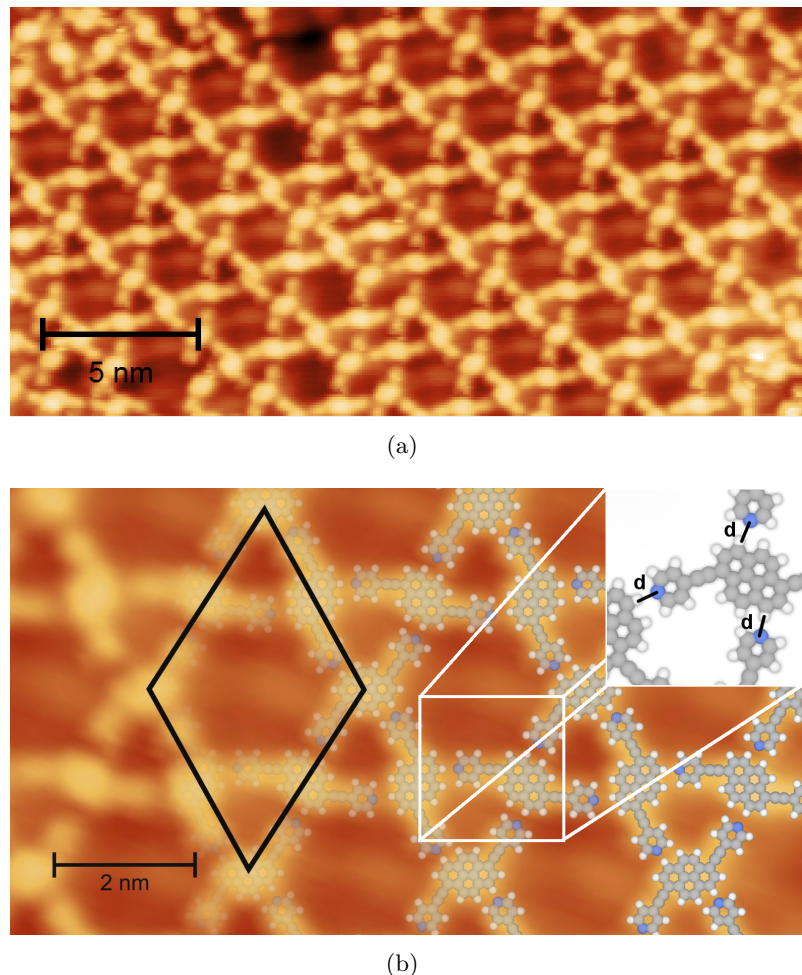


Figure 5.4. – Self-assembly of trans-pyrene on h-BN/Cu(111). (a) STM topography of two homo-chiral domains with minor lateral offset to each other resulting in a narrow transition region between both. (b) Enlarged view on one domain with overlaid models and unit cell (black rhombus). Pyridil-pyrene core connections assemble open porous networks of hexagons and triangles (kagomé lattice) with well-defined binding distances d (black lines in inset). Image parameters: 1 V, 0.1 nA, Image width: (a) 24 nm, (b) 11 nm

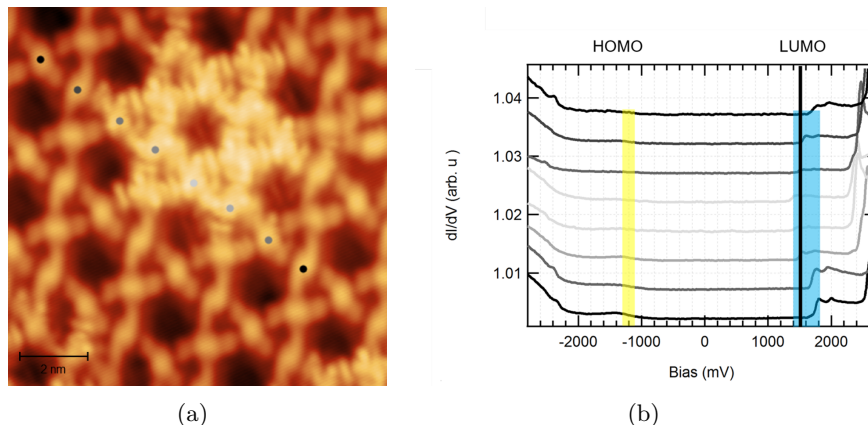


Figure 5.5. – Spatial variation of the molecular states within the kagomé lattice formed by trans-pyrene on *h*-BN/Cu(111). (a) Position and shift of HOMO (yellow) and LUMO (blue). (b) STM topography of a region where spectra across a moiré pore are taken. Colored points indicate the distance to the pores' center. Imaging bias voltage is indicated in (a) by a black vertical line. Imaging parameter: 11.07 nm, 1.6 V, 0.2 nA

chirality (homo-chiral) while no domains with mixed chirality (hetero-chiral) are observed. Although a major surface area is covered by this regular pattern, homo-chiral domains are connected by narrow intermediate regions to compensate a lateral lattice offset. The connecting region between two domains with opposite chirality is usually larger. The unit cell of the kagomé pattern is ?rhombic? with (3.04×2.93) nm long unit cell vectors and holds three molecules. The hexagonal pores feature an edge length of about 1 nm. Although not every part of the surface was regularly covered with kagomé patterns of either chirality, the binding motif is controlled by N-H interactions between the nitrogen in the pyridil legs and the hydrogen terminated pyrene-core of their nearest neighbor. The distance $d = (0.20 \pm 0.02)$ nm (black lines in inset of Figure 5.4) is smaller compared to the one reported in the dense packed assembly of tetra-pyrene and compares (how) to some literature values (**citation!**). The shortened binding distance builds up stress in the assembly, a reason for the limited domain size of the assembly. For the distance given above, the molecules are assumed to lie flat on the surface – including the pyridil rings. A way to release some of the adlayer stress is to increase the tilt or rotation angle of the pyridil group, both increasing the binding distance.

To investigate the influence of the number of substituents on the electronic structure, STS is a capable technique. For trans-pyrene the HOMO is located between -1368 mV & -1409 mV and a LUMO between 1478 mV & 1816 mV. The resulting average gap between HOMO and LUMO is 3051 mV. Molecular orbitals on pore positions of the *h*-BN layer are

again shifted to lower energies as compared to molecular orbitals on wire positions. The shift in LUMO energy (338 mV) is larger than the shift in the occupied states (122 mV). ST spectra show a large bandgap in between the HOMO and LUMO (3.05 eV), which matches DFT results (2.95 eV) very well. Compared to the electronic gap of the tetra-substituted species, the gap of the bis-substituted trans-pyrene is 378 mV larger, following the trend of increasing electronic gaps with decreasing number of functional groups reflected in the DFT calculations.

To rule out a drastic influence of the assembly on the electronic structure we deposited cis- functionalized pyrenes. These molecules form extended, well ordered, dense packed islands, composed of rows along a preferred growth direction (compare island perimeter and white arrow in **Figure 5.6(a)**). Every row is composed of molecules that interconnect like tooth in a zip fastener. Molecules on one side of the fastener show the same orientation where those in the other half are rotated by 180°. The interconnection between both is shown in the inset of **Figure 5.6(b)** and stabilized by two bonds along d_1 and d_2 . The two sides of the zip are bound via N-H binding along d_2 (0.298(10) nm). Within each side of the zip connection a bond between the nitrogen terminated leg and hydrogen terminated core of the trans-pyrene molecules guides chain formation along d_1 (0.284(10) nm, resulting in the above mentioned preferred growth direction. Stability within an island (i.e. perpendicular to the indicated growth direction) is maintained through vdW interactions of a molecules' passivated pyrene-core to its neighbors' with an average distance of 0.26(5) nm. A unit cell within the island (black rectangle in **Figure 5.6(b)**, 2.27 nm × 1.57 nm) is made up of 2 molecules. Binding distances compare well to those present for tetra-pyrene on *h*-BN where extended islands are found, too. The binding distance is comparable to those on Ag(111) as well. [134] The electronic structure of cis-pyrene is studied in STS. Cis-pyrene adsorbed on *h*-BN (**Figure 5.7**) show a HOMO located between -1606 mV & -1689 mV and a LUMO between 1242 mV & 1602 mV. This results in an average gap between HOMO and LUMO of 3.11 V. Again the shift of the LUMO is more pronounced (375 mV) than for the HOMO (84 mV).

The effect of increasing number of substituents and the accompanied change in self-assembly affects its electronic structure. For the dense packed motifs (trans- & cis-pyrene) the band gap increases with decreasing number of substituents (2.56 & 3.11 eV). Changing the surface tessellation while maintaining the number of substituents (trans- & cis-pyrene) results in almost no change (3.05 & 3.11 eV). This indicates that changing the number of substituents has a larger impact on the electronic gap than an increased screening introduced by a larger number of nearest neighbors.

The previous STS measurements show the *h*-BN's ability to effectively decouple the

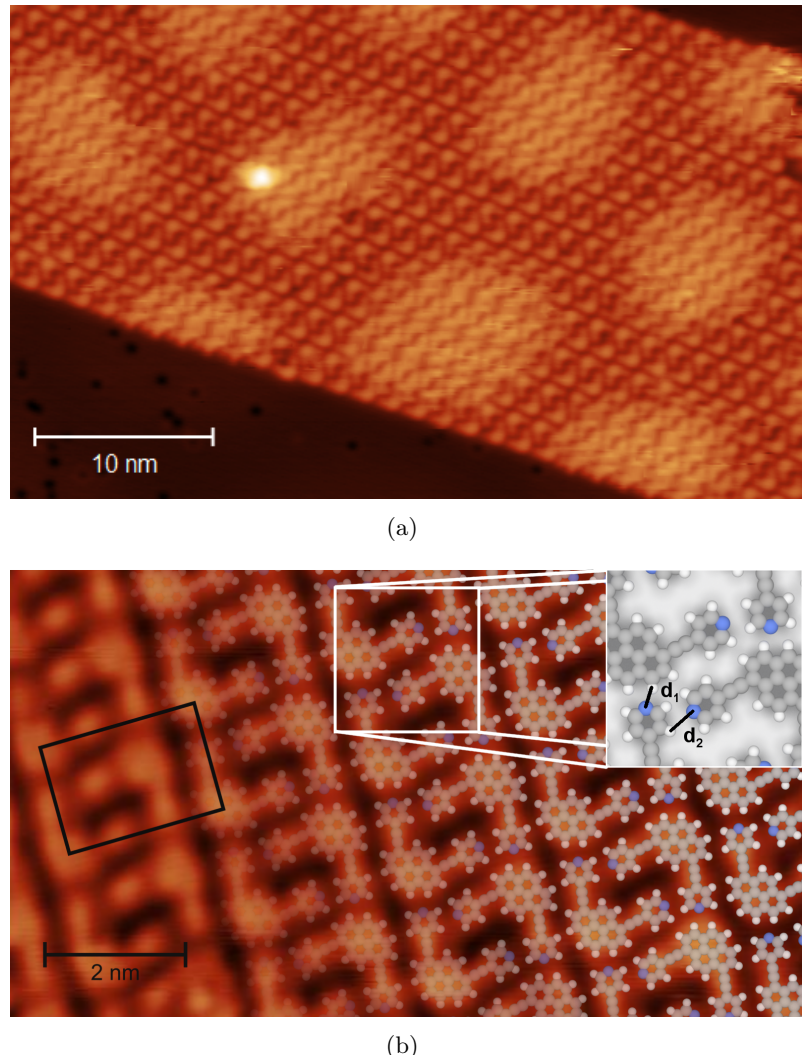


Figure 5.6. – Molecular self-assembly upon adsorption of *cis*-pyrene on *h*-BN/Cu(111). White arrows indicate the preferred growth direction. (a) The electronic corrugation of the *h*-BN (moiré) is visible as protrusions in LT-STM. (b) Overlaid molecular models of the binding motif. Unit cell is sketched as black rectangle. Enlarged inset depicts the binding distances (d_1/d_2) within this motif. Image parameters: (a) 1.38 V, 0.02 nA, **Image width:**; (b) 1 V, 0.27 nA, **Image width:**.

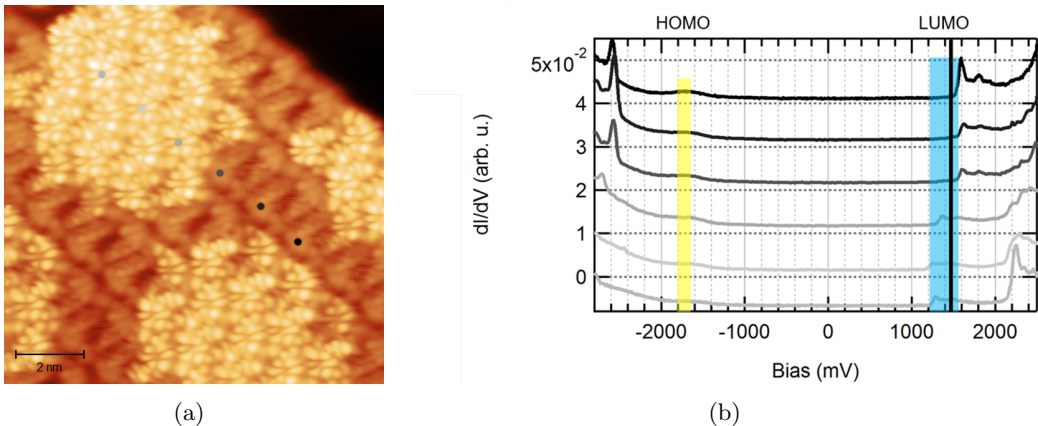


Figure 5.7. – (b) STS measurements on *cis*-pyrene on *h*-BN/Cu(111) across a moiré unit cell. HOMO (yellow), LUMO (blue) and the bias voltage used in (a) (black vertical line). (a) STM topography showing moiré pores with colored points indicating the positions of spectra in (b). Imaging parameter: 11.07 nm, 1.5 V, 0.1 nA.

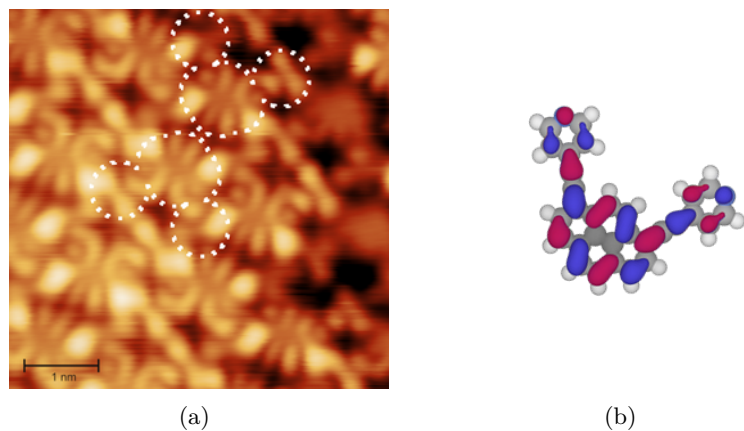


Figure 5.8. – Structure of unoccupied frontier orbital. (a) STM image recorded close to the onset of the LUMO energy. White dashed lines indicate the perimeter of two molecules. Imaging parameters: 1.5 V, 0.27 nA, **Image width:** (b) DFT-calculation.

electronic systems of molecules and metallic substrate. This can be used to image the shape of frontier orbitals directly in STM. Recording STM topography images close to the onset of the LUMO frontier orbital resolution is achieved (**Figure 5.7(a)**). A closer look (**Figure 5.8(a)**) reveals the real space distribution. For better visibility two molecules are outlined in white. One can recognize four central lobes along the short axes of the pyrene core and three dots on the leg positions. Comparing the contrast of these features with DFT calculation suggests a tunneling process where tunneling is indeed mediated by the first unoccupied molecular orbital as calculated by DFT in gas phase (**Figure 5.8(b)**).

5.5. Summary

Here we investigated a benchmark system for unperturbed pyridil functionalized pyrenes on an inert substrate in UHV. Bis- & Tetra-pyridin-4-ylethynyl functionalized pyrene molecules are investigated with STM/STS on a *h*-BN/Cu(111) surface as well as by means of UV/Vis spectroscopy in solution and ab initio calculations in gas-phase. Reminiscent of adsorption on Ag(111)(citation) substrates the pyrene core adsorbs flat on the substrate. The different assemblies on *h*-BN/Cu(111) are a direct result of the stabilizing binding motifs that can be tuned by the number & position of functional groups. Depended on these design considerations open porous networks and dense packed assemblies are formed on the surface. TETRA: For tetra-pyrene the dense packed assembly is a result of an interaction solely between pyridil legs. A rotation of the pyridil ring makes its delocalized electronic pi system accessible for the nitrogen terminated pyridil ring of its neighbors. TRANS: For trans-pyrene the position of the pyridil legs cause a kagomé network solely stabilized by connections between pyridil rings and pyrene cores, constructing a binding to stabilize open, hexagonal pores. Only the pyrene core is assumed to adsorb flat on the surface. The shorter binding distance introduces stress in the adlayer, compensated by the pyridil leg being rotated around the C-C bond and therefore increasing the binding distance. The molecules' pro-chiral property transfers to the assembly and forms two homo-chiral mirror domains. In contrast to the adsorption on Ag(111), where dense packed structures are achieved only at higher coverages(citation), cis-pyrene on *h*-BN/Cu(111) develops extended islands. The reported (citation) Ag-adatom mediated head-to-head coupling motif is not observed here, but only on the bare metal substrate. This is because in contrast to Ag(111) there are no metal ad-atoms available on *h*-BN. The binding motif within the assembly shows both, interaction between rotated legs, and towards flat adsorbed pyrene cores. STS shows prominent HOMO/LUMO features that are a result of the efficient decoupling from the metallic substrate via the *h*-BN layer. These shift in the same direction

but by different amount related to the molecules' position in the moiré. The electronic gap is predominantly determined by the larger shift of unoccupied states which are closer to fermi energy on moiré pore sites. Hence a smaller gap is created on pores while the gap is larger on wire sites, highlighting the use of *h*-BN as a work function template for adsorbates. While an increasing number of functional groups reduces the electronic gap in accordance with other reports on similar systems (citation), the assemblies' effect on the band gap is investigated by bis-substituted pyrene derivatives (trans- & cis-pyrene). Here the number of substituents remains the same and the assemblies' effect on the band gap can be investigated. A minor change between open-porous (trans-pyrene, 3.05 eV) and dense packed (cis-pyrene, 3.11 eV) assemblies (60 meV) can be linked to the increased screening for dense packed assemblies (**citation for similar systems!**).

5.6. Conclusion

The novel, optically active bis- & tetra-pyridin-4-ylethynyl functionalized pyrene molecule self-assembles on the isolating *h*-BN/Cu(111) surface in networks on the nm scale that are stabilized by an attractive interaction of pyridil legs. While cis- & tetra-functionalization results in close packed assemblies, trans-functionalization leads to open porous networks on *h*-BN/Cu(111) that may be further investigated regarding their role as host for different molecules. The electronic gap is decreasing with increasing number of substituents. The electronically corrugated *h*-BN/Cu(111) interface acts as work function template for the adsorbed molecules where the size of the gap is related to the adsorption site within the moiré.

6. Borazine functionalized coronene

- Evaluate height of molecules for RT and annealed preparations on Ag

If height changes, the molecules conformation is changed towards a adsorption geometry closer to the crystal. This means the legs need to accommodate.

6.1. Abstract

In the following the samples are prepared with increasing surface coverage of HBBNC adsorbed at RT on Ag(111) and investigated by means of STM, AFM and XPS on Ag(111). The assemblies formed upon adsorption are studied and a binding motif for sub-ML coverage is derived. After annealing the regular assembly patterns are lost and a new binding motif is observed and investigated with STM and AFM. The molecules change their adsorption behavior on Au(111) where they separate into monomers arranged in the herringbone reconstruction.

6.2. Introduction

Graphene, a carbon honeycomb lattice, has interesting aspects for applications in electronics, its band gap is often subject of interest, determining the opto-electronic properties. Different methods to tune both include placement of ad-atoms below the lattice (intercalation) and replacement of individual lattice atoms (doping). To control the defect density on the atomic level, the desired stoichiometry is determined by growing graphene from precursor molecules. These molecules form self-assembled islands, their stoichiometry being determined by the precursor design. Polyaromatic hydrocarbons are the prototype of precursor material for graphene growth.

Coronene ($C_{24}H_{12}$, known as [6]circulene or super benzene) is a polycyclic aromatic hydrocarbon made of six carbon rings to form a molecule reminiscent of a small graphene flake. It belongs to the family of circulenes where a central polygon is enclosed by different numbers of fused benzenoids. For example [5]circulene (corannulene), [6]circulene (coronene), [7]circulene and higher orders could be synthesized and show different conformation. While species with 5 or 7 benzene rings are bowl shaped, coronene is flat.

6.3. The molecule

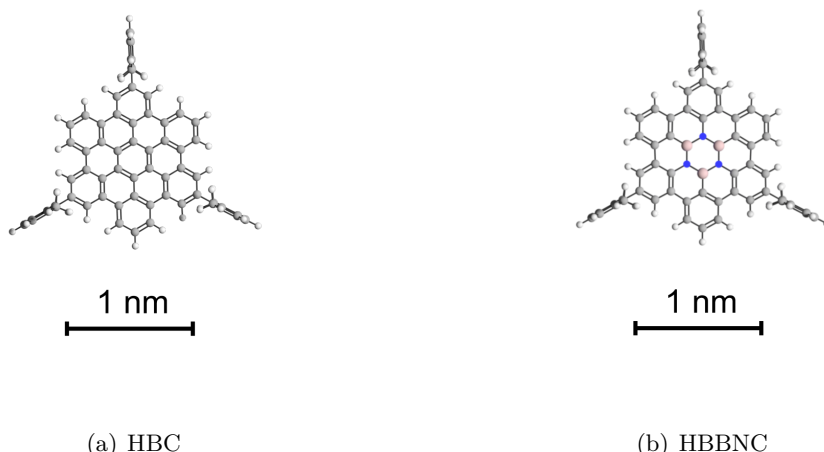


Figure 6.1. – Geometric gas-phase calculated structure of (a) HBC and (b) HBBNC. While HBC is constituted solely of carbon, the central carbon ring in HBBNC is replaced with alternating boron and nitrogen atoms. Image width: 4 nm

Here we use modifications of coronene as shown in Figure 6.1. For both species six benzene rings are added to extend the molecular backbone. Three 2,6-Dimethylphenyl groups were added to the molecules that now resemble a triangular footprint. While hexa-peri-hexabenzo-coronene (HBC shown in Figure 6.1(a)) features a central carbon ring, it is substituted by a central borazine ring for hexa-peri-hexabenzo-borazino-coronene (HBBNC shown in Figure 6.1(b)). Here the central $(BN)_3$ core is oriented to point all nitrogen atoms towards the leg functionalization. DFT calculations in gas-phase show a flat coronene center with upright standing legs for both species.

While in 2015 [147] and 2016 [148] HBBNC was synthesized, its bad solubility prohibited experiments. In 2017 the synthesis [149] of a soluble, BN-doped coronene derivative by substitution of the central carbon ring was successful.

Both species have the same number of atoms and molecular weight. The difference between both becomes apparent when calculated electronic properties are compared (in gas phase). Figure 6.2 contrasts the electrostatic potential (ESP) and the band gap of the two species that have been done in the group of Prof. Dr. D. Bonifazi.[149] The regular covalent sp^2 hybridization within the coronene core results in an evenly distributed electron density in HBC where the central region of the molecule shows considerable negative charge

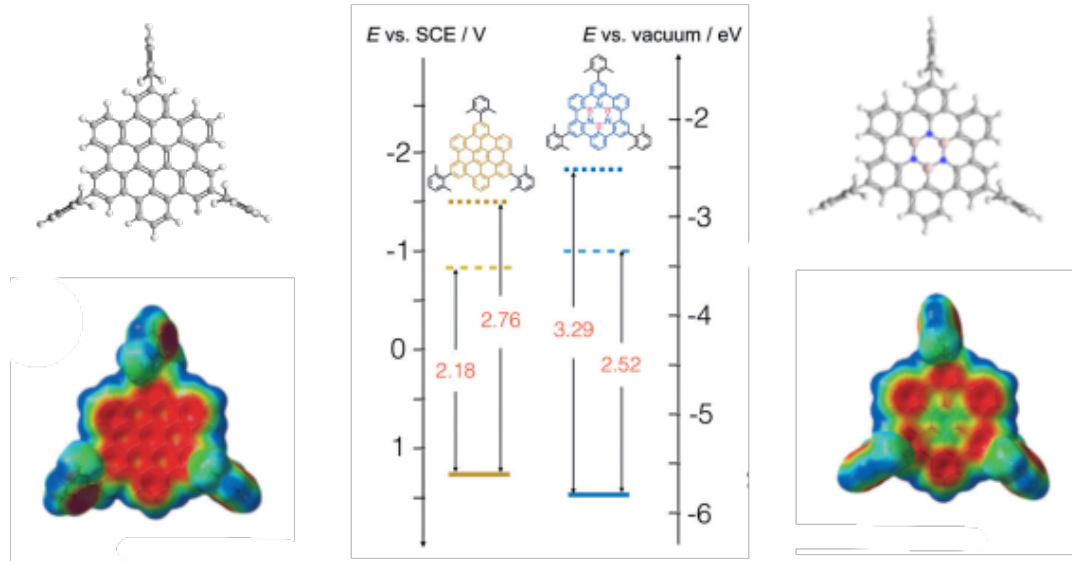


Figure 6.2. – Electronic structure of HBC (left) and HBBNC (right). The even electrostatic potential (shown as colored models) for HBC is changed for HBBNC at the center where the molecule is doped with boron and nitrogen. This does deplete the electron density at the center. The electronic gap is calculated (center) and shows a smaller gap for HBC (2.18 eV) compared to HBBNC (2.52 eV). Adopted from [149]

as a result of the molecules central π -system. Changing the central carbon ring to a borazine ring changes the ESP. Electrons are redistributed from the central borazine ring towards the outer hexaphenylene rim. In the center the aromaticity is interrupted and the extended electron π -system is altered because the ionic character in the bond between B and N. Comparable to the difference between graphene (perfect C-C bonds, conductor) and *h*-BN (ionic B-N bonds, insulator) the band gap present for HBC is 0.4 eV smaller than for HBBNC, changing its optoelectronic properties. By using HBBNC the HOMO-LUMO band gap could be widened and shows blue-shifted emission properties compared to its all-carbon counterpart.[149]

The present functionalization of the coronene molecule serves a twofold purpose. The functionalized core of the molecule is used to create 1. an sufficiently large adsorption platform for small polar molecules (like CO) and 2. an electrostatic potential surface to trap polar species. Di-Methylphenyl groups are added to lift the molecule from the substrate and guide the formation of self-assembled islands of the molecule on the surface while electronic interactions with the substrate are reduced. Molecules are provided by the group of Prof. Dr. D. Bonifazi, Jacobo Dosso performed the synthetization of the molecules.

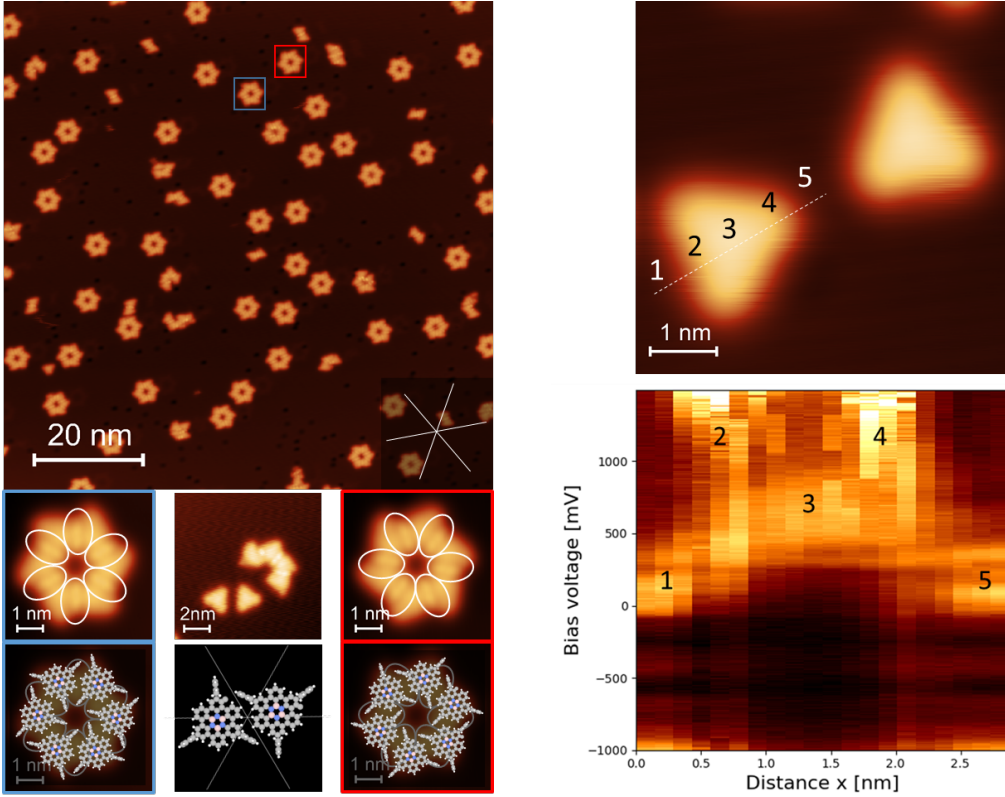
6.4. Results

6.4.1. On Ag(111)

After RT adsorption of HBBNC on Ag(111) different assemblies are found. For low coverage (left side in [Figure 6.3](#)) the dominating pattern is a hexagon in two different orientations (blue/red) with respect to the substrate. Following things can be concluded:

1. The internal structure of these hexamers can be revealed by lateral manipulation of a hexamer with the STM tip. A hexagon is made up of six intact HBBNC molecules. The monomer shape resembles a triangle with even apparent height distribution. A closer look on the modeled assembly of the hexamers shows two possible molecular orientations present for both hexamer types. The molecular orientation aligns along the high symmetry directions of the substrate. This is true for the few di- and trimer assemblies present, too. Two neighboring molecules are rotated by 180° and connect to each other with parallel edges, shifted to avoid steric hindrance. The center-center distance is 1.5(1) nm.
2. The two bright features in apparent height between two neighboring molecules (highlighted by white ellipses in [Figure 6.3](#)) only occur when two molecules are close to each other and show the right inter-molecular orientation. Otherwise only a single or no protrusion at all is imaged. Therefor these features are attributed to rotated dimethyl-phenyl rings that resemble the shape of the gas-phase calculated structure. These protrusions are best visible at negative bias voltages, but are present for a wide range of positive and negative bias voltages. This is an indication for a true geometrical change and not an electronically induced feature in STM.
3. Molecules not incorporated in a hexamer appear flat with no pronounced apparent height features above the legs. This further benefits the assumption of flexible legs, that adjust their rotation to the surrounding. While arranging flat for monomers, the close proximity in assemblies causes a rotation. Because a leg orientation may be hard to access in STM (compare EHT simulation in [Figure D.11](#)) further AFM measurements on the geometrical structure are done and show possible conformational changes in the molecule ([Figure D.1](#)).

Both types of hexamers are equally often present on the surface. From the observation of smaller hexamer fragments, it seems like the growth mechanism of the hexamers is already fixed in an early state of the assembly and depends on the adsorption site of the second molecule attaching to the first. Molecule by molecule than arranges to match the steric hindrance restrictions from the already formed parts of the hexamer. This efficient guiding mechanism leads to most molecules finish hexamer assemblies. Since only two possible arrangements for the first molecules are possible, two different hexamer configurations are



(a) Hexamer self-Assembly after RT adsorption. (b) Line spectrum for disassembled hexamer.

Figure 6.3. – Low coverage RT adsorption of HBBNC on Ag(111). (a) Molecular self-assembly. An overview image is shown on top, where crystal orientation (white lines) and two hexamer orientations (red,blue) are shown. White ellipses highlight features in apparent height that do not appear for single molecules. In between, lateral disassembly of a single hexamer into single molecules is shown. Last line shows molecular models for each hexamer orientation. (b) STM topography (top) together with a set of spectra along the points indicated across the lower left molecule (bottom). Five points are highlighted by numbers. Bottom: dI/dV spectra for each point. Imaging parameter: (a) 88.5 nm, 750 mV, 0.1 nA, Color scale: 0 pm to 400 pm, (b) 5.5 nm, 750 mV, 0.2 nA, Color scale: 0 pm to 250 pm.

found.

The electronic structure of single HBBNC molecules is investigated with STS after disassembly of a hexamer into its comprising single molecules. At the right side in **Figure 6.3** two former hexamer constituents are shown in an STM topography image. A series of twenty STS spectra is taken along the dotted line and imaged below. Numbers indicate special positions for these spectra. 1 and 5 refer to positions on the silver substrate close to the molecule. 2,3,4 are taken at the edge, center and corner of the triangular molecular footprint. There is a pronounced electronic feature around 650 mV on the molecular center, features at 1200 mV and 1600 mV can be attributed to the leg and edge positions respectively. The lateral distribution of electronic features within the molecule is further evidenced by dI/dV maps recorded at the stated values (**Figure D.6**). The surface state of the substrate (-50 mV next to the molecule) vanishes below the molecule or shifts to positive bias values. At negative bias energies, faint tip states are visible that maintain their position in energy.

Increasing the coverage leads to island formation with two dominant island types shown in **Figure 6.4**. The first can be described as coalesced hexamer configuration. All of the hexamers within an islands show the same orientation and maintain their inner binding motif upon contact. The unit cell is rhombic with an opening angle of 60° and $4.2(1)\text{ nm}$ long legs. It holds six molecules and is rotated by 30° with respect to the substrate's dense packed direction. The connection point between three hexamers shows almost every time a bright feature in STM. Since here no molecular entities reside, this is attributed to another adsorbate.

The second island type is made of chain motifs which did not show up on lower coverage. These chains consist of molecules in two orientations which were already present for the hexamer configuration. Opposed to the latter, the second type is made of two chain orientations with varying length, so that little long range order is achieved. **Figure 6.4** shows such an island together with two hexamers. The molecular model shows two parallel chains as they guide the island formation. These two are separated by $\approx 6\text{ nm}$. The clearance is filled by repeating sets of four molecules acting as connection segment between chains. The inner pair of this connection shows the same binding configuration as the chain motif, but is rotated by 30° . Two additional molecules connect those two to the chains. Their orientation is close to the molecules' constituting the chains. The close proximity of the molecules between the chains however results in the deformation of the leg functionalization and additional apparent height features in STM. Although flexible side groups allow for a denser packing, without which the molecules would not fit in the space between two chains, it hampers the exact determination of the molecular

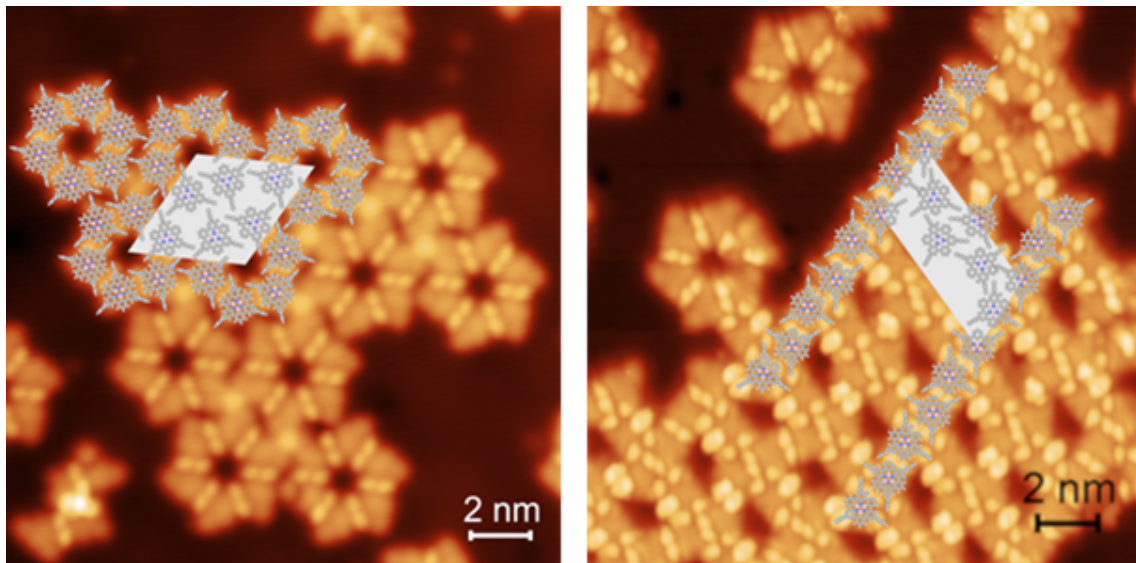


Figure 6.4. – Medium coverage adsorption of HBBNC at RT on Ag(111). While the hexagons are still present, regular assemblies with coalesced hexamers and chains occur. Imaging parameter: 20 nm, -250 mV, 0.2 nA.

assembly. The notable change to the gas phase configuration can be seen in the overcrowded region for the gas phase modeled assembly shown in the image. The unit cell however is $(5.9(1) \times 2.9(1))\text{nm}^2$ large, with an angle of 70° between its legs. It holds five molecules and its long side is close to the crystal substrate's high symmetry direction, with a mismatch of $\leq 5^\circ$. The chain length is always a multiple of 2 molecules and often shorter than eight molecules. At rare occasions, a square pattern is formed which is shown in **Figure D.8**.

Further increasing the coverage results in dense regions being formed (shown in **Figure D.9**). The dense packing results in a complex pattern of rotated side groups.

To address questions of thermal stability of the assembly and the molecule itself, annealing experiments are performed. A sample prepared at RT has been annealed in vacuum to 350°C and 420°C and is investigated with the STM (**Figure 6.5**).

After the sample is annealed to 350°C only monomers and few random agglomerates remain on the surface. Although the molecules undergo the same temperature range where hexamers are formed (from RT to 5 K) no regular assembly is imaged. Because the assembly is guided by the presence of the dimethylphenyl group a closer look to the molecular conformation is taken. Three different types can be distinguished and are shown in the inset. 1: The abundant species are molecules with a single protrusion on the leg position. 2: Flat molecules with an even apparent height at the legs are present, but are a minority. 3: Molecules with a leg missing are rarer exceptions. The unstable imaging

conditions above some of the molecules legs indicate their flexibility while the others seem to be rigidly connected to the molecular backbone and therefore imaged stable. The vanishing hexagon binding motif - observed for the RT prepared sample - underpins the importance for the molecules leg to adopt the assembly. This flexibility is not present any more after annealing to 350 °C and hexamer formation is suppressed.

Increasing the annealing temperature to 420 °C results in a percolated network where monomers coalesce and connect via their legs. Lateral manipulation attempts indicate a connection between neighboring molecules. Opposing to the previous preparations, the assembly could not be divided into single monomers. This rigid connection indicates a covalent coupling of the molecules.

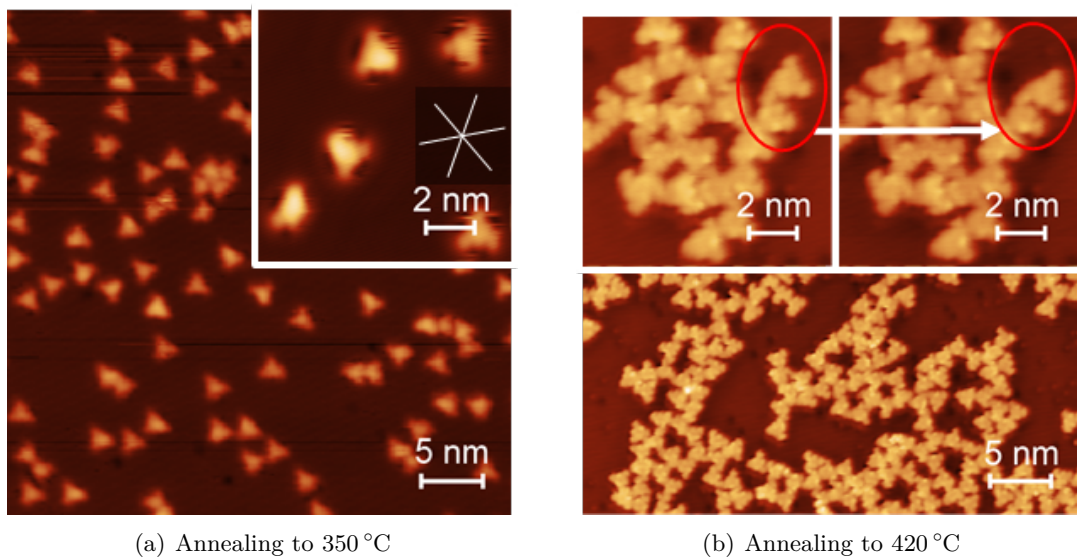


Figure 6.5. – Annealing steps of HBBNC on Ag(111) after RT adsorption. (a) After annealing to 350 °C and cooling down to LT-STM temperatures no hexamers are visible. A variety of molecular orientations and different conformations are present (inset). (b) Annealing the same sample to 420 °C leads to an unregular network where molecules are connected via their legs and not separable by lateral manipulation. Imaging parameter: (a) Width: 40 nm, 750 mV, 0.1 nA, Inset 10 nm, 500 mV, 0.1 nA. (b) Width: 40 nm, 2 V, 0.1 nA, Inset 10 nm, 2 V, 0.5 nA

Since the formation of a new bond is expected to change the core levels of participating elements (Carbon, C_{1s}), XPS measurements at the NIM-XPS are done and presented in the following. Sub-ML as well as multilayer preparations have been annealed to 420 °C to quantify a possible change in binding energy.

After RT deposition of a sub-ML HBBNC on Ag(111) a C_{1s} peak is observed at 284.94(1) eV that grows with increasing coverage and gradually shifts to 285.43(1) eV.

There is a minor shift after adsorption of a multilayer, because molecules in the second layer are facing a different environment. After annealing of the multilayer preparation the C_{1s} peak shifts to lower binding energies (284.59(1) eV), below the value observed for sub-ML preparation. A behavior typical for cyclodehydrogenation and ring closure reactions of e.g. porphyrins ([citation](#)).

Other mechanisms for a shift towards lower binding energies include the transfer of negative charge into the molecule. The more electrons agglomerated the better the atomic core charge is screened from the C_{1s} electrons. As a result the charge "felt" by electrons decreases and their binding energies with it. The opposite effect occurs for elements that strongly withdraw charge from carbon (like fluorine, chlorine), and is less present for elements like nitrogen and oxygen that only slightly shift the binding energy towards positive values. As the molecule becomes flat, it interacts more with the substrate surface. It is likely that the electron π system of the carbon rings interacts most with the substrate, due to its geometry exceeding the molecule and possible penetrating the substrate. To lower the binding energies for the carbon species, charge needs to be transferred from the substrate into the molecule. This would also imply less interaction with the metallic substrate for the multilayer preparations and an corresponding shift in the C_{1s} peak towards higher binding energies. It is assumed that the C-H bonds in the perimeter of the molecule are more reactive than the carbons bound to other carbons only and thus contribute more to the charge substitution with the substrate. [150]

The area below the peak drops to a sub-ML coverage, a clear indication for desorption of the multilayer. A covalently coupled layer would not desorp, so coupling in the lowest layer takes place after multilayer desorption. It can be concluded that annealing HBBNC on a Ag(111) surface will lead to the formation of a network stabilized via interactions that involve carbon

To further check the conformational changes in the molecule due to annealing, AFM measurements are done. nc-AFM has the big advantage over STM that it is less sensible to electronic changes in the molecule – more closely resembling the true geometric shape.

Before annealing HEXAMER COnFIguraTlOn in AFM

After annealing The fused triangular molecules that appeared flat in STM after annealing to 420 °C reveal their interesting geometric properties when investigated by means of nc-AFM. It is observed that many of the molecules appear to have their dimethylphenyl groups aligned planar to the surface. A behavior expected for a ring closure reaction between the hexabenzol groups and dimethylphenyl legs.

In the present case, almost all molecules show some defined contrast in the connection region which is an indication for a chemical interaction between the molecules. [Figure 6.7](#)

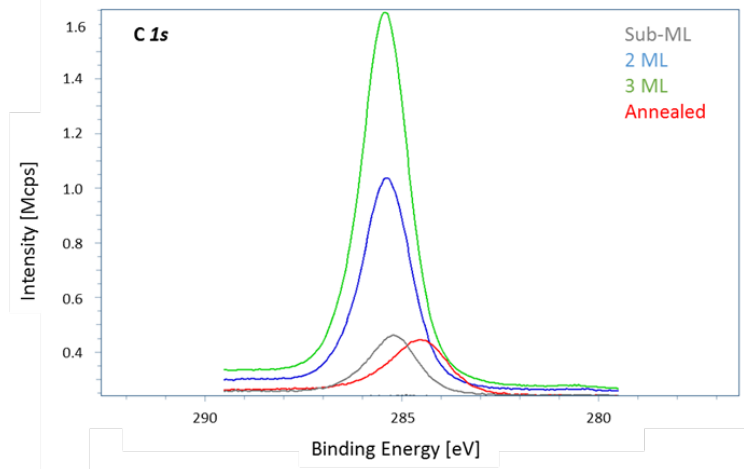
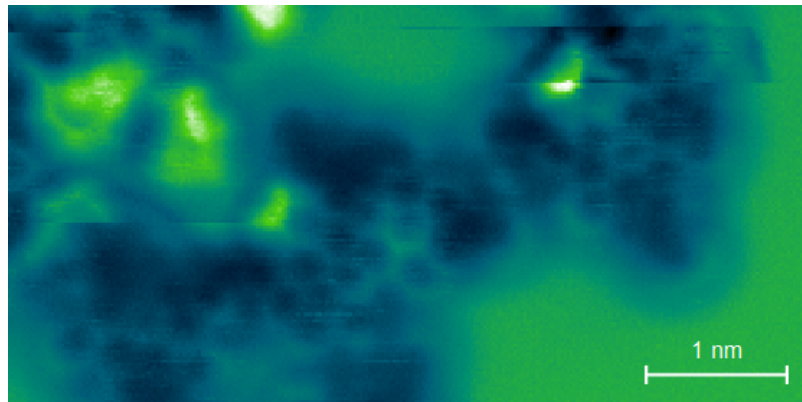


Figure 6.6. – XPS C1s spectra of HBBNC adsorbed at RT on Ag(111) for increasing coverages. Annealing to 420 °C leads to a decrease in signal and shift to lower binding energies.

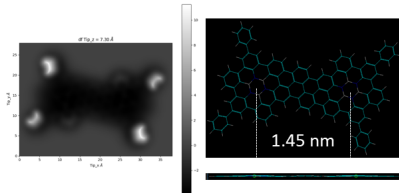
shows a dimer configuration that is used to clarify the structure of this connection with sub molecular resolution. For the two molecules a center-center distance can be measured (1.8(1) nm) and is used as benchmark for model verification. The detailed AFM image emphasizes that a link between molecules is present i) either between a leg functionalization and the coronene body (Type I: **Figure 6.7(b)**) or ii) between legs (Type II: **Figure 6.7(c)**). For both configurations the center-center distances are derived from the AM1 optimized models and result in a closer arrangement for type I (1.45(1) nm) as for type II (1.72(1) nm). A close match between the center-center distance of type II and the experimental value ($\delta \leq 6\%$) is achieved.

Both connection types increase the number of carbon rings and thus result in additional features visible in AFM. For type I the close link between leg and molecular core makes up for four new rings being formed, while a connection solely via the legs creates only one additional ring. This becomes most apparent in the planar configuration of both types (**Figure D.3**). This is not discussed in detail however, since the contrast in AFM is subject to changes in tip functionalization and scan height.

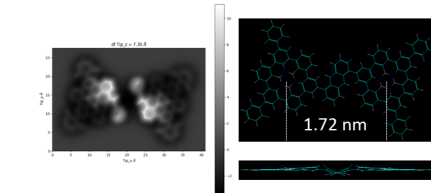
Accounting for varying number of visible rings Through assignment of geometric shape and features in AFM images a good agreement between molecular model and image can be achieved and helps to clarify the bond motif between molecules. This relies on the number and position of imaged carbon rings and fixes the resulting bond distances. Due to some flexibility of the leg functionalization the bond angle and distance may vary. In the following the influence of changing molecular geometry during the annealing process is



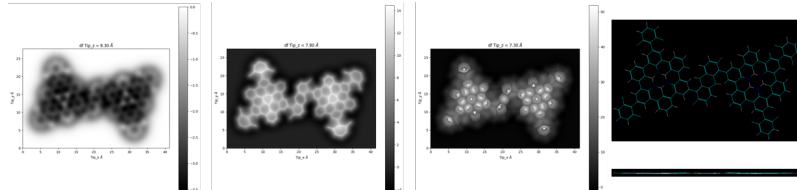
(a) Raw AFM image of HBBNC on Ag(111) after annealing to 420 °C. The distance between the two rightmost molecules that form a dimer is 1.8(1) nm



(b) Simulated AFM image for type I. Molecular centers are 1.45(1) nm apart.



(c) Simulated AFM image for type II. Center-center distance increases to 1.72(1) nm.



(d) Connection type I but with planar molecules (no AM1 optimization). Slightly smaller molecule distance of 1.70(1) nm

Figure 6.7. – Structure of an intermolecular connection between HBBNC on Ag(111) after annealing to 420 °C. AFM image (a) together with simulated AFM images of two different binding motifs. (b) Linking between leg and coronene center. This link may occur after the dimethyl groups at the phenyl legs are cleaved. (c) Covalent bond formation after dehydrogenation of di-methyl-functions. The bond is formed via the remaining carbon of the methyl group and an adjacent phenyl ring and is present twice for each link. A slight ripple present close to the covalent bond is a result from the AM1 structure optimization performed. (d) shows the same bond motif as (c) but for planar geometries and three different scan heights. The binding distances compare best for a bond via legs (configurations (c) and (d)) with a mismatch of $\leq 6\%$.

discussed briefly.

The annealing temperature not only assists the covalent bond formation between legs, but may result in an intramolecular bond being formed. Hereby the leg functionalization rotates in plane and reduces the distance to the coronene backbone, a bond between methyl group and coronene carbon ring may result in the formation of a 5-membered ring as shown in **Figure D.4**. Depending on the turn direction, two different leg orientations are possible, kinked to whichever rotation direction was chosen.

When these species now engage each other with the same bond motif as derived earlier, different bond geometries result. **Figure D.5** shows the same type of bond for pristine HBBNC molecules (a) and its ring-closed complement (b). These differ in shape of the intermolecular connection and the number of carbon ring structures within the dimer. This change however is hard to measure in AFM since geometric configuration after adsorption on a metal is hardly emphasized by present calculations and influences the appearance.

Since a ring closure fixes the leg orientation the resulting dimer shows a fixed orientation of its constituents which are modeled here either parallel or rotated by 180° with respect to each other.

A preparation where RT adsorbed molecules are annealed to 420 °C, cooled down to RT is prepared and HBBNC is evaporated at RT afterwards. See **Figure D.10** for details. It shows the two binding motifs that were observed for the annealed sample (covalently fused molecules in unregular structures) and for adsorption at RT (formation of hexamers). No mixed structures are observed, hardening the assumption that HBBNC form covalent bonds and the resulting network does not allow for connection to pristine HBBNC.

6.4.2. On Au(111)

To have the molecule adsorbed flat on the surface, another substrate is chosen. Silver is known to have a larger impact on adsorption geometries than Au(111) has.

In contrast to adsorption on Ag(111) where almost all molecules are incorporated into hexamers, molecules separate into monomers after RT adsorption on Au(111). Molecules arrange in the herringbone reconstruction visible as bright stripes in the STM image. These divide the surface into regions of fcc and hcp reconstruction.

Molecules show two different appearances. While some appear to adsorb flat in STM, others already show a protrusion above one of their legs. This protrusion is not caused by parts of the herringbone reconstruction, as two molecules on very similar adsorption sites within the reconstruction show different appearances.

The adsorption geometry of monomers is investigated. By scanning the same molecule in different heights, elevated parts of the molecule can be easily distinguished by their larger

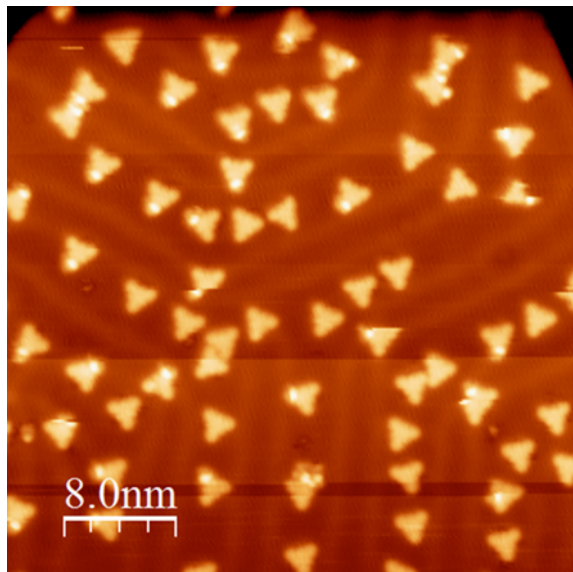


Figure 6.8. – STM topography image of HBBNC on Au(111)/Mica. **Stripes** of the herringbone reconstruction divide the surface into regions of fcc and hcp stacking order. Only monomers form after adsorption at RT. **Scalebar, Imaging parameter:** 11.07 nm, 1.5 V, 0.1 nA.

interaction force with the tip (the involved larger frequency shift is shown as protrusion in nc-AFM images). These show that the dimethylphenyl legs of a monomer do not lie flat on the surface but have an elevated and lower lying part. While their initial orientation on the surface is likely determined at adsorption, the legs are able to flip under the influence of the AFM tip (see Figure D.2) and change the adsorption angle of the molecule. This is imaged as bright edge where the lower part of the rotated dimethylphenyl group lifts the molecule. The effect is most pronounced when neighboring groups rotate in opposite directions. This is underpinned by calculated AFM images (Figure D.1) that show the same feature pattern after gentle rotation of the side groups.

6.5. Summary & Discussion

Investigations with STM are performed for similar molecules on Au(111) by [147].

HBBNC has been deposited at RT on Ag(111) and Au(111). On Ag(111) different assemblies are formed depending on coverage. Although the molecule is not chiral in gas phase, low coverage adsorption on the Ag(111) surface leads to the formation of hexagon assemblies with corresponding mirror images. During adsorption the molecule rotates its legs to a more planar configuration with the substrate.

6. Borazine functionalized coronene

This compares to previous studies of coronene on Ag(111), where close packed assemblies were formed at a distance of 1.15 nm which is of course smaller due to the smaller molecule.[151] Hexa-peri-hexabenzocoronene assembles in close packed hexagonal structure on HOPG with $a = 1.37$ nm.[152]

The close resemblance of HBCs assembly suggests that the orientation of single molecules with respect to the substrate is given by the symmetry of the molecule alone and that HBBNC's BN core does not influence the adsorption compared to the carbon center of HBC. These findings compare well with previous results. Coronene was investigated with STM on Ag(111) [151, 153]. Together with hexa-peri-benzocoronene its orientation at sub-ML regimes is determined by the molecular symmetry matching the substrate high symmetry directions[154].

Although tried intensely, the calculated band gap of 2.52 eV is not observed and may point to a broad HOMO feature that blends with the often observed tip states. Charge transfer between molecule and metallic substrate is possible and may be evidenced by future calculations.

Increasing the coverage in the high sub-ML regime leads to island formation with different unit cells. The interaction between molecules is always guided by the orientation of the di-methyl functional groups and results in chains formation.

Interestingly, exceeding monolayer coverage lead to stable second layer formation only for the HBBNC species, while no second layer is observed at RT adsorption of HBC on Ag(111), although multilayer coverage of hexa-peri-benzocoronene is reported and believed to change the adsorption geometry to a tilted configuration[154] where increasing molecular $\pi - \pi$ interactions between molecular planes cause a 0.3 eV shift of the molecular levels toward higher binding energy[155].

Annealing a multilayer HBBNC preparation to 420 °C leads to a chemical coupling between molecules that is pointed at by combined STM, XPS and AFM measurements.

7. Nitro functionalized Porphine

7.1. Abstract

Within this section, TBP molecules with are investigated. The number (1-2) and position (single-, cis-, trans-configuration) of the very same functional group is changed. Although first the results on metal surfaces are presented, one of the ideas of the following experiments is to use the dipole moment of the single functionalized molecule to orient it along the work function change of a *h*-BN/Cu(111) sample.

Preparations with the single nitro functionalized species are done at RT on Cu(111), *h*-BN/Cu-foil and Ag(100). The Ag(100) preparation was heated to 170 °C.

Preparations with the trans functionalization are performed at RT on Ag(100) and Cu(111) where the last was heated to 120 °C.

Evaporation of the cis functionalization were not performed, although tried intensively no molecules were sublimated in the OMBe and found on the sample. This indicates strong intermolecular interaction within the crucible like cluster formation or polymerization, which have to happen before the molecules sublimate.

Similar molecules have been investigated on a reconstructed Au(111) surface [156].

7.2. Introduction

Tetrapyrroles like porphyrins and phthalocyanines play important roles in biological systems [157]. Both species are able to incorporate metal atoms that control the function. Not only are they interesting model systems to study interaction towards a (metallic) substrate[158–160]. Their use in metal-organic frameworks highlights the use of scientific knowledge to design "real world" sensor applications[161].

Tert-butyl functionals have been used in a variety of molecules [162]. Due to their bulky nature, they electronically decouple the porphyrin's delocalized p-orbital system from the metallic surface just by lifting the molecule. They may undergo heavy conformational deformation when outer influences (like metalization of the central porphine core) act on the molecule [163]. Switching capabilities are well investigated [164] and it is possible to switch them with a voltage pulse through the STM tip [165]. Experiments with similar

molecules investigate the heat-induced formation of 1D and 2D conglomerates on a Au(111) surface.[166]

7.3. The molecule

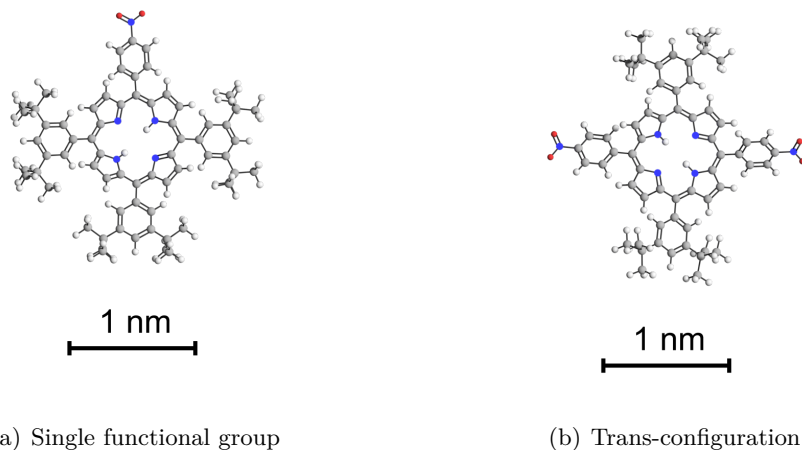


Figure 7.1. – Functionalized tert-butyl-phenyl-porphines. (a) shows a single functionalized porphine molecules. An additional function may be added in trans- (b) position.

- Free base nitrophenyl - 5,10,15 Tri [di-[tert-butyl]-phenyl])-porphyrin has 3(2) di-tert-butyl-phenyl groups attached to the porphine macro cycle at the meso-positions of the molecule. The free meso-positions are occupied with nitrophenyl groups as shown in Figure 7.1(a) If more than one functional group is present, one can distinguish between trans (Figure 7.1(b)) and cis configuration (??), whether the two functional groups are opposite or neighboring.
- The appearance of STM data is correlated to the molecular configuration according to [167] meaning that the lobes consisting of (3,5-di-tert-butylphenyl) are imaged as bright protrusions, while the functional nitro group is imaged fainter. This holds true for cis- and trans-substituted molecules[156].
- Tert-butyl groups can rotate to form flexible legs. Interaction with the substrate results in adsorption-induced conformational changes.[168]

Drawings for various functional groups and molecules can be found in [169].

7.4. Results: Single leg functionalization

7.4.1. on Cu(111)

When adsorbed at room temperature, TBP distributes equally on the surface, forms unordered islands and decorates step edges. Molecules orient their main axis (connecting line from one di-tert-buyl-phenyl ring across the center to the nitrophenyl ring) along the dense packed substrate rows most often, less are 15° of (**(Refer to image?)**). Several binding motifs (as shown in Figure 7.3) are observed, namely

- A dimer, where molecules lie “head-to-head”, functional groups (NO_2) pointing at each other
- A “triangle”, where molecules are rotated 120° and functional groups point towards a shared center. Although this motif does not occur very often (or at least under very flexible angles), it is given as an example where the functional groups point to each other. Similar motifs (like 3 molecules in 90° are observed together with other orientations.
- Chains with different length appear, where the nitro group of molecule 1 points to the di-tert-butyl group of molecule 2 (“head-to-tail”). At the connection points, molecules appear brighter, promoting a physical overlap of the two molecules.

Center-center distances are typically 1.78 nm (for the head-to-tail) and 1.5 nm for the head-to-head connection.

“head-to-head” To model the occurring binding motifs, deformations of the molecules have to be taken into account. Because nitro groups face each other in the “head-to-head” connection, their distance would be to small to facilitate a similar binding mechanism like for the TPCN on copper (where copper surface ad atoms promote binding between nitrogens), so no free space between the facing nitro groups is observed. Because the distance is so small, the phenyl ring (with attached nitro group) rotates by 45°, to make the phenyl ring stand upright. When the second molecule does the same, both match

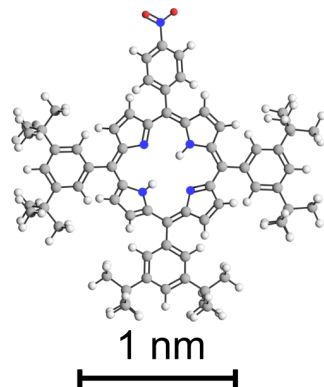


Figure 7.2. – TBP with three di-tert-butyl and a single nitro phenyl group added at the meso position.

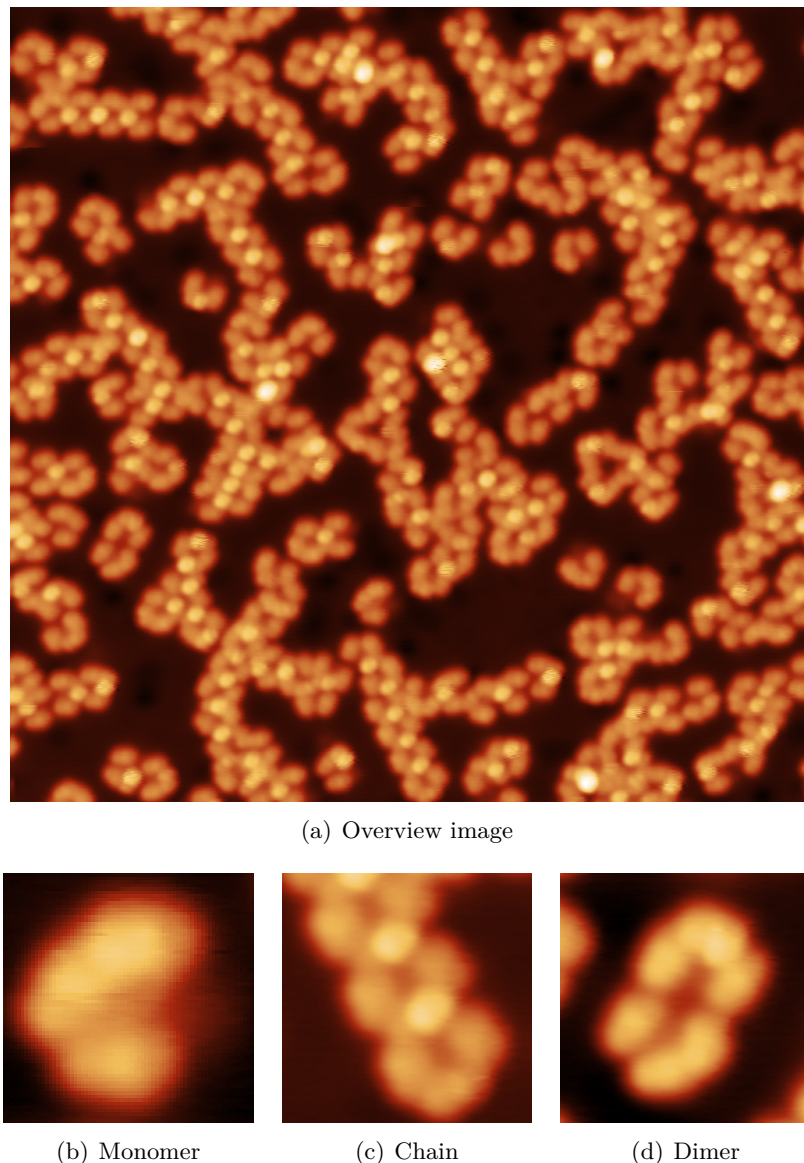


Figure 7.3. – RT adsorbed single nitro functionalized TBP on Cu(111) and their most abundant binding motifs. (a) Each of the binding motif can be found as well in the overview STM data, as well as in the enlarged images (b-d). All images recorded with -500 mV , 0.1 nA , color scale 0 pm to 300 pm . Image width: (a) 44 nm , (b) 3 nm , (c) & (d) 5 nm

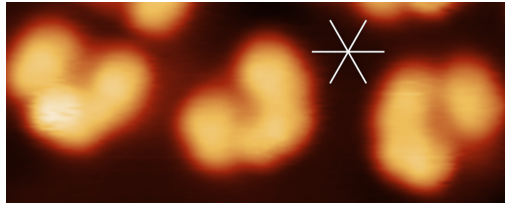


Figure 7.4. – Different appearances of TBP on Cu(111). While most of monomers (center in image above) show even heights with their tert-butyl functions, some (left) do posses an elevated tert-butyl group. The orientation of the tert-butyl groups is aligned with the high symmetry crystal direction (indicated by white lines) most often. Image recorded with -500 mV , 0.1 nA . Image width: 10 nm

each other with negligible lateral shift, reproducing the STM images best. Similar binding motifs are reported in [170] for non-covalent cross linking of dicarboxylic acids in hydrogels. Although the situation on a metal-surface may change considerably (only 2D - no 3D, metal present - will change chemistry), the observed binding motif matches very well.

“head-to-tail” The chain motif “head-to-tail” is reconstructed using the unique contrast of the TBP molecule. When the center-center distance is measured, molecules are modeled that distance away from each other. These models show a physical overlap between molecules, which is not possible because of steric hindrance. To solve the problem, the nitro-group (head) of one molecule is rotated by 35° out of the plane (like pulling the nitro-group upwards, not rotating the group left/right).

Flexible tert-butyl-groups Another interesting fact is that butyl groups of TBP seem to orient themselves (as far as steric hindrance allows for) along the dense packed rows of the copper substrate. Again, one has to be careful when reconstructing geometrical information from STM images. Like the distortion of legs in the TPCN molecule, this rotation can be explained by a rotation of single butyl groups. Although the phenyl ring remains at the same position/rotation, tert-butyl groups are allowed to rotate such that they appear in different heights. Because STM (constant current) follows equipotential lines, the whole phenyl-di-tert-butyl-complex looks rotated in plane, although it may not be. This is confirmed in literature[171, 172].

7.4.2. on Ag(111)

Molecules are adsorbed on Ag(100) at RT. The resulting conglomerates are shown in Figure 7.5(a). The very most surface area is covered with unregular patterns. The step edges are covered, assuming a sufficient large mobility at RT to move from the terrace to

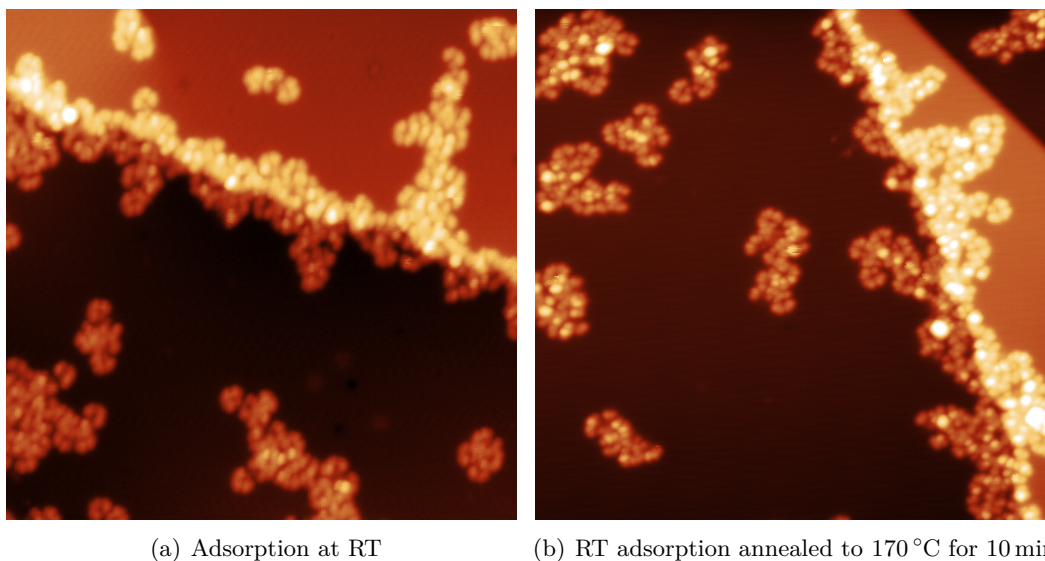


Figure 7.5. – Annealing after RT adsorption of molecules on Ag(100). (a) STM data of molecules adsorbed at RT (Scan parameters: $U_b = 1\text{ V}$, $I_t = 0.03\text{ nA}$), (b) After annealing for 10 min to $170\text{ }^\circ\text{C}$ (Scan parameters: $U_b = 1\text{ V}$, $I_t = 0.1\text{ nA}$). Color scale 0 pm to 600 pm. Image width: 44 nm.

the nearest step edge. The only free step edges observed are due to tip formings on the sample surface since these are created after the molecules are stuck on the surface because of the low temperatures during measurement.

Annealing The RT adsorption is annealed to $170\text{ }^\circ\text{C}$ for 10 min and investigated in LT-STM again (Figure 7.5(b)). No big changes are visible, neither in the formation of new assemblies nor in the distribution of molecules at terraces or at step edges. No chain formation could be observed.

Assembly Since no regular self-assembled islands are present on the surface, more detail is put on the only repeating binding motifs on this surface. One of this configurations resembles a cross (??), while the second one is a variation of the dimer motif (Figure 7.6).

While on copper, two molecules may form a dimer in head-to-head or head-to-tail configuration, on silver some form tetramers from two parallel merged dimers. While one dimer looks like two “U”’s with facing open ends ($\in \Theta$), the other dimer is shifted to closely match the first dimer best and lies parallel.

Another motif looks like a cross and shown in Figure 7.6(f). Build out of four molecules, where each is rotated by 90 ° with respect to its preliminary neighbor. One can distinguish

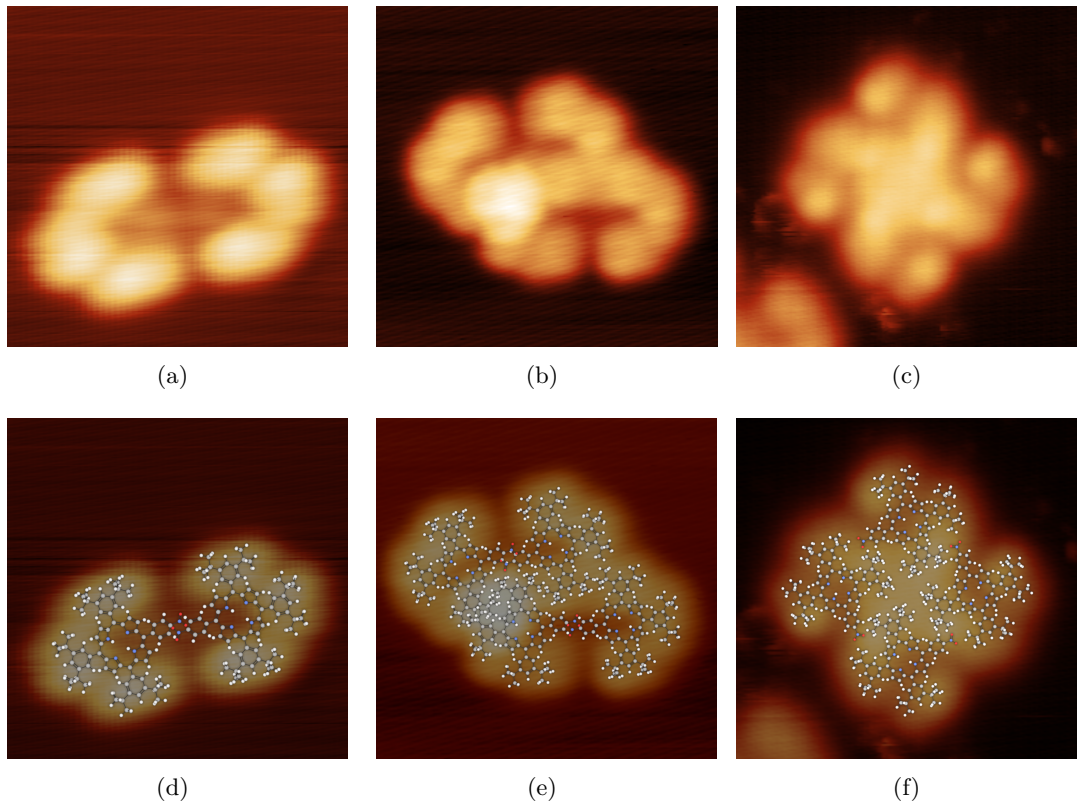


Figure 7.6. – Different observed binding configurations of TBP adsorbed on Ag(100) at RT. (a) STM data of dimer configuration. Scan parameters: $U_b = 0.328 \text{ V}$, $I_t = 0.035 \text{ nA}$, Image width: 5 nm. (d) Model representation. (b) STM data of two coalescent dimers. Scan parameters: $U_b = 0.097 \text{ V}$, $I_t = 0.035 \text{nA}$, Image width: 6 nm. (e) Model representation. (c) A cross consisting of four TBP molecules. Scan parameters: $U_b = 2.3 \text{ V}$, $I_t = 0.035 \text{ nA}$, Image width: 10 nm. (f) Model representation. Color scale in all STM images 0 pm to 300 pm

four di-tert-butyl groups from the central cross. Although there is no atom directly in the center, the cross looks bright in its center (in STM), which is somehow counterintuitive.

Flexible Tert-Butyl-Functions Figure 7.6(b) shows an interesting feature of the tert-butyl functions.

- Butyl groups within TBP feature different contrasts (look rotated), while the orientation of the butyl-groups doesn't follow the close packed substrate rows. —————— find image and explain
- TBP molecules have been heated on silver substrate for 10 min at 170 °C. The resulting sample did not feature chain-formation or improved ordering.

Spectroscopy Some spectroscopy could be achieved that shows different typical features for different areas in the molecule. Note that the spectra were done for molecules sitting on a Ag(100) surface. There is a clear indication, that the macrocycle of the molecule contributes to the broad peak in the dI/dV data at around 1 V, while the nitro groups dominate the spectra at around 600 mV. Look at the corresponding .pptx file for the spectra and the corresponding IGOR-files dimer/quatermer1-2 for the spectra.

7.4.3. on *h*-BN

***h*-BN grown on Cu(111)** Further experiments have can done to investigate the behavior of TBP on *h*-BN. When adsorbed on *h*-BN/Cu(111), molecules show a high mobility that makes the molecules move away from the *h*-BN islands. Some molecules could be resolved at defects or close to the perimeter of the *h*-BN islands. This is in line with other observations for adsorbates ((CITATION)). Adsorption temperatures as low as –170 °C have been used to lower the molecules' energy pool, but diffusion to free metal areas occurs and no molecules remain on the *h*-BN surface.

***h*-BN grown on Cu-foil** Molecules adsorb on the BN surface and STM imaging is hard due to molecules that can be moved on the rather 'slippy' surface of the insulating BN. Nevertheless some agglomerations of the molecules leave free BN spots where no molecules are. As the preparation of the BN should result in a closed BN layer on top of the Cu-foil no movement of molecules to free Cu areas should be observed, making these free regions BN regions. Why

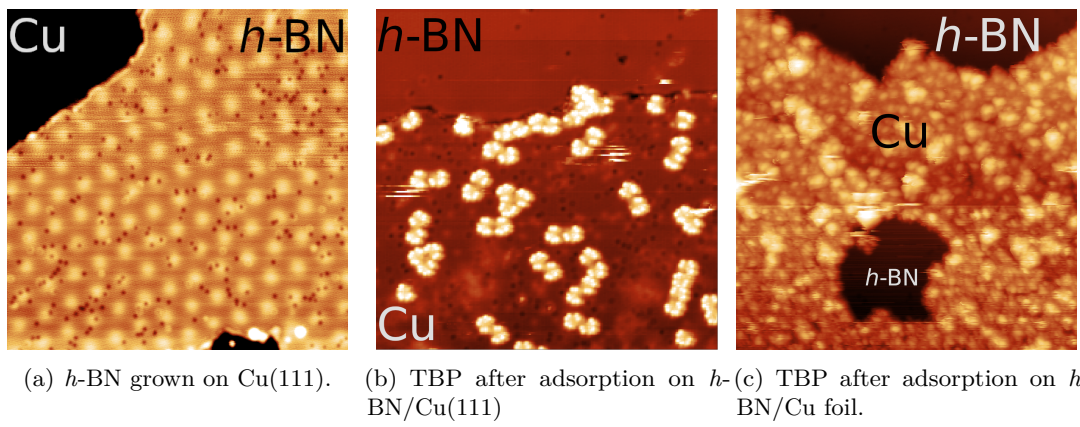


Figure 7.7. – STM topographs of h-BN grown on copper with subsequent molecular adsorption. (a) shows a h-BN layer grown on Cu(111) by CVD. (b) shows the sample after evaporating TBP molecules at RT. (c) shows empty h-BN islands grown on the polycrystalline copper foil and molecules on a copper terrace. Scan parameters: (a) $U_b = 2.273\text{ V}$, $I_t = 0.048\text{ nA}$, color scale 0 pm to 100 pm. (b) $U_b = 1.074\text{ V}$, $I_t = 0.033\text{ nA}$, color scale 0 pm to 300 pm. (c) $U_b = 2.585\text{ V}$, $I_t = 0.032\text{ nA}$, color scale 0 pm to 1500 pm. All images are 40 nm wide.

the molecules are not distributed homogenously on the BN remains topic to speculation. Spectroscopy has been tried intensively but without reproducible results. Unlike the adsorption on Ag(100) and Cu(111) no formation of di- and quaterners has been observed.

7.5. Results: Double leg functionalization

7.5.1. on Cu(111)

When depositing trans-TBP on Cu(111) at room temperature no long range ordering can be achieved. The molecules arrange rather arbitrarily as can be seen in Figure 7.9(a).

The molecules tend to connect in a **defined angle** to its next neighbor, forming different binding motifs. These are predominantly different kind of chain formation (see figure 7.10).

- The molecules are ordered such that they form a straight chain (Figure 7.10(a)).
- The molecules arrange in chains, but each molecule

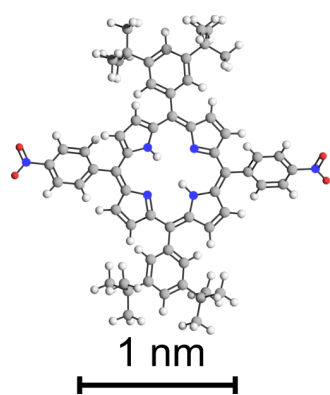


Figure 7.8.

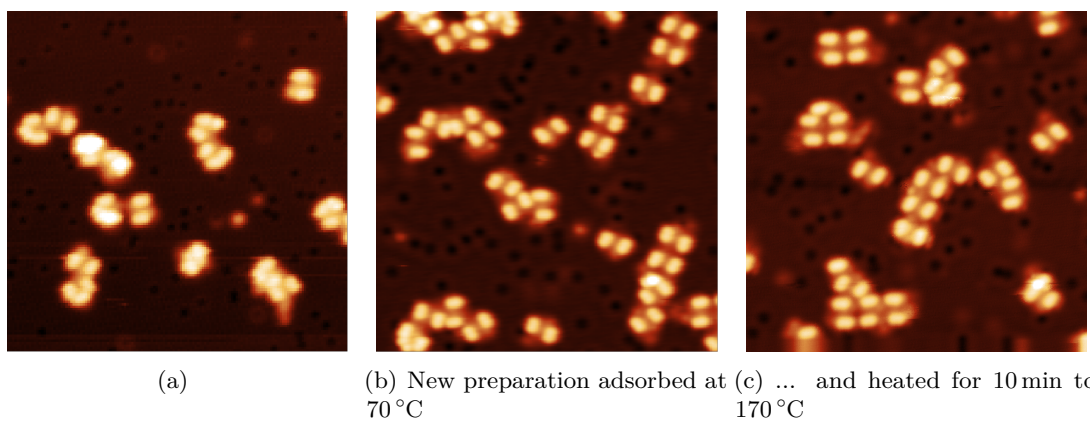


Figure 7.9. – Molecules adsorbed on Cu(111) at RT and subsequently annealed to different temperatures. (a) Adsorption at room temperature did not show extended long range order. (b) Adsorption at 70 °C and (c) annealing to 170 °C for 10 min improves the chain length slightly. All images are 40 nm wide. Scan parameters: (a) $U_b = 1.2$ V, $I_t = 0.041$ nA, (b) $U_b = 0.5$ V, $I_t = 0.038$ nA, (c) $U_b = 0.522$ V, $I_t = 0.021$ nA

has an offset of about a half of its width to the next neighbor or the molecules attach in chains, but show a kink. **Figure 7.10(b)**

During modeling Figure 7.11 several points became clear.

- First consider the even apparent height of the di-tert-butyl groups. It indicates that both groups in a legs have comparable heights and it is likely that the phenyl ring bearing these groups is rotated for an even alignment of the tert-butyl groups with regard to the substrate level.
 - Orientation of di-tert-butyl phenyl groups is the same within a single molecule but alternates (by $\approx 10^\circ$) in neighboring molecules in a chain. This is indicated by blue and green lines in Figure 7.10(a), each representing a common orientation.
 - Second the minor contrast variations in the central porphine core change as the orientation of the di-tert-butyl-groups. Free base porphine core is likely to adsorb with its axis - formed by opposing nitrogens in the core - aligned parallel to the dense packed crystal direction[173]. In the present case, the molecule is lifted from the substrate by the bulky di-tert-butyl groups. Hence the porphine core interaction with the crystal substrate is considerable lower than in the 2H-P case. Still, every second molecule has the same orientation, while neighboring molecules are rotated by 30° .

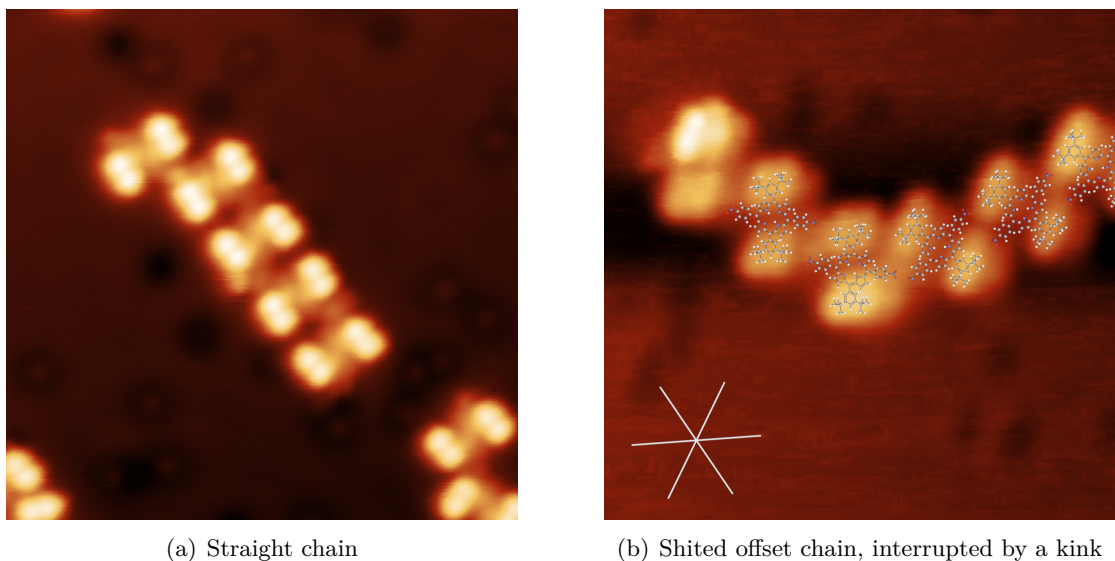


Figure 7.10. – All motifs exist at every temperature, although the chain length increases with temperature. It also looks like the chains are getting more offset- and kinked-like chains than at lower temperatures.

- The gap between di-tert-butyl-phenyl groups of neighboring molecules is larger on one side of the chain than on the other and shows a larger apparent height (white arrows in Figure 7.10(a)). Although identification of surface ad-atoms is not straightforward with an STM, they are believed to originate from the copper surface.

The best fitting model consists of molecules with a center-center distance of 1.9(1) nm

Having a closer look to the nitro groups, one recognizes a close proximity of these to each other. Also note the light protrusions in between two adjacent molecules' butyl groups (adatom?). If the legs are rotated by just 15°, the nitro groups would point to these protrusions. This rotation costs not much energy and is about 25 kJ/permol ((
please cite something, value is for rotated phenyl ring at a porphine core I
guess)). Considering these protrusions as Cu-ad atoms (already occurred in chapter ?? as protrusions in between TPCN chains which may change their position in discrete position in the molecule.) This Cu-ad atom may direct the binding of the nitro groups towards it, making them bend outwards. The position of the cooper atom itself may rely on its registry to the substrate - preferring a threefold coordination site as known for copper ((
citation))).

The second motif is a chain motif, too. Orientation of molecular axis and dense packed substrate atom rows are the same and again the di-tert-butyl groups orient along them. The difference is a lateral offset between the molecules to shift each of them by half a

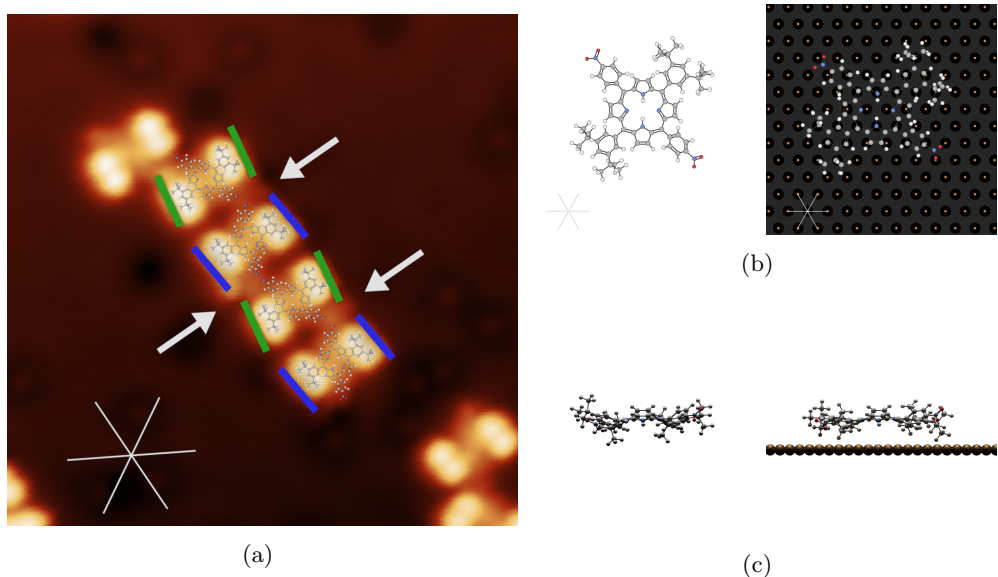


Figure 7.11. – Straight chain binding motif on Cu(111). (a) shows an STM image together with the dense packed row indication of the substrate (white lines). Colored bars indicate the rotation of the di-tert-butyl-groups. Arrows point at places where ad-atoms are considered. (b) Top views (6 nm wide) showing the molecules geometry in gas-phase (left) and after adsorption and assembly (right). Although the exact adsorption site is not known, it is considered to be on a bridge site as for 2H-P/Cu(111). (c) Side views of above shown configurations.

molecules width. The center-center distances are 1.9(1) nm. It is harder to quantify a possible orientation of the nitro-phenyl groups, since as well straight as well as bended configurations match the assembly. In this binding motif, stable connections between molecules are most likely due to nitro-phenyl groups pointing to di-tert-butyl groups and therefore stabilizing the assembly.

7.5.2. on Ag(100)

Unit cell When adsorbed on a square (100) silver surface, the molecules interestingly arrange in a trihexagonal tiling (see figure 7.12). The molecules at the perimeter of this island is nicely distinguishable and continuing their regular pattern to the center of the island results in an accurate description of the assembly. The unit cell is determined to be _____ and the hexagonal unit cell is shown in Figure 7.12(b), bearing three molecules.¹

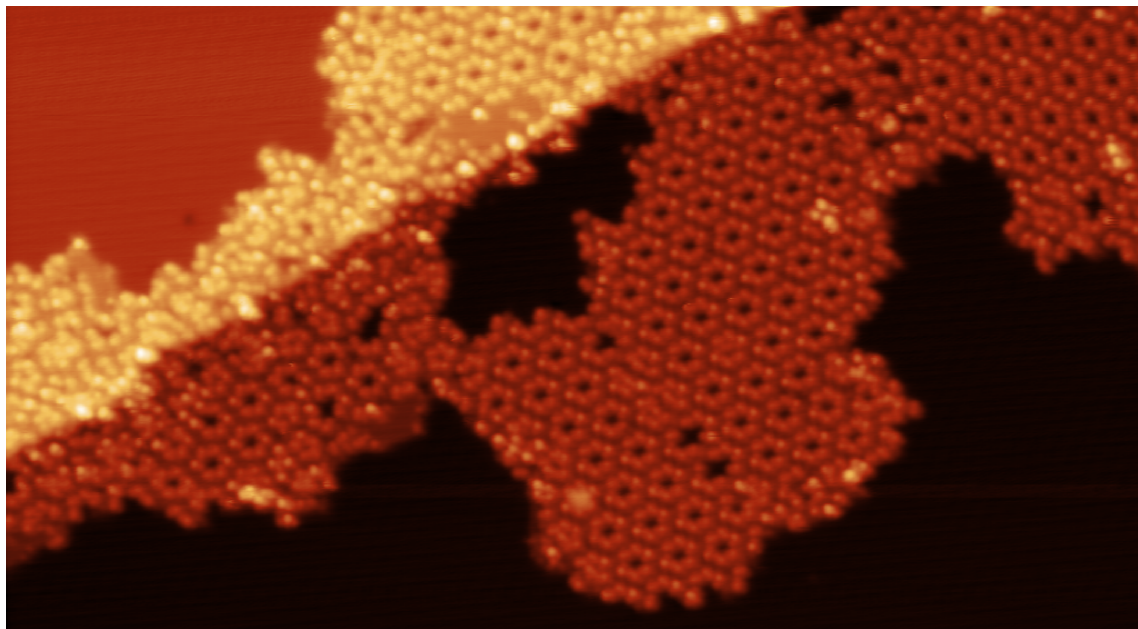
¹Similar open porous network can be created, e.g. cyano functionalized triarylamines on Au(111) [174].

Molecular orientation The molecules are arranged so that each molecule has one of its di-tert-butyl-groups in one hexagonal pores and the other in the neighboring one. Each pore is made up of six molecules arranged on a hexagon with _____ long edges. Each vertex is occupied by a single molecule, neighboring molecules on the hexagon are rotated by 60°. The pores are created by free space where the di-tert-butyl-groups point towards each other. The nitro-phenyl groups point towards the intermediate space where smaller triangular openings are formed. At their edges the nitro-phenyl groups connect to the neighboring di-tert-butyl groups.

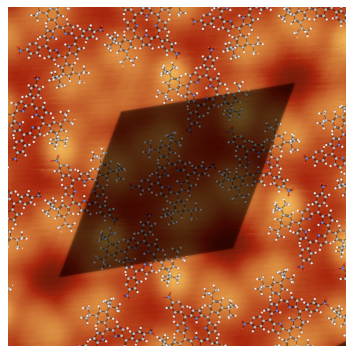
Considering a former orientation calibration on Ag(100) where the direction of the dense packed crystal direction was determined, the orientation with regard to the substrate is given as white lines in **Figure 7.12(b)**: The long and short axis of the unit cell (marked as green cross in (b)) is almost collinear, just differing by less than 10°. Since the calibration was done with another preparation the angle calibration may not be 100 % accurate because the sample was moved in the meantime. That may result in a little angle uncertainty. Please see **Figure C.3** in Appendix C TBP for a detailed image.

Contrast within single molecule A closer look to the geometries in high resolution STM data gives clue to the rotation of the di-tert-butyl-groups and is visualized in **Figure 7.12(c)**. Focusing on the STM contrast of a single molecule, one can see that it is dominated by the di-tert-butyl-groups on both sides of the molecule. These look like small triangles in the STM with a single brighter protrusion enclosed by the footprint. The bright protrusion is never on the same side of the triangular footprint thus the di-tert-butyl-groups are believed to be rotated in two different directions - lifting opposite parts of the functional group.

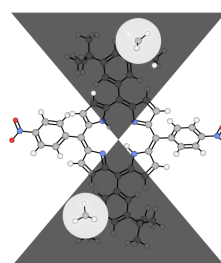
Domain boundaries The observed domain boundaries are imaged in **Figure 7.13**. On both sides the regular tiling is proceeded, but both are shifted with respect to each other by _____. This offset results in the wrong alignment of molecules from one domain with respect to the other domain and a discontinued growth. The resulting free area at the domain boundary is occupied by molecules from one domain that bear the wrong orientation the proceed the growth of the second domain and vice versa. This can be nicely seen in **Figure 7.13(c)**, where the misalignment of one domain (left) with respect to the other (right) causes two cavities to open up between the two (lower image part). While these two are unoccupied and reveal the substrate, another type of cavity can be formed directly seen on top of the two aforementioned. Here the cavity is filled with a single molecule so that both di-tert-butyl groups interlock with the open cavity. Some of the assembly pores are filled, too. Here the space of the pore prohibits a complete molecule to fit in, the observed adsorbates in the pores are attributed to molecular fragments like



(a) STM topography of several molecular islands grown next to a step edge. Areas with trihexagonal tiling as well as some domain boundaries are visible.



(b) Hexygonal unit cell with overlaid molecular models.



(c) Enlarged view on the molecules rotated di-tert-butyl-group and highest elements enclosed by brighter circles..

Figure 7.12. – *Trans-TBP adsorped on Ag(100) at room temperature. (a) shows a large overview of the assembled molecules. The unit cell constituents are enlarged in (b) where parts of (a) are shown with molecular models overlaid. (c) shows a single molecule crossing a horizontal plain to emphasize high lying part in the molecule that are marked with white circles and will appear brighter in STM. All images recorded with 437 mV, 0.1 nA, color scale 0 pm to 650 pm*

tert-butyl-groups that were incorporated by the assembly during the island growth.

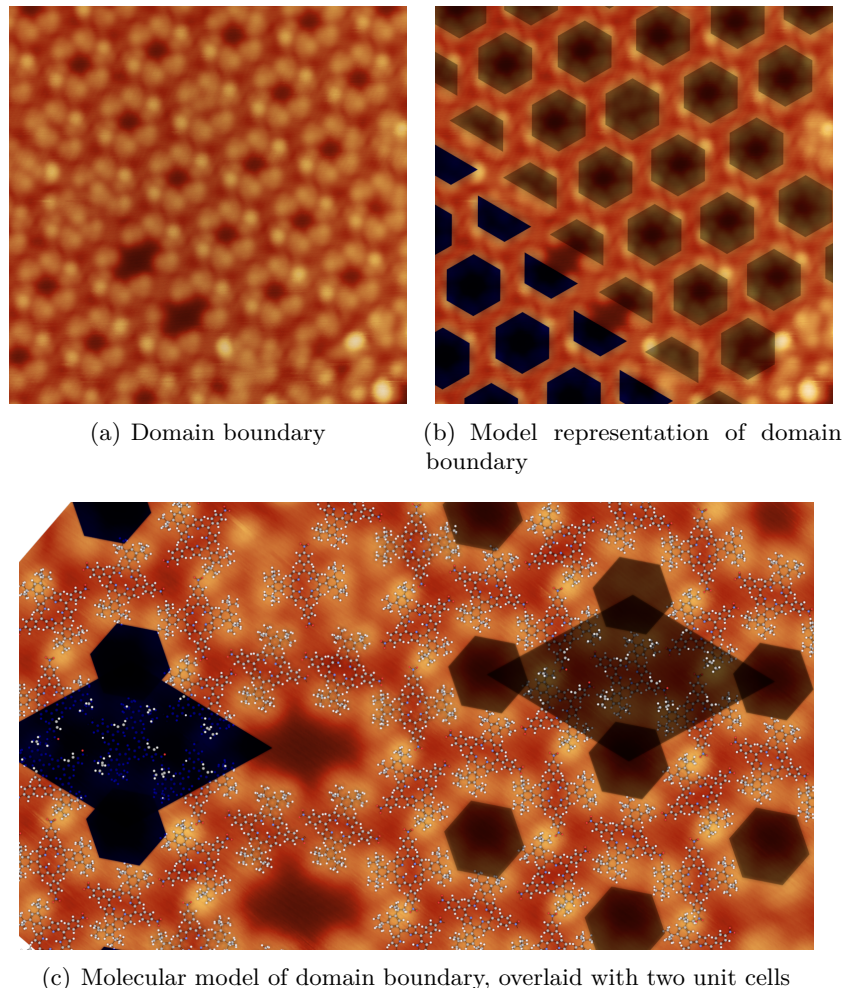


Figure 7.13. – Domain boundary of *trans*-TBP adsorbed on Ag(100) at RT. (a) shows an overview of the domain boundary together with its model representation in (b). The assembly close by is modeled in (c) where a rotated detail view of (a) is shown and molecular models overlaid. All images recorded with 1.3 V, 0.1 nA, color scale 0 pm to 650 pm

7.6. Summary & Discussion

TEXT

7.7. Conclusion

The driving force for orienting the whole molecule on the surface remains speculative. On Ag(100), neither an orientation of the molecules main axis with respect to the substrate, nor a orientation of butyl-groups along the dense packed substrate rows can be seen - which again favors Cu-substrate interactions as dominant role. When the copper is exchanged with silver to act as substrate, TBP behaves quite different. Although the distribution is homogeneous on the surface, the interaction between molecules look different. While on copper the most abundant binding motif is the head-to-head dimer, this motif does not appear on silver as often as on copper. Two other motifs emerge on silver. The interaction between the butyl-phenyl groups is considered to be van der Waals like [175], stabilizing the conglomerate.

8. Cyano functionalized helicene molecules on Ag(111), Ag(100) and *h*-BN supports

8.1. Abstract

We propose the novel synthetized 7,8-dicyano-5,6,9,10-dibenzo-[5]Helicene (dcdb-[5]H) as model compound to investigate intermolecular interactions present for chiral, dipolar species. The adsorption on different metal surface terminations (Ag(111)/Ag(100)) shows the importance of the cyano group. It determines the orientation of dcdb-[5]H strands along the substrate's high symmetry directions and dominates the intermolecular coupling of constructive enantiomers resulting in parallel dipole orientation. While on metal substrates strands are paired depending on the surface termination, broad islands are achieved by introducing a monolayer of *h*-BN grown on Cu(111) maintaining strands as building blocks but lifting their substrate interactions. On this geometrically flat surface, molecular orbital energies align to the modulated surface potential arising from the superstructure present in this lattice mismatched system. Here interactions between molecular and STM-tip dipole are observed.

8.2. Introduction

To gain insight in intermolecular interactions present on a sub-molecular level, model systems used are often reduced to two dimensions. This can be achieved by adsorption on a surface under UHV conditions that guarantee a clean chemical environment. vdW interactions can be investigated with high precision for molecules that consist of simple hydrocarbon species to help analyze larger, more complicated systems. While homogenously charged species govern their assembly by vdW interactions and avoidance of steric hinderance (pauli repulsion), polar molecules exhibit additional dipole interactions. The importance of these is evidenced for fluorenone derivatives [176–178], hydroxyanthraquinone[179], octanoic acid [180] and thiopene derivatives [181] on HOPG surfaces where the combined interplay between extended alkyl chains and dipole moment forms columns and two-dimensional packings. Repulsive and attractive forces determine the assembly of anthracenes with ether side chains and cause a patterned monolayer to form[182]. Depending on the substrate,

dipole moments have shown the ability to overcome electrostatic interaction energies to form gratings and 2D islands.[183]

Progress in coordination chemistry led to a variety of processes to heavily modify molecules or to completely design them on the drafting table by the needs of the task. It was shown that supramolecular structures of Hexa-peri-hexabenzocoronene with CN and NO₂ groups form hexagonal assemblies while functionalization with CF₃ groups opens a porous honeycomb structure under the influence of the larger dipole moment.[184]

Since the mid 50's of the last century helicenes faced increasing interest in their chiral and optical properties.[185–187] Helicenes consist of ortho-condensed, six membered carbon rings annulated at position 1 & 2 to form circular structures. Due to overcrowding in their center spirals are formed. Depending on the turn direction two enantiomers can be distinguished denoted as "R" [lat.: rectus, right] and "S" [lat.: sinister, left], often noted as P(lus) and M(inus). Like left and right turning screws, these are related to each other like mirror images that cannot be superimposed by rotation or translation. The lack of a rotary reflection axis is what makes these molecules chiral, an interesting geometric property present in many biological entities like sugars and proteins determining their biological function.

Because in simple helicenes carbon atoms are passivated with hydrogen, stereo selective molecular recognition mediated by van der Waals (vdW) forces plays an important role for 2D conglomerate crystallization.[188] (S)-proline, an amino acid, shows extended 2D island growth of enantiopure molecules, consisting of hydrogen bonded chains on a Cu(110) surface.[189] On the same surface the self-assembly of adenine is guided by hydrogen bonds to form linear and ladder like chains[190] and meta-aminobenzoate molecules assemble through hydrogen bonds between amino groups and carboxylate groups.[191]

The subtle interplay of hydrogen bonds, vdW- and dipole interactions can be accessed by designed chemical substituents that steer molecular assembly and function via their type, number and position in the molecule. Dibenzo-5[H] was used as model system to understand diastereomeric interactions in 2D crystals formed on an Au(111) surface where molecules deposited at room temperature (RT) form heterochiral 2D conglomerates.[192] (Molecular motion is frozen below 50 K where only homochiral molecular domains are observed.) Enantiopure 6,13-dicyano[7]H was used to study chiral recognition and chirality transfer on Cu(111)[193, 194], where the presence of the polar cyano group guides chain formation oriented 30° off the Cu(111) high-symmetry directions at lower coverages and forms 2D agglomerates at higher coverage. While close packing on single-crystal surfaces is always a combination of intermolecular forces and occupation of the favored ad-sites at saturation coverage, molecules may behave different when adsorbed on different surfaces. The interplay

of surface and helicenes' molecular structure is important for stereochemical recognition[195] and already investigated on (111) surfaces of silver and gold[196] and Ag(100)[197]. To understand enantiomorphism in 2D molecular crystals heptahelicene ([7]H) is used.[198, 199] On Cu(100) 2D conglomerate crystallization leads to homochiral domains[200] while racemic crystals[199] and separated homochiral domains[201] are reported on Cu(111) where substantial vdW repulsion was presumed. For enantiopure [7]H a transfer of molecular chirality into a long-range chirality of the assembled molecular assembly is observed on Cu(111)[202] and second layer adsorption leads to quasi-epitaxial growth with chirality transfer occurring in 3D.[203]

Not only acts the metal surface as a guide for 2D molecular motion, it is also an almost infinite charge supply/drain. With neglectable DOS close to the fermi energy, a single layer of hexagonal boron nitride (*h*-BN) acts as isolating spacer layer and reduces the influence of the substrate on the molecular assembly and frontier orbitals.[69, 113, 136] With a lattice mismatch of (2%)[65, 66] the geometrically flat[46] *h*-BN adlayer forms a electronically corrugated superstructure (moiré) on Cu(111).[65] Here the surface potential is nano-patterned[65], following the substrate's hexagonal symmetry, with the period determined by the angle between *h*-BN and Cu(111)[89]. The surface potential influences the energy of highest occupied (HOMO) and lowest unoccupied (LUMO) molecular orbital with respect to the vacuum level.[136, 204] STM is a versatile tool to investigate those systems since it detects geometric as well as electronic properties, and is even able to follow Ullmann coupling of bishelicenes on Cu(100)[205] on the surface.

8.3. The molecule

It is adsorbed @ RT on 1. a thin, insulating hexagonal boron nitride monolayer grown on a copper single crystal (*h*-BN/Cu(111)) as well as 2. different surface terminations of a metallic silver single crystal (Ag(111) & Ag(100)). The preparations are investigated with scanning tunneling microscopy & spectroscopy @ 5K (LT-STM/STS).

The carbon backbone of dcdb-5[H] either turns up clockwise (denoted as 'M') or counter-clockwise ('P') and is therefore chiral as shown in **Figure 8.1a,b**. The color of the carbon atoms in the helicene backbone emphasizes their height and allows for easier recognition of the turn direction also indicated by the circular arrows. The hexagons (green in **Figure 8.11a** for the M enantiomer and blue in **Figure 8.1b** for the P enantiomer) resemble the footprint of the molecule, while the direction of the dipole moment is indicated by an orange arrow within. To identify the adsorption geometry via LT-STM imaging, extended Hückel calculations are performed. A comparison between calculated (**Figure 8.1c**) and

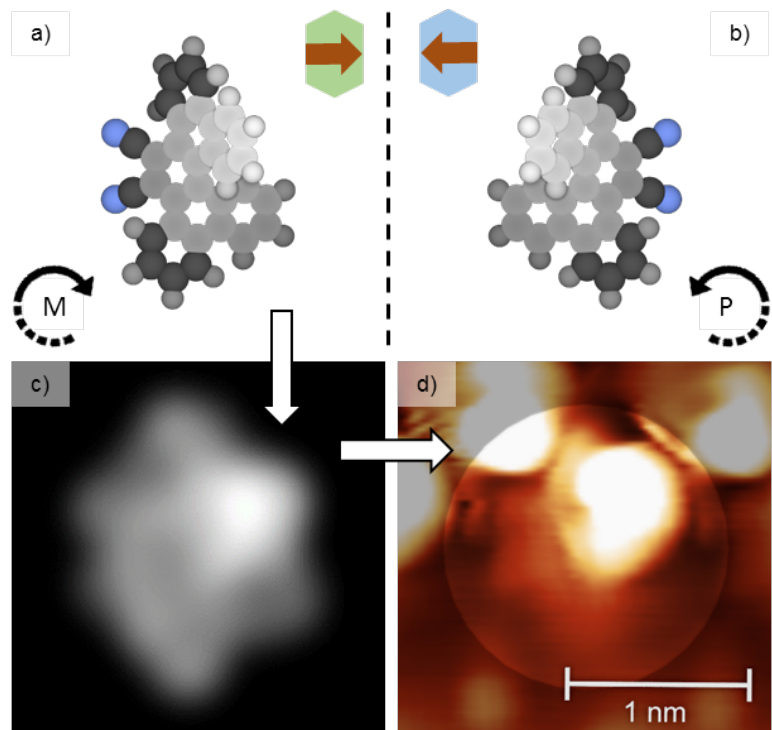


Figure 8.1. – Representations of dcdb[5]-H. Ortho-fused carbon rings build a helical structure which results in a chiral nature of this molecule. a, b) Ball models with indication of the chiral nature. The molecule either turns up clockwise (green hexagon, M) or counter clockwise (blue hexagon, P). A large dipole moment (orange arrow) is build up through the functionalization with two cyano groups at the central carbon ring. c) EHT simulated STM image of the M enantiomer. d) LT-STM image of an M enantiomer on Ag(111). All images show 2 nm × 2 nm, Image d is recorded at 150 mV, 0.09 nA.

measured (**Figure 8.1d**) STM image of the M enantiomer shows that one benzol-group at the lower part of the helicene backbone adsorbs flat on the Ag(111) surface while the opposing end of the helicene screw points away from the surface – a geometry reported for helicenes on other metal surfaces, too.[206] This distal part of the molecular helix is imaged as protrusion in STM and is the dominant distribution to the STM contrast in all images. The benzol groups are recognized as darker regions with uniform contrast to the sides while the cyano group contributes barely to most of the observed contrasts in STM. A match between calculated and measured STM image can only be obtained in the shown configuration (**Figure 8.1a-c**) allowing for assignment of chirality and azimuthal orientation on the surface.

8.4. Results & discussion

8.4.1. on Ag(111)

To clarify the molecular interaction geometries within the assembly, dcdb-[5]H is adsorbed on Ag(111) (**Figure 8.2a,c**). It assembles in 1D-chains oriented along the high symmetry directions of the three-fold symmetric substrate. A typical chain contains between 30 to 50molecules (compare appendix ??). Each chain is made up two single strands. The model representation (**Figure 8.2d**) partially shows two strands of a chain separated by a black line. A strand consists of molecules with alternating chirality but parallel aligned dipole moment. Two strands rotated by 180° with respect to each other form the chain shown in **Figure 8.2c**. The inter-molecular distance (center-center) of neighboring molecules with different chirality is $A_{Ag(111)} = 0.81(6)$ nm, two molecules with the same chirality are separated by $B_{Ag(111)} = 1.21(6)$ nm. Single strands are $C_{Ag(111)} = 2.09(6)$ nm apart. The close arrangement of the molecules in a strand is possible because the cyano groups of the molecule have a lower height than the elevated carbon ring of its closest chiral counterpart. Although – if like here the geometry is projected orthographically onto the surface – the molecules seem to touch this is not the case. The same is true for two elevated carbon “tails”. Their elevation leads to carbon rings with a well-defined distance. Only the projection on the image plane makes them look closer than they are in real space. If a chain happens to have a kink both parts of the chain follow the high symmetry directions of Ag(111). The connection point of two chains is made such that frontier molecules of different chains connect with their cyano groups always pointing towards the helicene backbone of the connecting chain. Most chains terminate with the same length of their constituting strands pointing to a mechanism where the total dipole moment of the chains is minimized. The fact that chains on Ag(111) almost exclusively occur in

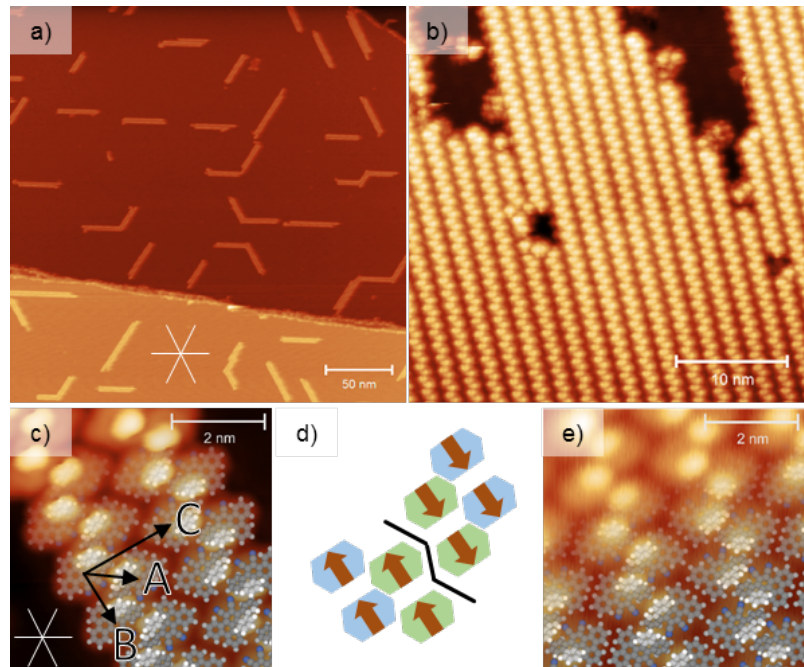


Figure 8.2. – *Dcdb-[5]H* on Ag(111) (a) and on h-BN/Cu(111) (b). Detail images of a chain and parts of the extended island are shown in c) and e) respectively. Labelled arrows in c) indicate the direction in which center-center distances have been measured. A model representation of the binding motif is given in d). It shows a simplified representation of the models overlaid in c) and e). High symmetry directions for Ag(111) are depicted as white lines. The binding motif is the same in both cases though extended islands only form on h-BN. Imaging parameters: a) 295 nm × 295 nm, 655 mV, 0.02 nA b) 35 nm × 35 nm, 2.37 V, 0.13 nA c) 5.5 nm × 5.5 nm, -500 mV, 0.1 nA e) 5.5 nm × 5.5 nm, 1 V, 0.07 nA

pairs of strands (even number of molecules in chain width (**Figure E.3**)) underpins this assumption and leads to a minimum of total surface dipole. Molecules are stable upon annealing to 100 °C. LT-STM images for an annealing sequence from 100 °C to 175 °C can be found in the appendix (**Figure E.1**) depicting the gradual decrease in chain length and over all order. The longer the annealing time, the more pronounced this effect gets. When exceeding an annealing temperature of 100 °C a surface assisted, temperature induced cyclodehydrogenation is observed (**Figure E.2** in appendix) for a fraction of molecules that increases with temperature and time. Here the first and last ring of the helicene backbone fuse together, forming a flat molecule with no chiral properties. This new compound tends to form separate chains often attached to existing ones.

8.4.2. on *h*-BN on Cu(111)

To further investigate the intermolecular interactions dcdb-[5]H is adsorbed on *h*-BN/Cu(111). Here extended islands (**Figure 8.2b,e**) are formed. The building block of this 2D assembly is the same as after adsorption on Ag(111) (i.e. strands) which can still be recognized at the edges of the assembly. Several strands form an island, where again every second strand is rotated by 180°. Different islands on the same *h*-BN flake do not show a fixed orientation to the underlying substrate (not shown here). Distances are $A_{h-BN} = 0.77(6)$ nm, $B_{h-BN} = 1.20(6)$ nm and $C_{h-BN} = 2.05(6)$ nm - close to those on Ag(111). On *h*-BN the molecules assemble the same way as on a metallic support. This suggests that the molecule-substrate interaction is weaker than the inter-molecular interaction including 1: hydrogen-bridge bonding of CN- groups towards the terminal H of the next molecule (along A & B), 2: π -stacking of molecular orbitals of elevated carbon rings (along A), 3: vdW interactions of flat helicene parts (between chains, along C) and 4: dipole interaction along direction B (parallel within strands) & C (antiparallel for neighboring strands). Strict orientation of the molecular assembly along the crystal axis on metal supports indicate an interaction between the molecule (functional –CN group) and the substrate. This restriction is lifted when changing to the insulating *h*-BN support leading to coincidentally oriented molecular islands.

8.4.3. on Ag(100)

We prepared dcdb-[5]H on Ag(100) to further investigate the influence of the substrate termination on the molecular self-assembly. Ag(100) has two different sets of symmetry directions in a square unit cell. Directions [0 1 1] & [0 -1 1] point from one surface atom to its nearest neighbor (white lines in **Figure 8.3**). [0 0 1] & [0 1 0] are rotated by 45° with respect to [0 1 1] & [0 -1 1] and point from one surface atom to its second nearest

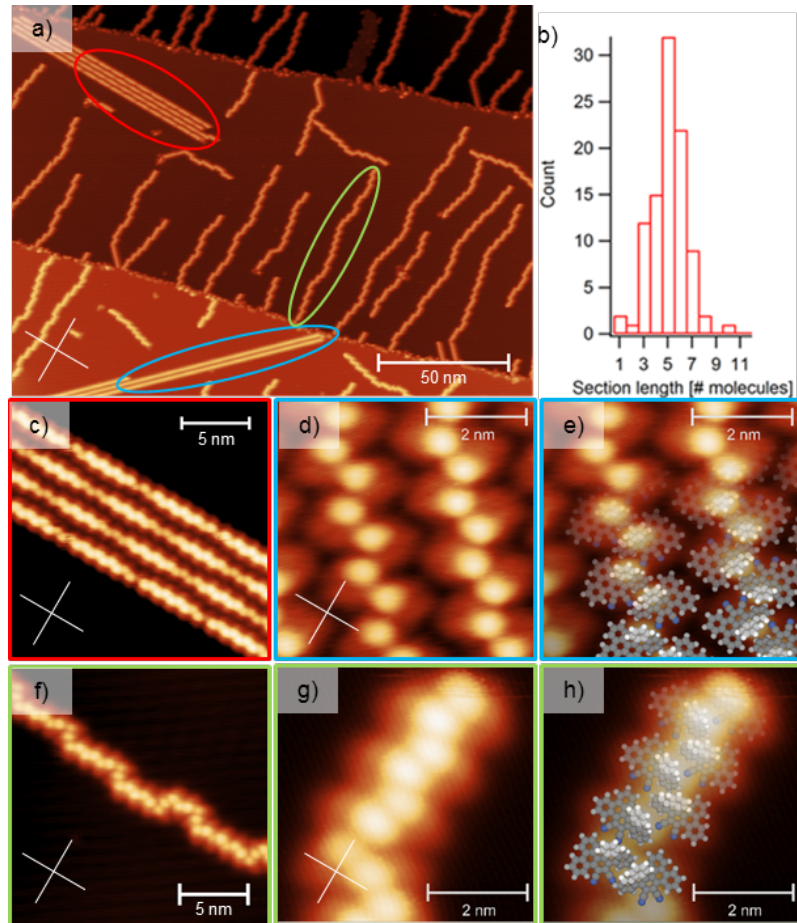


Figure 8.3. – Self-assembled structures upon RT adsorption on Ag(100). White lines show the high symmetry directions of the substrate. A statistical analysis of the section length of kinked strands is shown in b). Overview (f) and detail images (g, h) show the binding motif within kinked strands. Broad chains are observed less often. Those aligned along [0 1 1] & [0 -1 1] (c) show periodic height modulation. Chains oriented along [0 0 1] & [0 1 0] (d, e) do not show periodic height modulation. Imaging parameter: a) 200 nm × 150 nm, 500 mV, 0.0 nA c) 18 nm × 18 nm, 450 mV, 0.2 nA e) 5 nm × 5 nm, 31 mV, 0.5 nA f) 18 nm × 18 nm, 272 mV, 0.06 nA g,h) 5 nm × 5 nm, 325 mV, 0.1 nA

neighbor. **Figure 8.3a** is an overview STM image showing different chain orientations (i-iii) where three of them are marked with colored ellipses. Enlarged views (c,d,f,g) and overlaid atomic models (e,h) are given with the corresponding color frame. Like on Ag(111) molecules assemble in chains oriented along the high symmetry directions. Type i) chains aligned along [0 1 1] & [0 -1 1] (red) show modulation of their apparent height visible in STM (**Figure 8.3c**). The period of this modulation is 6.03(11) nm. For these, differential conductance (dI/dV) maps are recorded at voltages ranging from 0.3 V to 0.6 V (see appendix ??) showing the lateral distribution of the corresponding molecular states. These show a similar period of 6.1(3) nm. Both indicate a commensurate growth (every 12th dcdb-5[H] molecule occupying the same lattice site every 21st silver surface atom - corresponding to a period of 6.048 nm. This is in line with the molecule-substrate interaction visible in the strict alignment of molecular and crystal axis. It is likely that the two -CN groups of the molecule determine the commensurate adsorption position and the registry to the substrates' high symmetry directions.

The reduced surface symmetry results in additional assemblies (ii-iii) not observed on Ag(111) or *h*-BN/Cu(111). ii) Some chains are oriented along [0 0 1] & [0 1 0] (blue ellipse in **Figure 8.3d,e**). The distances in this molecular assembly are $A_{Ag(100)}^b = 0.67(6)$ nm, $B_{Ag(100)}^b = 1.25(6)$ nm and $C_{Ag(100)}^b = 2.10(6)$ nm. These do not show modulation in apparent height. iii) The majority of the chains is formed by a single strand, which is oriented along [0 1 1] & [0 -1 1] and periodically kinked. The cyano group always points towards a rising step edge if connected to one. If a strand kinks to the left or right is defined relative to the direction of its dipole moment. The kinked nature results in 1: a connecting segment between two sections, 2: a turn direction for each kink and 3: a typical length of a section. **Figure 8.3g,h** show a section of a kinked chain that is 6 molecules long, together with its connecting segment after the strand kinks to the left. The connecting segment consists of two molecules, rotated by 45° to the connecting sections. The length distribution (**Figure 8.3b**) indicates a most common section length between 4 and 6 molecules. Kinks to the left occur as often as to the right. The distance of two neighboring molecules (opposing chirality) is $A_{Ag(100)}^t = 0.83(6)$ nm, while two adjacent molecules with the same chirality are $B_{Ag(100)}^t = 1.17(6)$ nm apart. Entirely straight strands are less frequent. These are oriented along [0 0 1] & [0 1 0] (not shown in detail here, but some can be found in the overview topography in **Figure 8.3a**). Due to their straight nature, they do not have connecting segments. They are typically shorter than the total length of the kinked chains but longer than their sections. When comparing $B_{h-BN} = 1.20(6)$ nm to $B_{Ag(111)} = 1.21(6)$ nm, $B_{Ag(100)}^k = 1.17(6)$ nm and $B_{Ag(100)}^b = 1.25(6)$ nm no change in B can be observed. This points to larger molecule-molecule interaction

compared to molecule-substrate interactions. Considering the proposed adsorption model, estimations of binding distances can be given. The distance between the -CN group and the terminal H atom is 0.226 nm. This distance varies with the elevation adsorption angle but match reported distances.[134, 207, 208] Two molecules with different chirality are connected through π -stacking of their elevated carbon rings. The distance between those is 0.46 nm and assumes a parallel adsorption of the lower helicene helix, which is a reasonable guess but hard to verify in STM.

8.4.4. Molecular orbital energy shift and tip-dipole

As the assembly is understood on the two silver substrates as well as on *h*-BN, we take a closer look on the effects that are only visible on *h*-BN. Varying the bias voltage (U_b) in constant current mode results in a periodic contrast pattern across the RT assembly of dcdb-[5]H on *h*-BN (Figure 8.4). While at high U_b the STM contrast resembles every strand with the same apparent height (a), lowering U_b changes the apparent height of every second chain (b-c). Because these show the same dipole orientation of its constituents and therefore the same alternating pattern as the STM contrast, an interaction of a polar tip termination with the molecular dipole is likely. A tip termination with unfavorable tip-molecule interaction for one tip-dipole orientation will avoid regions with repulsive interaction. The accompanied increase in the tunneling distance results in chains being imaged in a darker contrast. The contrast is enhanced for the 180° rotated chains because here the interaction becomes attractive. An alternation of both effects results in the contrast pattern shown in Figure 8.4c. According to this, the modeled tip-dipole is assumed to be flexible (red arrow mounted on a spring in Figure 8.4d) and allowed to rotate in plane (semitransparent arrows) as it would result from the pickup of a molecule that is allowed to rotate around its helix axis. When $|U_b|$ is increased the increasing tip-sample distance quickly reduces the dipole-dipole interaction (d^{-3}) and therefore a homogeneously distributed contrast across the chains as observed in Figure 8.4a. Please note that not only dipole-dipole interactions are present in the close proximity of functionalized tip and molecular assembly. With a molecule attached to the tip interactions of the molecular helices are possible. The elevation of the distal parts in the helix of two neighboring chains is antiparallel and interaction with the tip may result in a similar contrast. Modification of the tip apex with [7]H is possible as reported in literature[195] and used for dimer-separation on a Cu(111) surface.

An electronic influence of the substrate on the occupied states of the molecule can be excluded as a reason for the contrast variation since the resulting pattern would show hexagonal symmetry as discussed in the following.

The inherent lattice mismatch between *h*-BN and copper substrate results in an emerging moiré superstructure[65], dividing the surface in regions with smaller (wire) and larger surface potential (pore)[209]. In **Figure 8.5a-c** pores are highlighted by dashed circles. Here molecular energy levels are shifted by the changing surface potential.[136] **Figure 8.5a** shows a STM topography where this electronic shift is visible as change in apparent height of the molecules. This can be explained by taking a closer look at energies close to the highest occupied molecular orbitals (HOMO) and lowest unoccupied molecular orbital (LUMO) states as shown in **Figure 8.5b** and **c** respectively. When tuning U_b from 0 V to -3 V HOMO states appear first on the wire sites (**Figure 8.5b**) because on pore regions the HOMO is shifted further away from the fermi energy compared to the molecules on wire regions where occupied states are accessible first. When tuning U_b from 0 V to 3 V LUMO states are antithetically observed first on the pore sites (**Figure 8.5c**) where the larger surface potential shifts the unoccupied states closer to fermi.

Position depended differential STS (dI/dV) on molecules in the moiré unit cell shows this shift of HOMO and LUMO. On a pore site (P in **Figure 8.5d**) both states are shifted towards negative bias (to the left). This results in the HOMO (LUMO) being shifted further away (closer towards) the fermi level. The voltages at which STM was conducted in **Figure 8.5b & c** are shown as black vertical lines limiting the electronic states contributing to the tunneling process to either include molecules on wire (**Figure 8.5b**) or pore (**Figure 8.5c**) regions. This is in agreement with the position depended emergence of the frontier orbitals in STM as discussed earlier. No hybridization with the metal substrate is observed, resulting in a large featureless electronic band gap of (4.4(1) eV) and highlighting the effective electronic decoupling of the molecules by the *h*-BN layer.

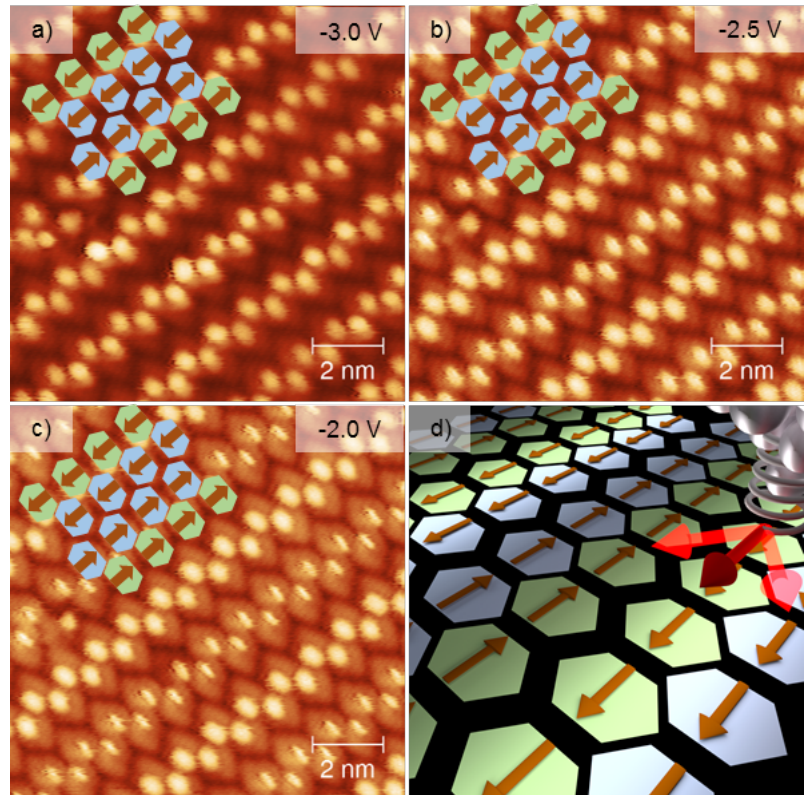


Figure 8.4. – Periodic change in contrast when $R_t = U_b/I$ changes. Cc-STM images (a-c) are acquired at a current set point of 0.05 nA but decreasing U_b (given in upper right corner). Model representation (d) of possible dipole alignment between tip (red arrows) and molecular assembly (orange arrows). Dipole interaction strength changes with respect to their relative alignment which is responsible for the alternating contrast in cc-STM. The contrast difference quickly diminishes with increasing U_b because electric dipole field scales with d^{-3} .

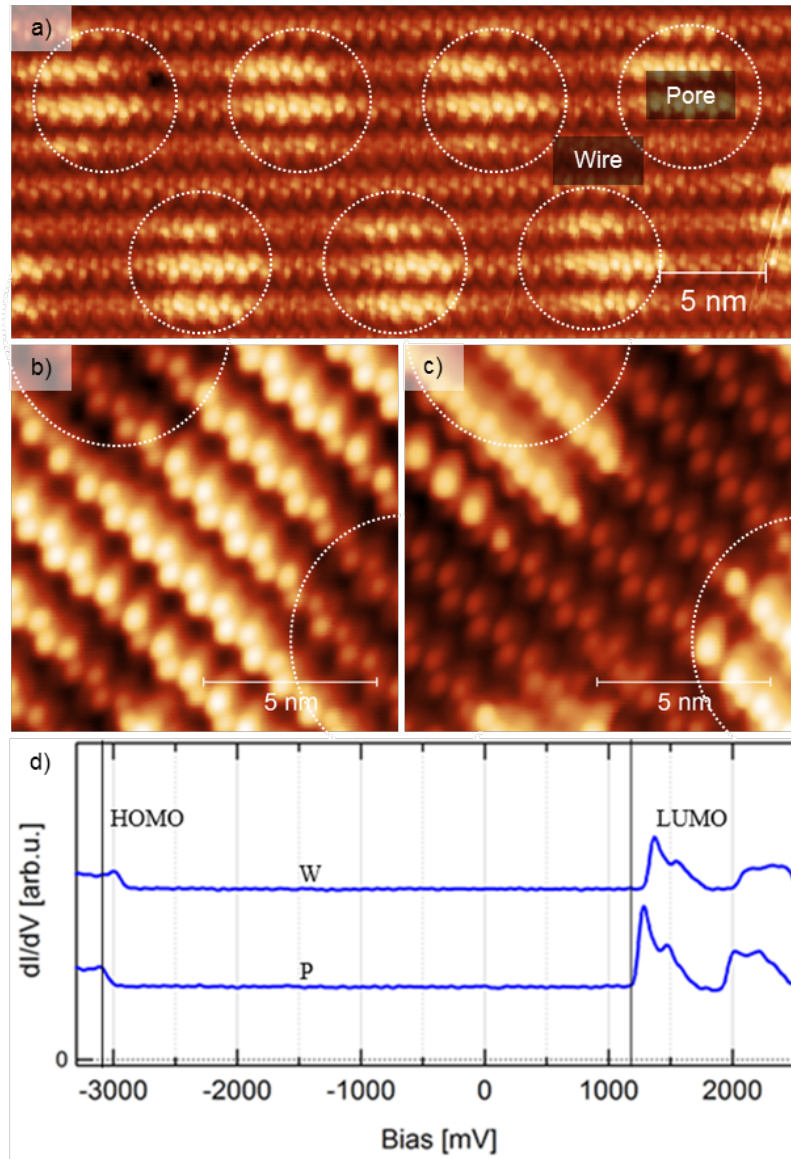


Figure 8.5. – STM topography with visible moiré protrusions (white dashed circles) recorded at 1 V, 0.05 nA (a). STM topographies of HOMO (b, $U_b = -3.1$ V) and LUMO (c, $U_b = 1.2$ V) states recorded at 0.1 nA. U_b used for imaging is also indicated by black lines in the STS spectra (d) where HOMO/LUMO states and electronic gap are shown. Spectra labeled W(P) are recorded on a wire(pore) region of the moiré.

8.5. Conclusions

We contribute measurements on novel synthesized chiral molecules where chiral separation is overcome by intermolecular interactions. This is achieved by molecular design where a cyano group is added to the central ring of the helicene. On all substrates racemic assemblies are formed guided by the presence of the cyano group. Especially on Ag(111) dipole interactions of single strands favor the formation of paired strands along the high symmetry directions. Their assembly is stable upon annealing to 100°C and disintegrates quickly at higher temperatures. Here single molecules undergo a surface assisted cyclodehydrogenation using the silver surface as catalyst resulting in a new achiral compound. On Ag(100) more chain directions and setups can be reported, but only one where commensurate growth is observed. Furthermore it is shown that *h*-BN is an adequate spacer layer to decouple dcdb-[5]H from the metallic support. Removing the metal substrate that facilitates growth along high symmetry directions results in extended island growth with no particular substrate registry. The isolating properties of *h*-BN is indicated by unperturbed HOMO/LUMO states with a flat electronic gap measured in STS. *h*-BN also templates the substrate's surface potential directly transferring to HOMO/LUMO states, thus shifting them towards negative bias on pores and positive bias on wire regions.

A. Polycrystalline copper foils

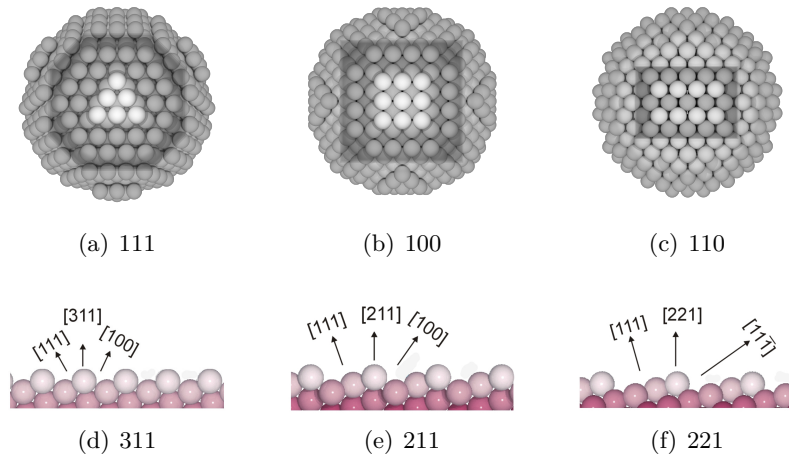


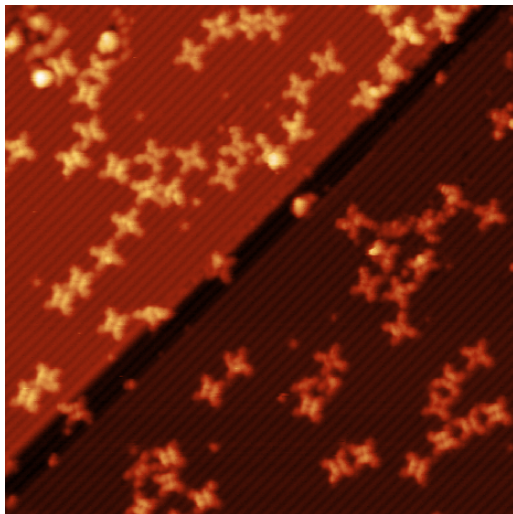
Figure A.1. – Hard sphere models of different surface facets for a fcc crystal. (a)-(c) Same fcc crystalline cluster, viewed along the different surface normal of surface orientations (111), (110) & (100). Terraces are parallel to the paper plane. (d)-(e) Higher order facets are shown from the side as they may be present on an unordered polycrystalline surface. (311), (211) & (221) consist of (111) terraces separated by steps that form a regular stepped surface. **311:** (100) steps run parallel to $[0\bar{1}\bar{1}]$, rhombic unit cell. Terrace is 4.23 Å (two close-packed rows) wide and inclined by 33.5°, steps by 146.4° with respect to the surface normal. **211:** (100) steps run parallel to $[01\bar{1}]$ crystal direction. Rectangular unit cell. Terraces are four close-packed row wide (7.66 Å) and inclined by 19.5°, steps by 35.3° with respect to the 221 surface normal. 0.74 Å interlayer spacing. **221:** (111) steps parallel to $[\bar{1}10]$. Steps go up in $[\bar{1}\bar{1}4]$, rectangular unit cell. Terraces are 7.66 Å wide, inclined by 15.8°, steps by 54.7° with respect to the [221] surface normal. 0.6 Å interlayer spacing. Lower graphics row adapted from [210].

A.1. Surface structure of h-BN on Cu-foil

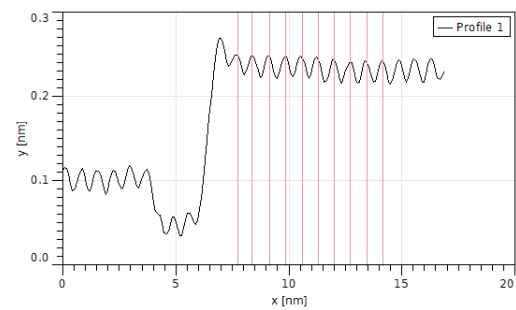
During experiments a “new” surface structure appeared and is shown in **Figure A.2**. The apparent height change between the both terraces is 130 pm separated by a slim trench that is slightly lower than the right terrace (50 pm). The parallel stripes have an apparent corrugation of 25 pm and are separated 70 pm from each other and cover the whole image.

The adsorbed TPCN molecules show different apparent heights in their molecular center. Some fragmented and heavily deformed molecules are visible.

A. Polycrystalline copper foils



(a) Molecules on copper foil surface - supposed to be covered with *h*-BN, maybe just free (maybe faceted) copper. Stripes not visible on the lower terrace, although present in the same orientation.



(b) Line spectrum across the step shown in (a) perpendicular to the trench. No molecules were crossed.

Figure A.2. – Surface structure of copper foil after deposition of TPCN molecules. Two terraces are visible, both covered with linear stripes - oxygen over layer (2×1)? - cu reconstruction? - maybe some very small (0.75 nm) linear moire on a Cu(100) facet? Noise can be excluded due to the fact that the stripes appear in both scan directions on the same spot. Adsorbed TPCN molecules appear as cross shaped protrusions. Many deformed molecular cores visible throughout the image → strong substrate interaction → no h-BN! Line spectrum shown in (b) indicating a period of 70 pm. Imaging parameters: (a) 1.26 V, 0.04 nA, color scale 0 nm to 0.8 nm, Image width: 40 nm

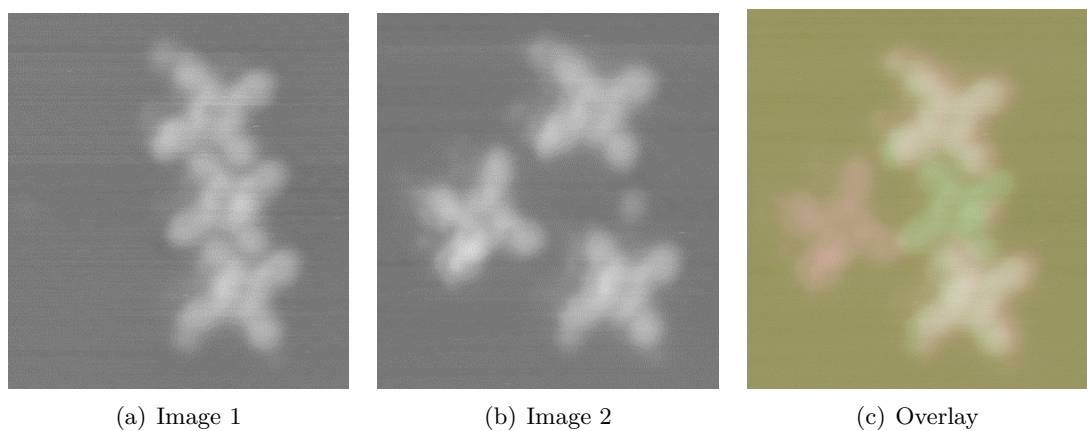


Figure A.3. – **Parameters** Position change of TPCN group members. Central molecule is manipulated, color indicates its initial (a, green hue in c) and final (b, red hue in c) position. Image (c) is created via an overlay of two sequential images. The upper and lower molecules do not shift thus sharing the same color.

B. Pyrene

Figure B.3 shows the emergence of LUMO states for trans-pyrene. The STM topographies show the same region with subsequently increased bias voltage. Starting close to the fermi level in the molecules' band gap the contrast is determined by the shape of the molecule (upper left). Increasing the bias voltage (for upper left to lower right) reveals two things. First the contrast pattern changes at energies close to the proposed LUMO 1.4 V to 1.6 V and LUMO + 1 2.2 V to 2.4 V energies, while the contrast between 1.8 V and 2.1 V remains constant. Second this change in contrast is not homogeneous across the surface but originates from the pores' center.

Some preparations were done to show the functionality of the trans-pyrene pores as host system for other molecules. First cis-pyrene was dosed on the surface at R, afterwards annealed to 100 °C, cooled to RT followed by dosing trans-pyrene molecules. Two different, coexisting motifs occur which are shown in **??**. First there is a dense packed phase (**Figure B.7(a)**, **Figure B.7(c)**). This mixed preparation does show a uniform growth. Alternating rows of either trans-pyrene or pairs of cis-pyrene molecules assemble in islands. The resulting triclinic unit cell (1.94 nm × 1.97 nm 75°) incorporates 3 molecules – one trans-pyrene and two cis-pyrenes. The second phase is dominated by the kagome motif already observed in the homo-molecular preparations but with their larger pores partially filled with cis-pyrene species (**Figure B.7(b)**, **Figure B.7(d)**). The unit cell remains the very same, but contains an additional cis-pyrene molecule. Not all guests (cis-pyrene) molecules are oriented the same way, only discrete orientations are allowed (and three of six different ones can already be seen in **Figure B.7(b)**). This means that although cis-pyrene molecules were evaporated first their assembly becomes unstable at temperatures of about 100 °C. This allows them to participate in the nucleation process after the trans-pyrene molecules are dosed at RT. Their assembly is still in progress while cooling down from RT to 7 K. A fully occupied kagome cell bears 3 trans-pyrene molecules and a single cis-pyrene molecule.

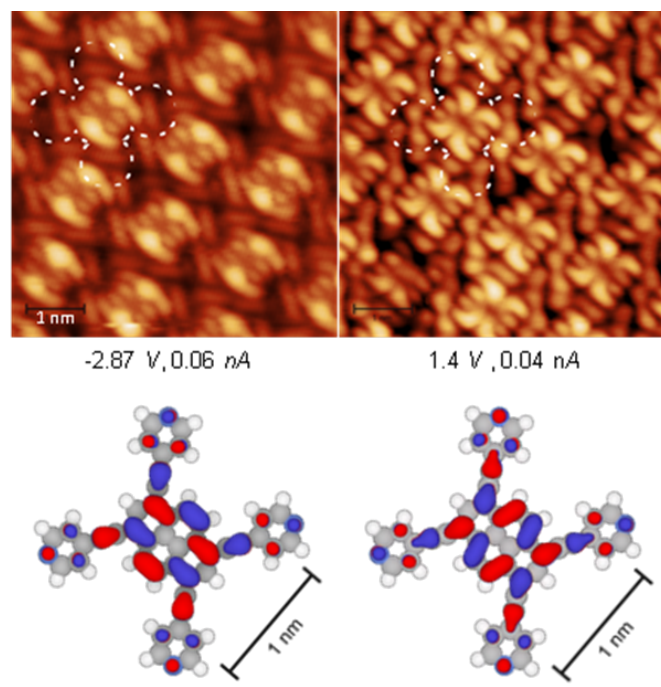


Figure B.1. – Calculated (EHT) HOMO (left) and LUMO (right) states of trans-pyrene. Assignment of HOMO and LUMO orbitals through symmetry observations in STM topography images that resolve the molecular orbitals. Compared to the HOMO, where between two legs only one side features a double lobe, the LUMO has double lobes in between every leg.

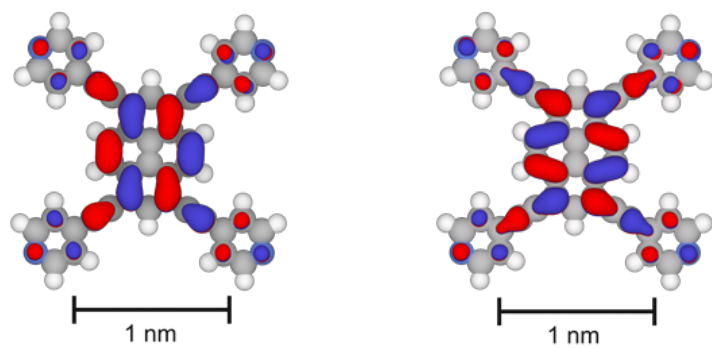


Figure B.2. – a) EHT calculated HOMO and b) LUMO states of cis-pyrene.

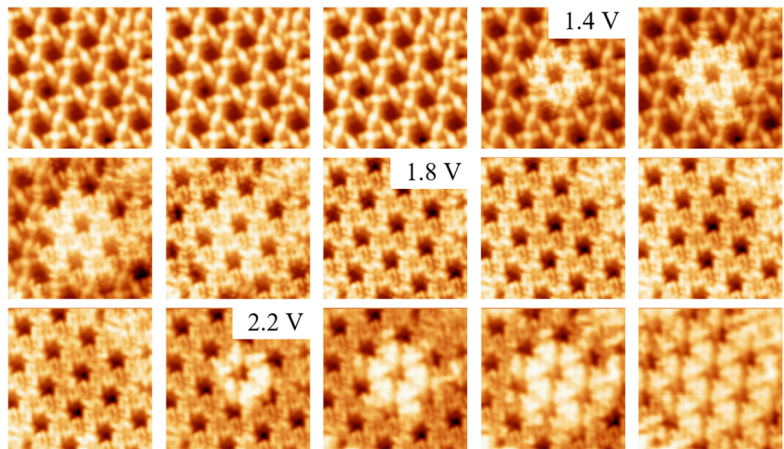


Figure B.3. – STM image series depicting LUMO/LUMO+1 states with positive bias voltages (1.1 V to 2.5 V). Starts @ 1.1 V and increases in steps of 0.1 V for upper left to lower right, Image size is 11 nm × 11 nm.

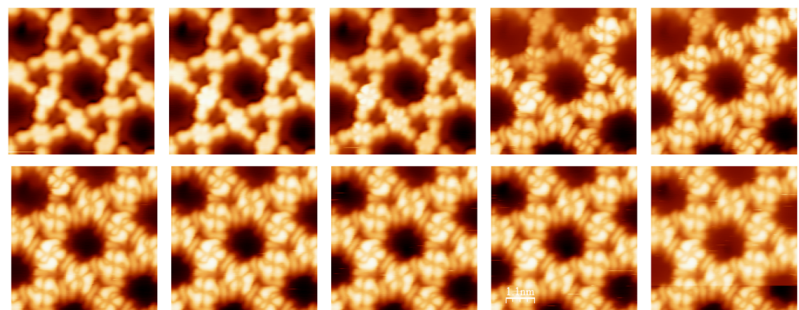


Figure B.4. – STM image series depicting HOMO-1 states with negative bias voltages -1.8 V to -2.7 V. Starts @ -1.8 V and decreases in steps of 0.1 V for upper left to lower right. Image size is 5.5 nm × 5.5 nm.

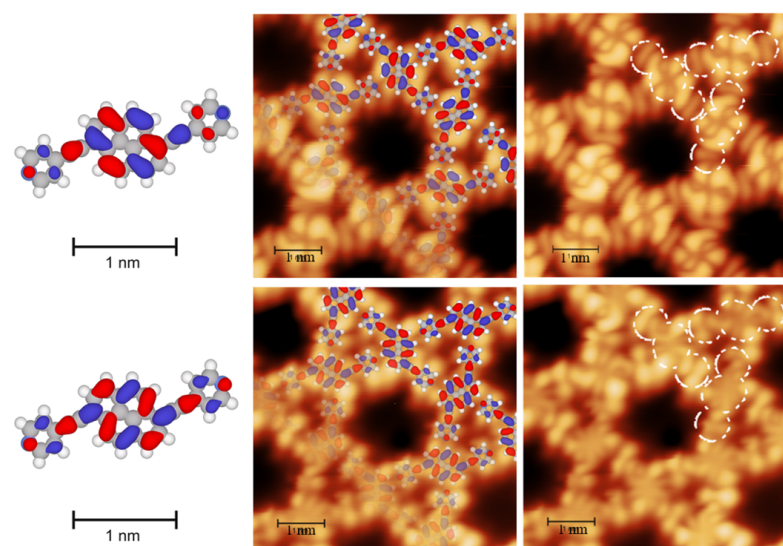


Figure B.5. – Calculated (EHT) HOMO (top) and LUMO (bottom) states (in red/blue) superimposed on a model of trans-pyrene. Imaging parameter: -2.4 V (HOMO) & 2.1 V (LUMO). Recorded with 0.2 nA , Image width: 5.5 nm .

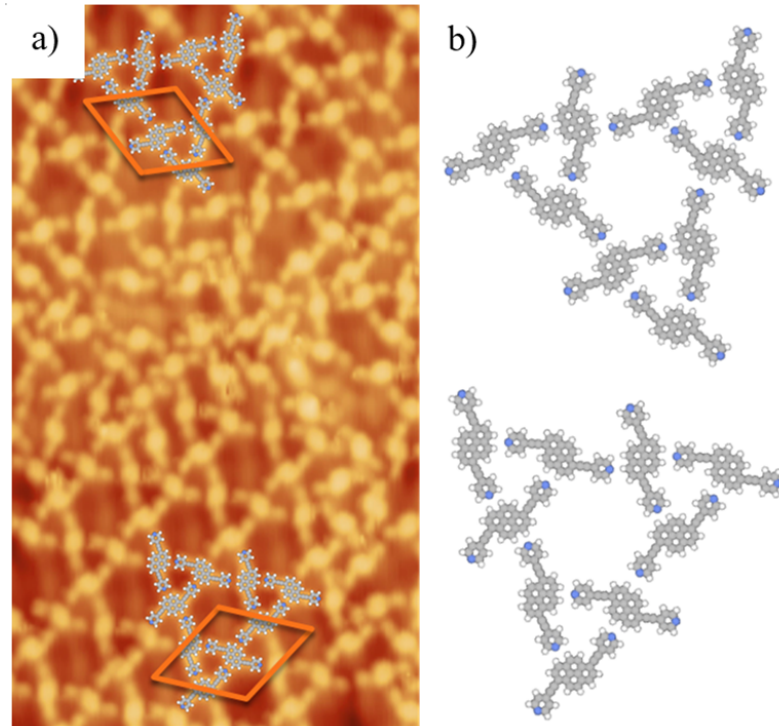


Figure B.6. – Homochiral mirror domains of a self-assembled sub-ML of trans-pyrene on $h\text{-BN}/\text{Cu}(111)$. a) STM image with overlaid molecular models and unit cells (colored in orange). b) Enlarged view on the molecular assembly in a). Imaging parameters: 14 nm × 25 nm, 1.0 V, 0.1 nA.

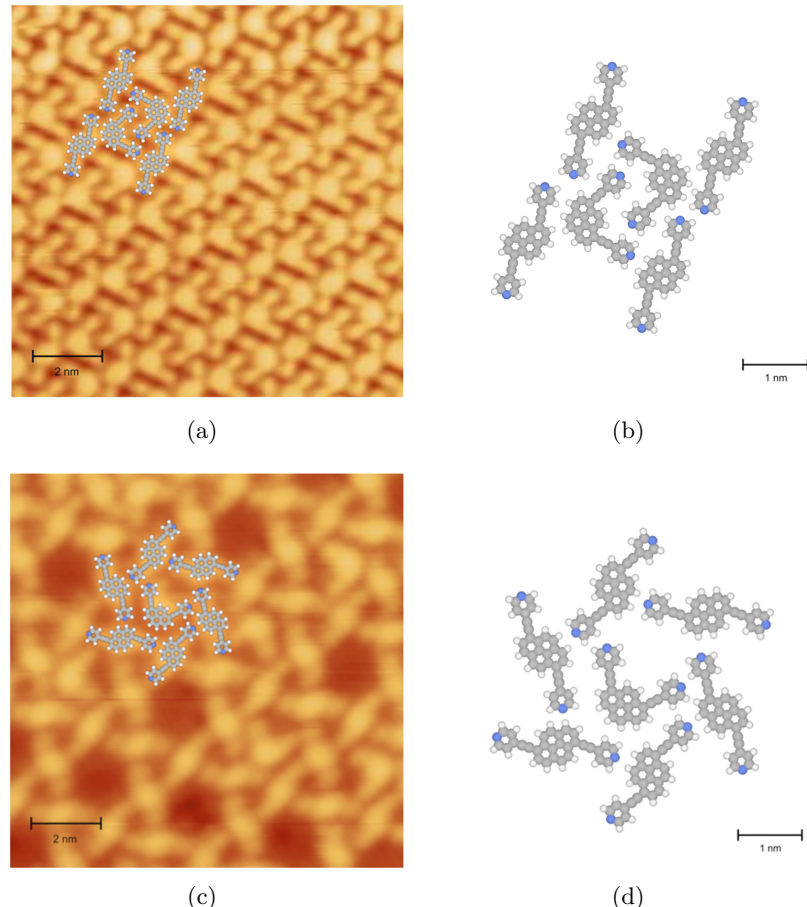


Figure B.7. – *Cis*-pyrene/*trans*-pyrene mixed preparation on *h*-BN/Cu (111). STM image of a self-assembled sub-ML with overlaid molecular models ((a), (c)). Enlarged views on the molecular unit cells ((b), (d)). (a), (b)) shows a dense packed mixed motif while (c) and (d) show *cis*-pyrene molecules (guest) in a *trans*-pyrene kagome (host) network. Imaging parameters: 1.0 V, 0.06 nA.

B.1. Extended Hückel theory calculations

In the following extended Hückel theory calculations of functionalized pyrene molecules are shown. After structural relaxation via the AM1 semi-empirical method in the Hyperchem software, the result is exported to an IGOR script for presentation. Single molecular orbitals as well as their sum can be shown. For all molecules some basic information is given in a box. The number of atoms, electrons and calculated orbitals is given together with a ball and stick model of the corresponding molecule. Calculated HOMO/LUMO states are shown to the right with their energies noted below. The left side of the pages shows occupied states (second column) and their sum (first column). The right side shows the unoccupied in the same manner.

The first two pages will show cis-pyrene as calculated in gas phase together with a model showing the rotation of pyridil legs and the influence on molecular orbitals. Trans- & tetra-pyrene molecules are shown afterwards.

Due to the same molecular center, all the species show distinct symmetry towards their pyrene center.

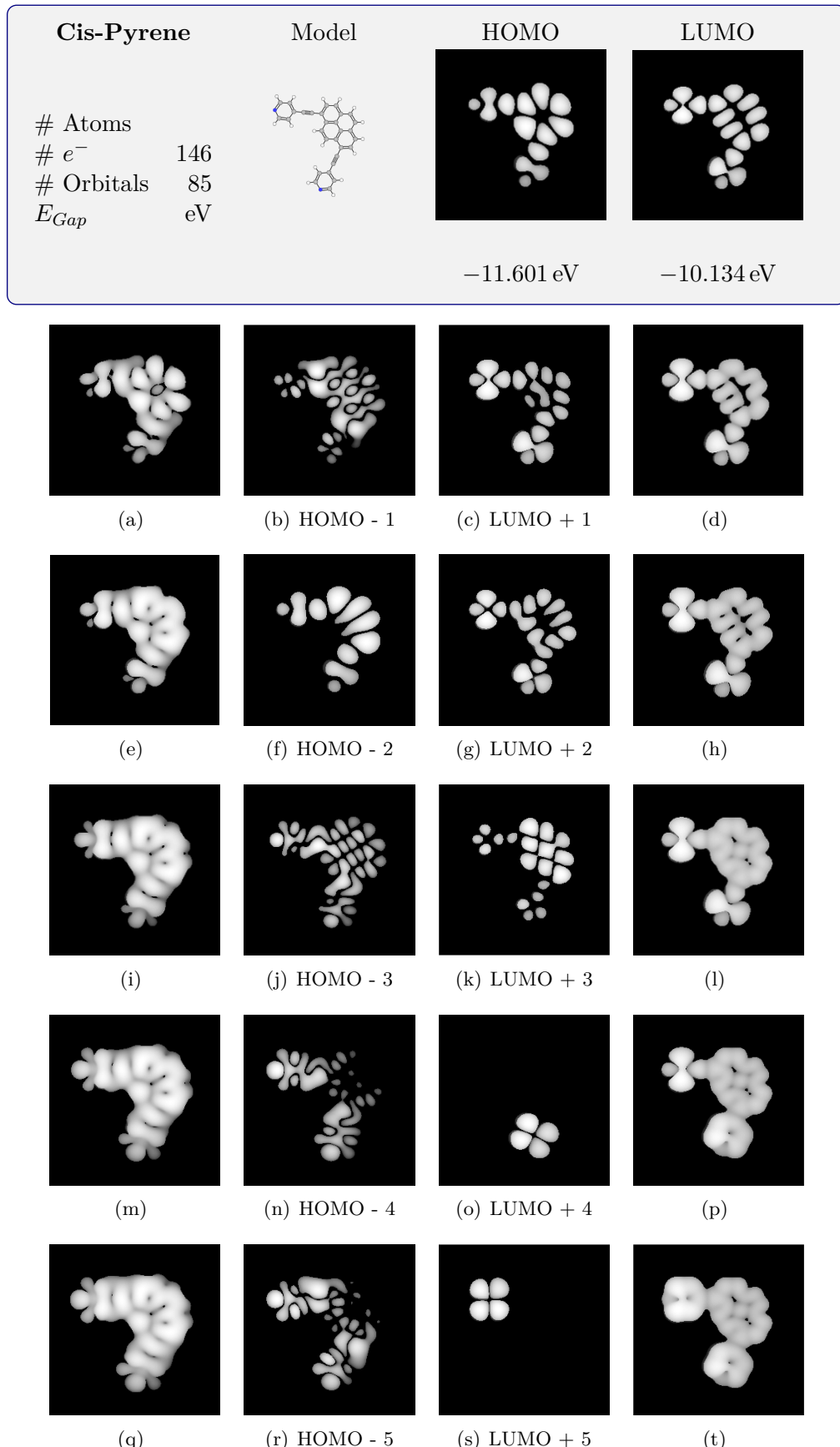


Figure B.8. – EHT calculated molecular orbitals. HOMO and LUMO states together with five neighboring states (shown in the same column). Inner two columns show HOMO & LUMO states. Outer columns show integration of states as STM image estimation if all states to E_F were contributing equally. Images are 2.5 nm wide

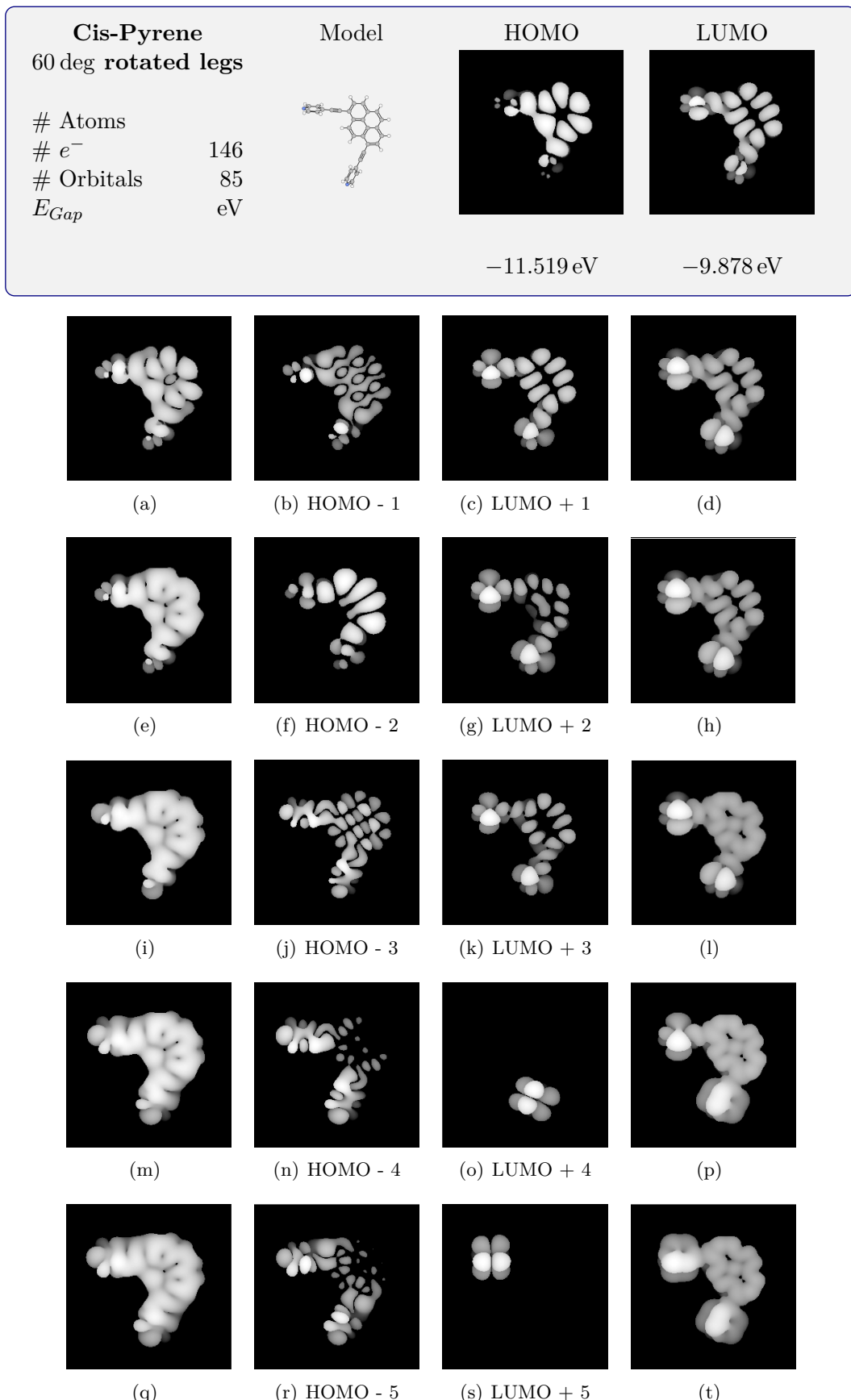


Figure B.9. – EHT calculated molecular orbitals. HOMO and LUMO states together with five neighboring states (shown in the same column). Inner two columns show HOMO & LUMO states. Outer columns show integration of states as STM image estimation if all states to E_F were contributing equally. Images are 2.5 nm wide

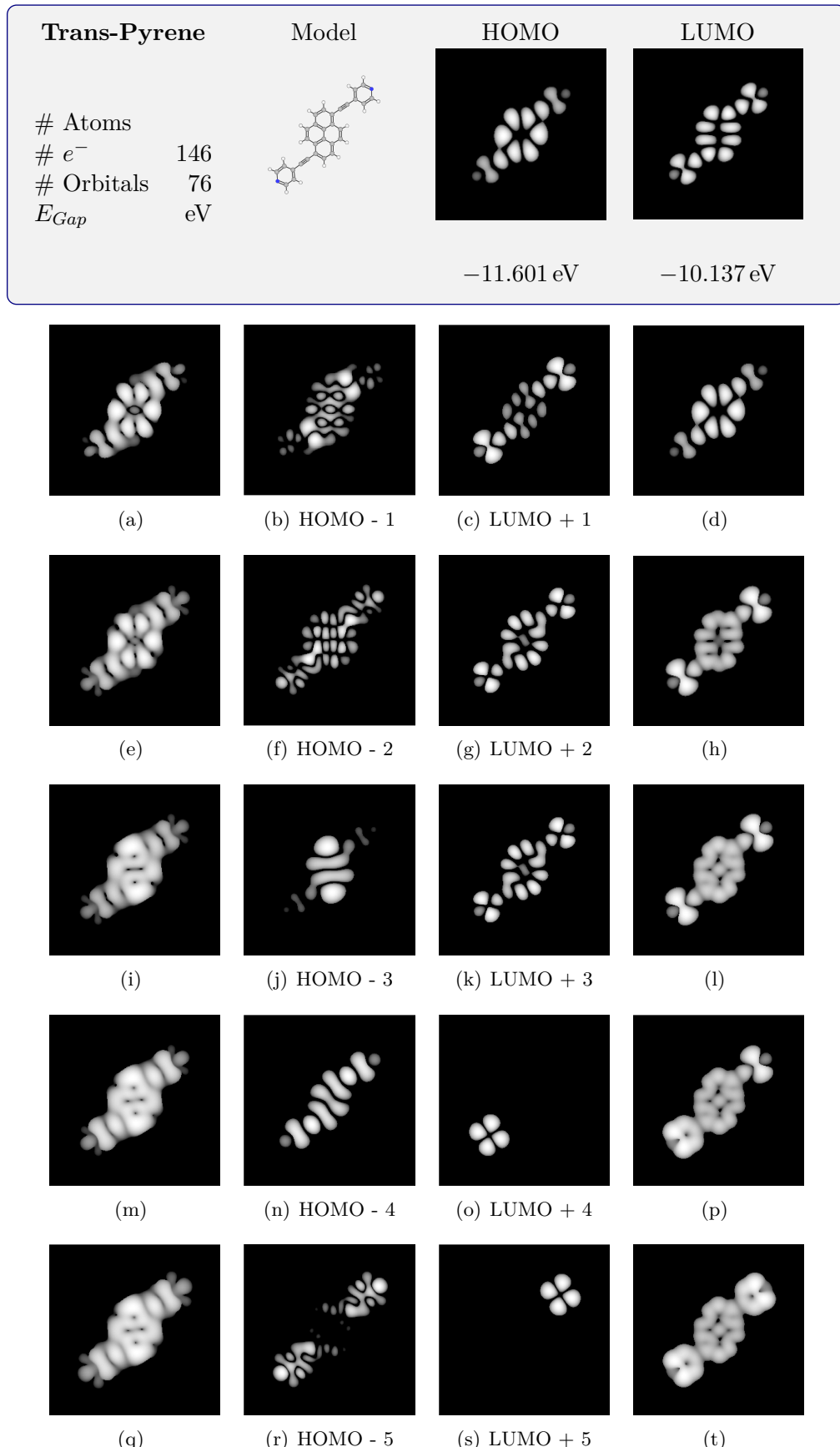


Figure B.10. – EHT calculated molecular orbitals. HOMO and LUMO states together with five neighboring states (shown in the same column). Inner two columns show HOMO & LUMO states. Outer columns show integration of states as STM image estimation if all states to E_F were contributing equally. Images are 2.5 nm wide

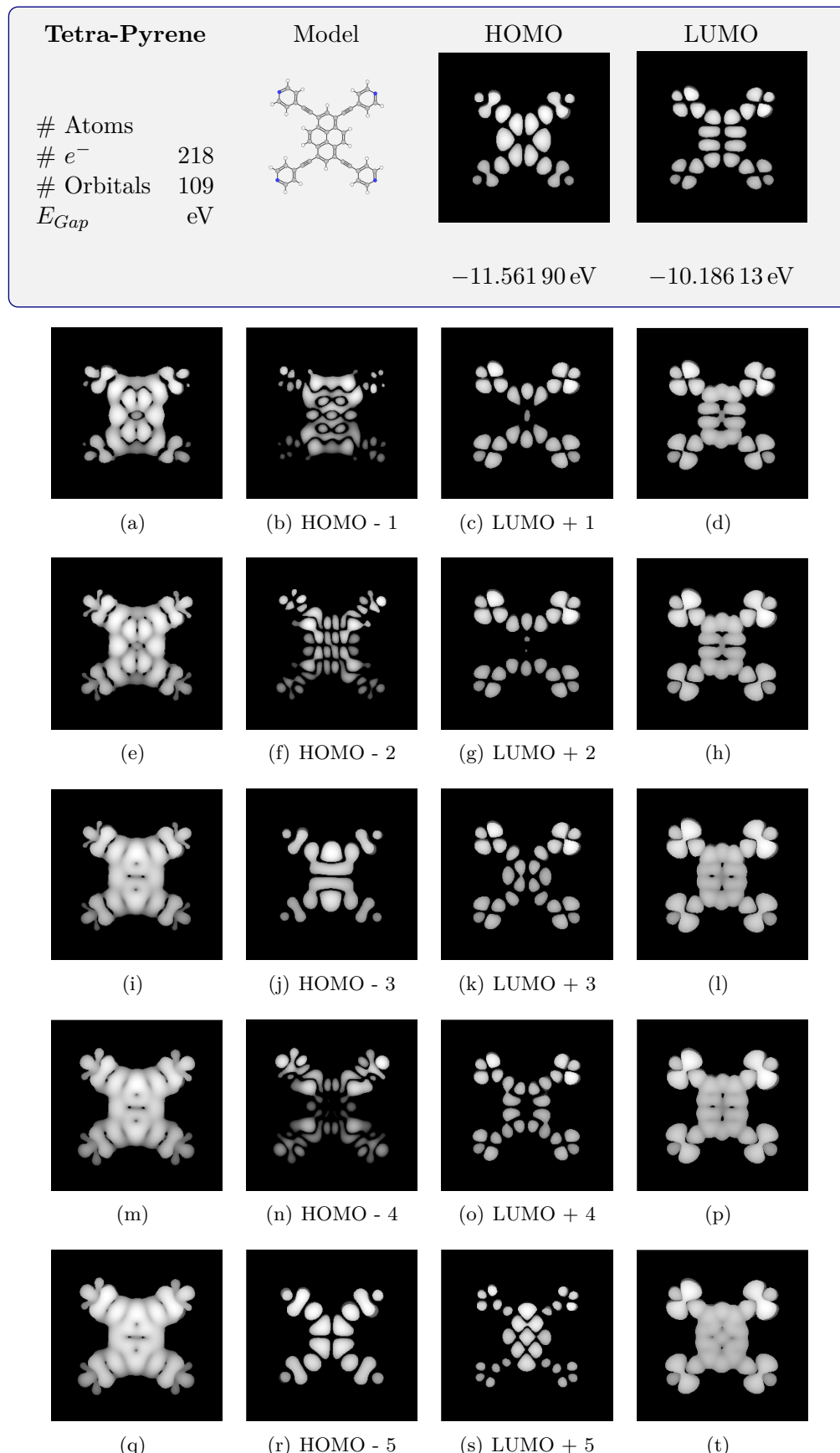


Figure B.11. – EHT calculated molecular orbitals. HOMO and LUMO states together with five neighboring states (shown in the same column). Inner two columns show HOMO & LUMO states. Outer columns show integration of states as STM image estimation if all states to E_F were contributing equally. Images are 2.5 nm wide

C. TBP

C.1. How to determine molecules' distance

To determine the distance between molecules, one has to carefully choose the points of interest. As a problem of STM imaging the contour of the molecules sometimes appears as more or less fuzzy shape. There is no sharp edge that one could take as start or end point of the profile. Therefore the center of the molecule is often used as reference point to measure the distance between two molecules (compare fig. C.1). As the molecule has a square footprint, one can use the center in one direction (along profile 2/3) to determine the center in the other direction (profile 1). As one can see the three profiles match leading to a consistent center of the dimer. This is also shown as depression in profile 1.

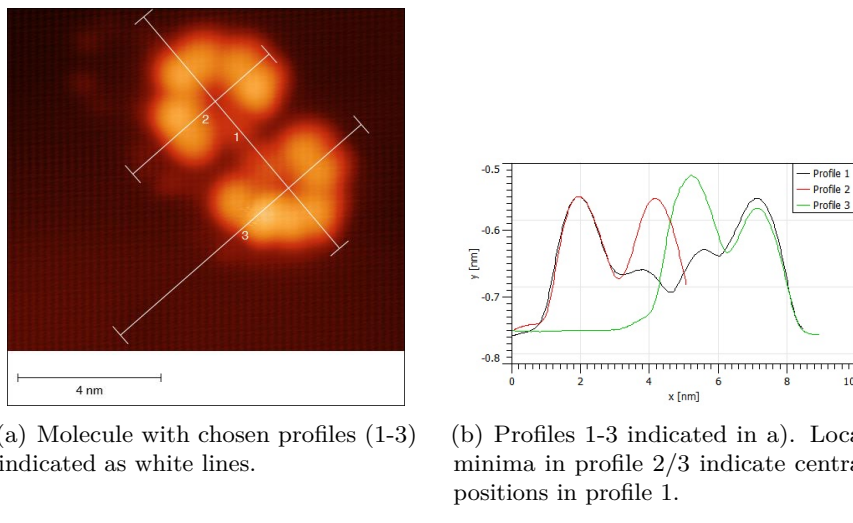


Figure C.1. – Sketch of how to determine the distance between two molecules. As the molecule is square (with the exception of one direction, one can determine the center of the molecule by comparing two 90 deg rotated profiles. Profile 1 goes through the symmetry axis, while profile 2 and 3 intersect profile 1 at the center. As the profile 2 and 3 look the same when starting at the butyl groups, one can use the depression in profile 2 and 3 to determine the center of the molecule in profile 1.

C.2. Ordered areas

Only a single ordered area of TBP on Ag(100) was found, but its structure could not be resolved properly due to tip issues (compare figure C.2). Its unit cell looks hexagonal with roughly 1.7 nm period.

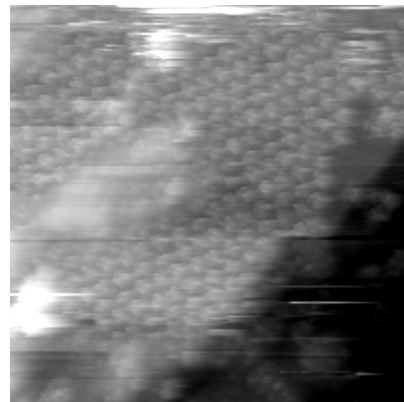


Figure C.2. – TBP on Ag(100) showing some ordering

C.3. TBP on Ag(100) - Symmetry relations

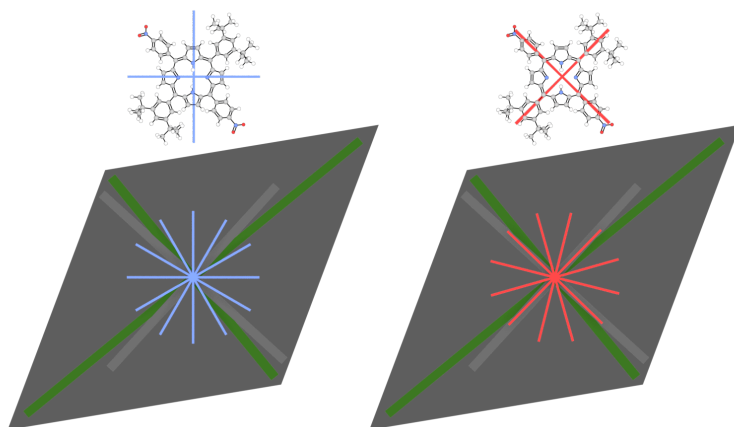


Figure C.3. – Symmetry relations between TBP molecule and Ag(100) crystal substrate. The same molecular model is highlighted in two different ways, emphasizing the two molecular axis (red/blue). Since the assembly is made up of three different orientations, the three rotated axis sets are shown. The assemblies derived unit cell is shown as shaded background with short and long symmetry axis highlighted in green. The crystal orientation from another preparation on the same single crystal is shown in grey.

D. HBBNC

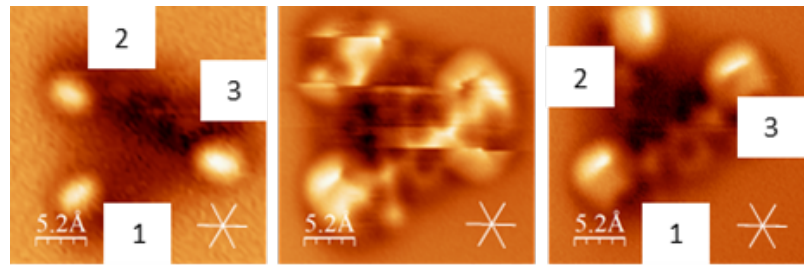


Figure D.1. – Conformational change of a HBBNC monomer after several scans with the AFM. First the molecule starts with an orientation of the legs in 1: clockwise, 2: counterclockwise, 3: clockwise. After several scans in close proximity legs at positions 2 and 3 flip around and change their orientation to 1: clockwise, 2: clockwise, 3: counterclockwise. This results in a changed adsorption geometry. First the upper right edge is lifted from the substrate, while after the leg rearrangement the lower right edge is lifted from the surface. This is caused by the lower lying dimethyl groups lifting the phenyl ring and the molecule's edge connected to it.

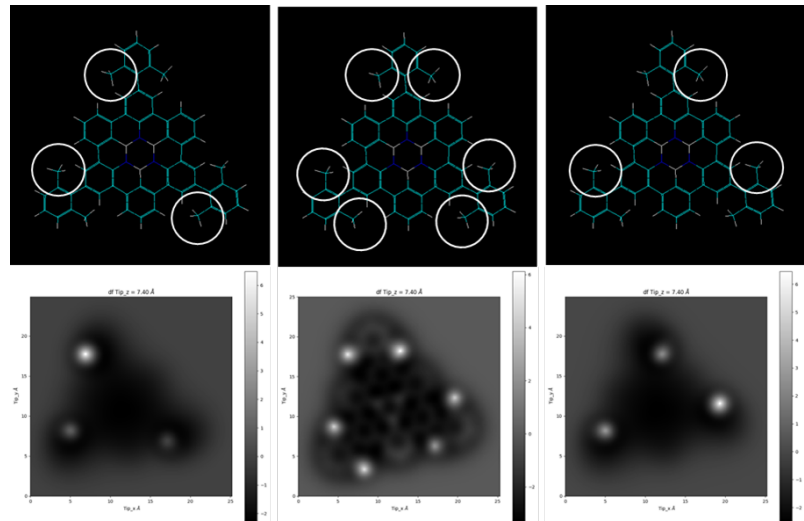
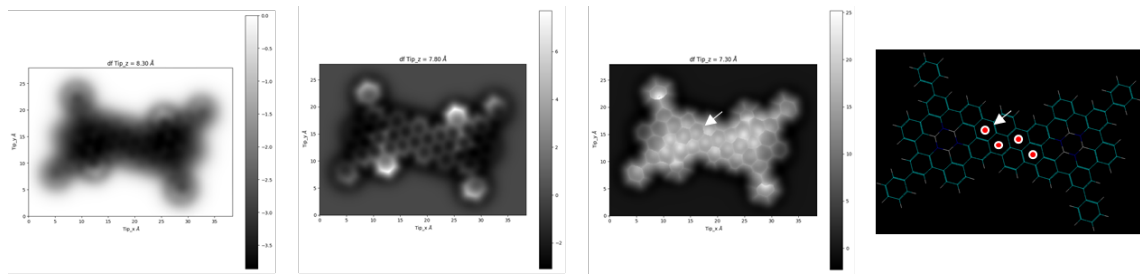
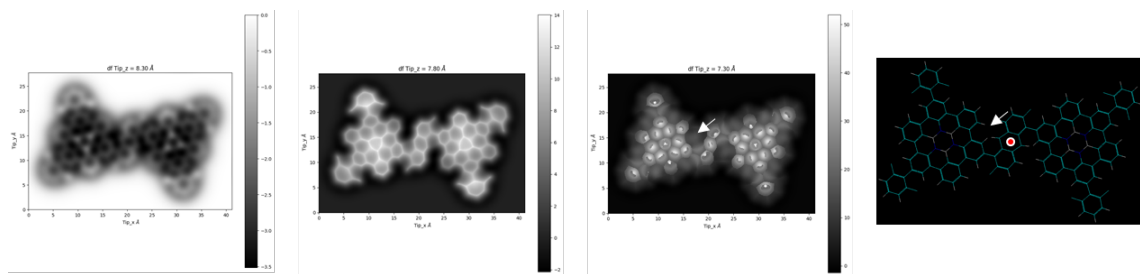


Figure D.2. – Calculated AFM images for freestanding HBBNC. The coronene has been aligned to lie flat in the image plane. Three different leg rotations are shown. The highest features are enclosed by white circles. In the middle column, all phenyl rings are parallel to the image plane, resulting in six features in the calculated image above the dimethyl groups. Columns to the left/right show AFM images as would be expected by a rotation of the dimethylphenyl rings by $\pm 20^\circ$. The rotation direction is chosen as described in Figure D.1 and reproduces the highest appearing spots in the AFM images well. The used code was published as web tool [211] and bases on [212, 213].



(a) Variable height simulated AFM images for type I connection.



(b)

Figure D.3. – Simulated AFM images showing the change in structure of a dimer formed by two different binding motifs as explained in Figure 6.7. Calculated AFM images given for three different heights. An arrow is placed next to spots where experimental identification between the two types is difficult and requires best tip conditions. New features visible in AFM are highlighted by a dot in the molecular model.

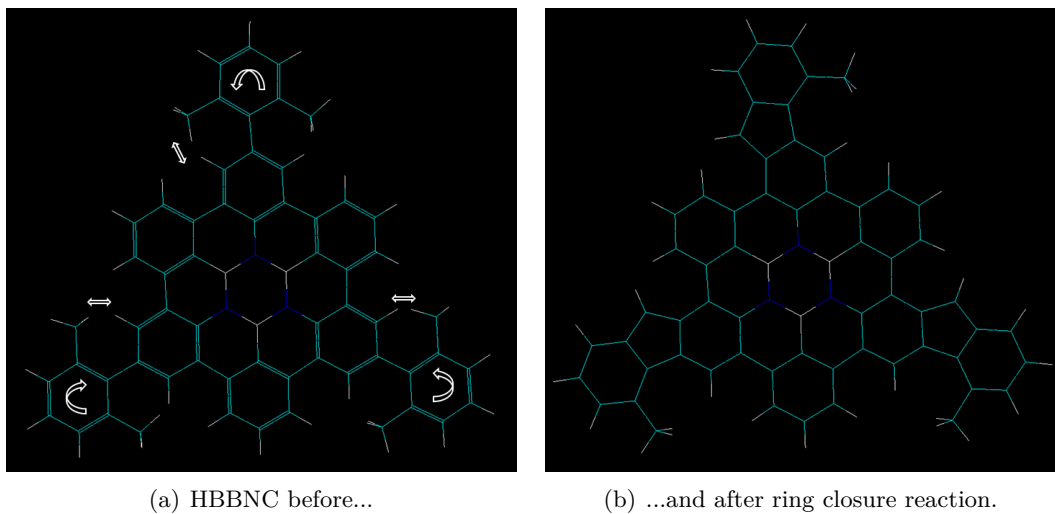


Figure D.4. – Possible ring closure reaction after annealing HBBNC. (a) In HBBNC the upper and right leg are rotated counterclockwise and the methyl group links with the coronene body. This creates a new 5-membered ring and bends the leg. A connection with opposing direction (clockwise) is present for the left leg. (b) Depending on the turn direction of the di-methyl-phenyl leg, two turn directions of the modified leg functionalization form.

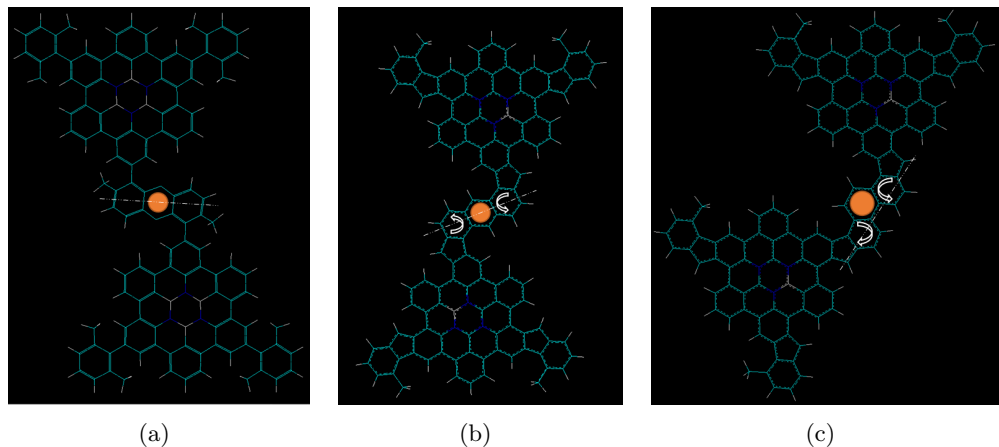


Figure D.5. – Same bond formation (methyl groups create new carbon rings with adjacent methyl-phenyl rings) for (a) pristine HBBNC and its ring closure counterpart. (b),(c). (b) Two legs with the same turn direction connect and result in a straight line between newly formed ring and the already present phenyl legs. (c) Two opposite turn directions are linked in the same bond type but the new formed ring does not lie on the connection line between legs. Compared to the previously derived connection between unaltered molecules, the connection for ring-closure molecules is formed at an different angle to the molecular backbone and may help identify the type of bond.

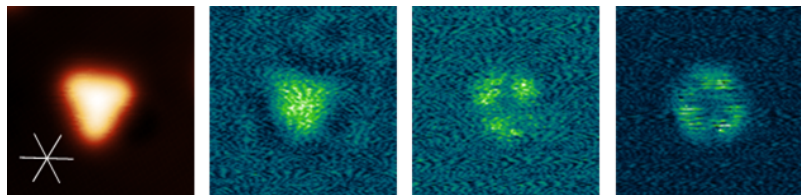


Figure D.6. – STM Topography image and dI/dV maps for chosen energies. Choosing the spectroscopy energy to match one of the spectral maxima of the line spectra reveals the spatial distribution of electronic states as shown by the maps. While at 650 meV only the core contributes to the DOS, energies of 1200 meV and 1600 meV are located on the leg and edge positions respectively.

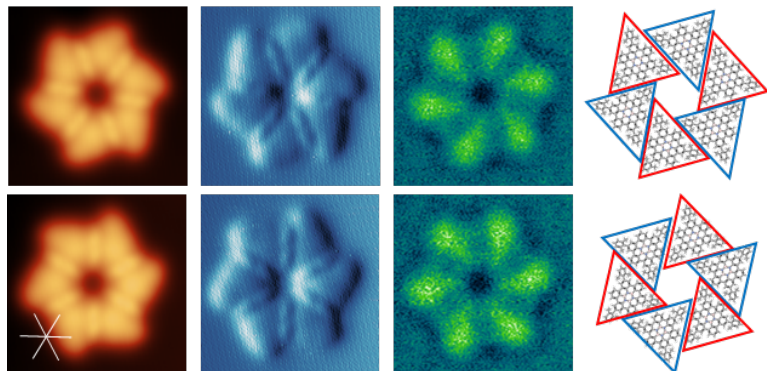


Figure D.7. – Comparison of two hexamers. While in STM the most apparent change is the orientation of the hexamer and the change in the star shaped protrusion, dI/dV maps (600 meV) emphasize the turn direction of the hexamer and its mirror image.

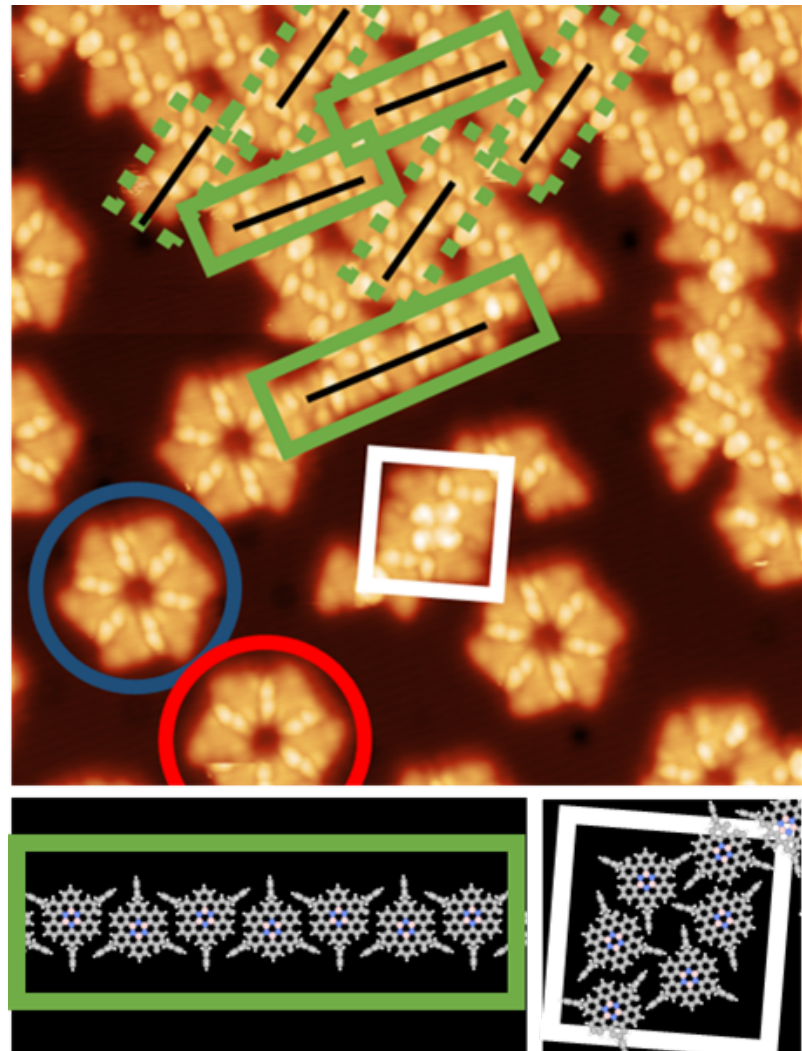


Figure D.8. – Medium coverage adsorption of HBBNC at RT on Ag(111). While the chiral assemblies are still present (blue/red circles), additional binding motifs like chains (green boxes) occur. Square binding motifs are less frequent (white box). Imaging parameter: 22.1 nm, 2 V, 0.4 nA, Color scale: 0 pm to 400 pm.

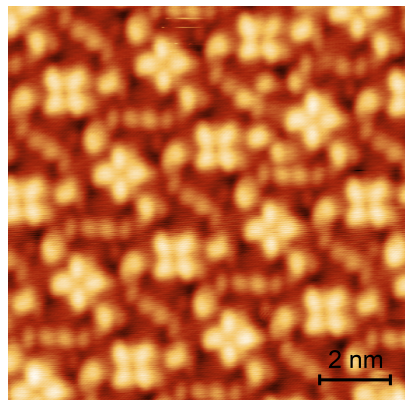


Figure D.9. – STM topography image for high coverage adsorption of HBBNC at RT on Ag(111). The dominating pattern is the clover-leaf resembling the one observed for medium coverage. It is present here in two different orientations and distributed such that neighboring squares do not show the same orientation. Two squares with the same orientation are separated by lines made up of four bright spots aligned parallel to the square edge and diagonal. Squares with different rotations show a single protrusion with larger apparent height. Imaging parameter: 11.07 nm, -250 mV, 0.2 nA.

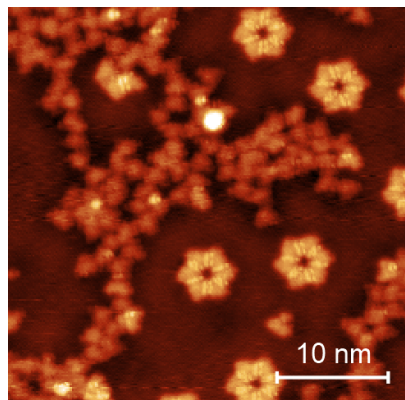


Figure D.10. – STM topography image for a RT preparation of HBBNC on Ag(111) that is annealed to 420 °C. After cooling down to RT, additional HBBNC molecules are deposited and the sample is investigated at l_{He} temperatures. The sample shows both typical features present for an annealed sample (percolated network formation) and RT assembly (hexamers). Imaging parameter: 35 nm, -70 mV, 5 pA., Color scale 0 pm to 250 pm

D.1. Extended Hückel theory calculations

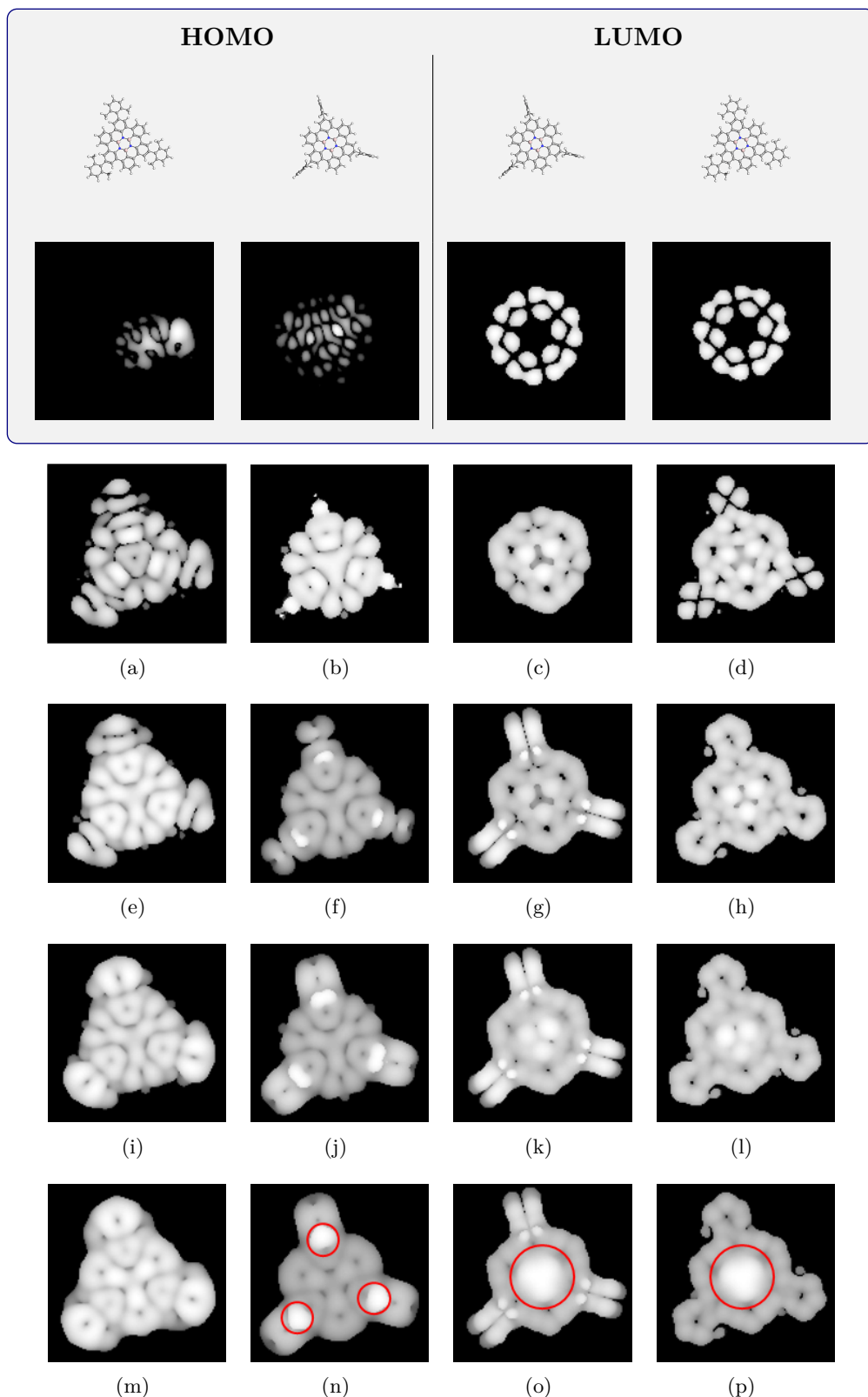


Figure D.11. – Integrated EHT calculated molecular orbitals for two leg configurations of HBBNC. Inner two columns show molecular configuration as predicted by a B3LYP structure optimization. Here the coronene center is parallel to the image plane while the legs are oriented with 90° rotation. Outer columns show the molecule with rotated di-methyl functionalization to lie in the image plane. The difference in shape at the leg functionalization is best visible for occupied states as opposed to unoccupied states where similar features develop at the center. Images are 2.5 nm wide.

E. Helicene

Some experiments were done to test the thermal stability of the self-assembly. Therefor the molecules are deposited at room temperature in subsequently annealed to higher temperatures and investigated in LT-STM (**Figure E.1**). Moderate annealing to 100 °C leads to almost no changes, the chains maintain their shapes. At intermediate temperatures a ring closure reaction between the first and last carbon ring is induced, resulting in a new species. Its appearance is flat in LT-STM. As the temperature increases, they start to disintegrate into smaller fragments with no dominant binding motif.

A closer look revealed that some of the molecules start to change their appearance after annealing. The height of single molecules reduces and the distinct bright spot in the molecule vanishes (**Figure E.1a**). Modelling a dcdb-[5]H with Hyperchem (AM1) where first and last carbon rings are fused together matches this shape very well, pointing to an temperature induced ring closure reaction (**Figure E.2b**), which suppresses chirality of the new formed species. These often but not attach to the initial molecular assembly or agglomerate in unordered configurations. A cyclodehydrogenation is observed for double 5[H] on Au(111) at 380 °C [214] and dibenzo[i,o]heptahelicene on Ag(111) at 247 °C to 397 °C [215]. Heptahelicene/Cu(111) decomposes above 227 °C [201]. Investigation of [7]H on Ni(111) and Ni(100) revealed dehydrogenation temperatures not below 227 °C and 127 °C respectively.[216]

Chains formed at RT on Ag(111) bear significantly more molecules than those formed on Ag(100) and are almost exclusively made of two strands - thus are 4 molecules wide. This is shown as histogram representation in **Figure E.3**. Only some chains are three strands wide.

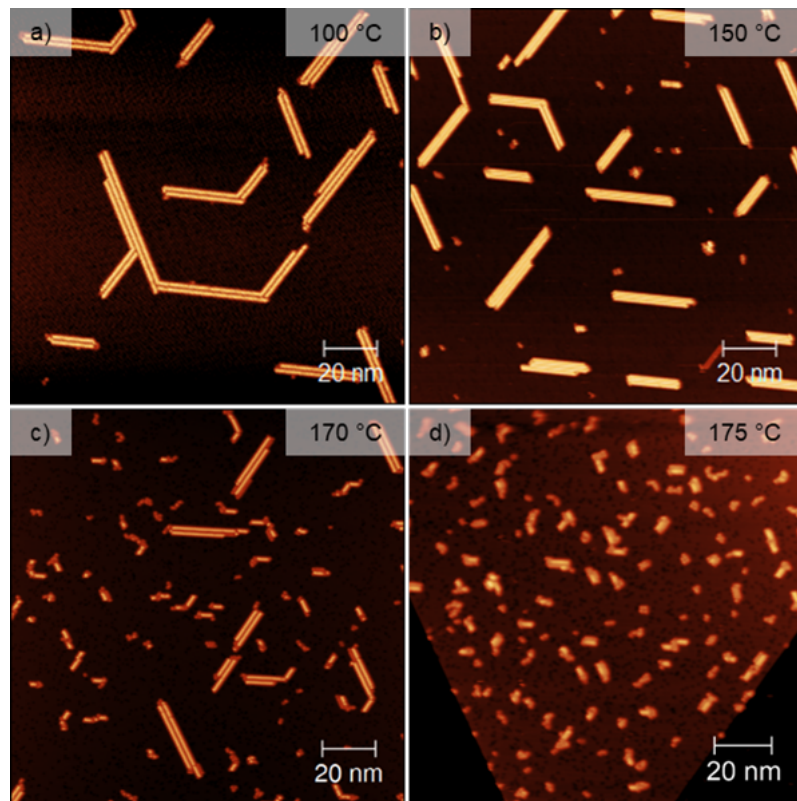


Figure E.1. – After adsorption at RT on Ag(111) the same sample was subsequently heated to 100/150/170 °C (a-c) and investigated in LT-STM. The higher the annealing temperature gets, the shorter the chains become. At intermediate temperature ring closure reactions form flat compounds. At longer annealing times at elevated temperature (175 °C, 30 min, d) the molecules start to form denser but more unordered configurations while the typical chain length of the assembly further decreases.

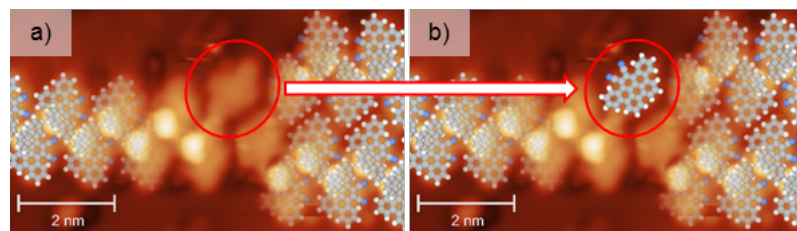


Figure E.2. – Upon heating to the Ag(111) to 170 °C for 10 min some molecules start to change their typical appearance (red circle in a)). They lose their bright feature and become flat. A molecule's model representation with its first and last carbon rings connected is shown in b) closely resembling the footprint of the new species.

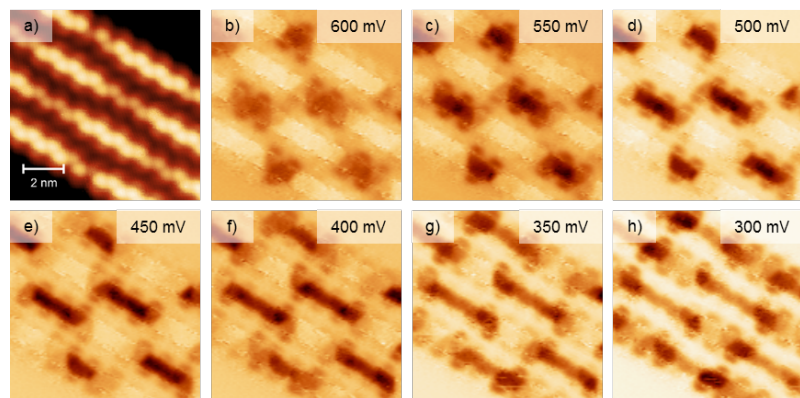


Figure E.3. – (a) Topography of a molecular chain along the Ag(100) high symmetry direction recorded at 400 mV. (b-h) dI/dV maps ranging from 600 mV to 300 mV. The periodic height modulation visible in the topography can be recognized in the dI/dV maps. The width of the features decreases with decreasing bias voltage.

F. Peltier cooling unit

Here the setup of the peltier-cooling unit is described. It is used for cooled storage of borazine, a liquid precursor used to grow *h*-BN via CVD.

The precursor containing glass tube is surrounded by a hollow cylinder made of copper that is cooled via the cold side of a peltier element at its bottom. The hot side is connected to a thermal mass which is held at RT by a CPU socket fan (LGA775). For thermal insulation to the environment, the cold hollow cylinder is surrounded by a acrylic glass. When possible, the volume between copper and acrylic cylinder should be sealed to prevent water vapor to condense and freeze on the cold copper surface.

When used in the setup shown below (Figure F.1), operating temperatures down to -5°C are achievable with ambient temperatures around 20°C . If lower temperatures are needed, one may either increase the power of the peltier element (either by increasing the single element power or stacking several ones) or decrease the temperature of the hot side below RT (by water-cooling).

Peltier elements should be sealed to prevent moisture uptake that would quickly degrade the elements or shortcut the contacts. The maintenance interval mainly depends on the quality of the peltier element in use, since it is more fragile than the fan or the power supplies. Attention should be paid while checking the cabling of the peltier element. Its welding spots are usually very small and brittle. Once loose, a repair is unlikely.

F. Peltier cooling unit

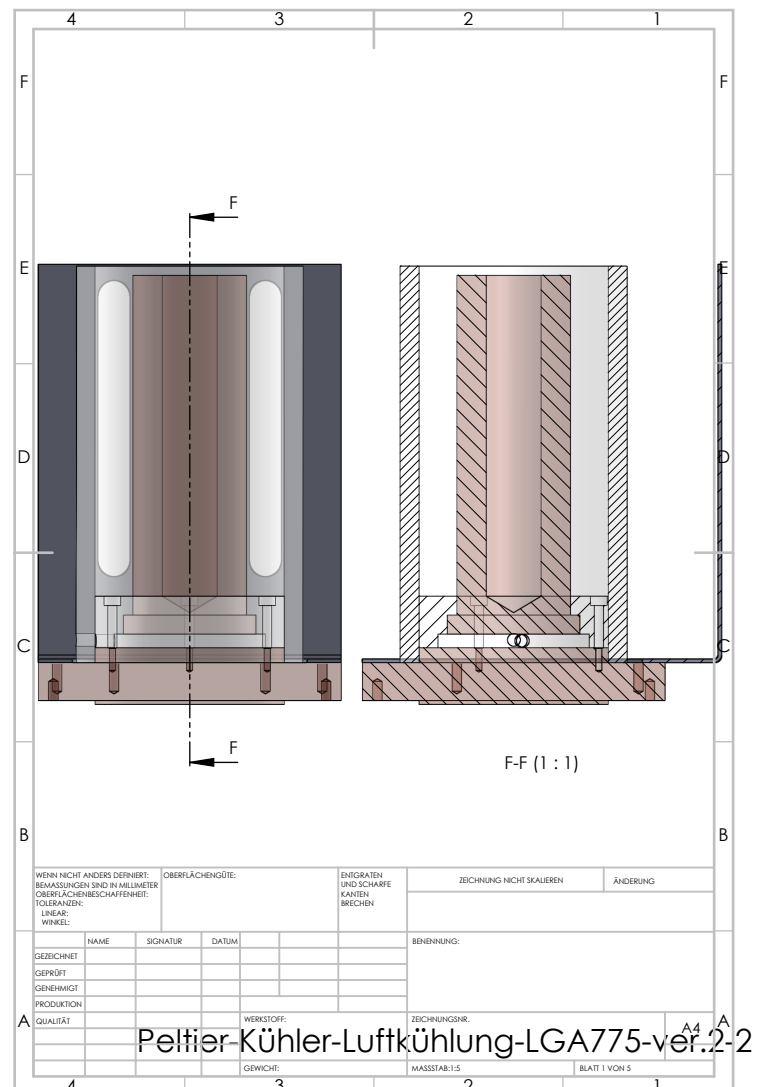


Figure F.1. – Design of a peltier cooling unit used to store the liquid borazine precursor below 5 °C. The precursor is surrounded by a rather tight fitting copper cylinder. Its thermal energy is permanently lowered by the peltier element that in turn rises the temperature of the lower copper plate. To keep it at room temperature, a CPU heat sink is attached (not shown in the sketch). A acrylic glass cylinder surrounds the cooled parts to prevent air moisture to condense and freeze on the copper. An "L" shaped mounting bracket with slotted holes ensures an easy fix of the cooler at the frame in various positions and angles.

Bibliography

- [1] M. F. Crommie, C. P. Lutz, and D. M. Eigler. “Confinement of Electrons to Quantum Corrals on a Metal Surface”. In: *Science* 262.5131 (Oct. 8, 1993), pp. 218–220. ISSN: 0036-8075, 1095-9203. DOI: 10.1126/science.262.5131.218. URL: <http://www.sciencemag.org/cgi/doi/10.1126/science.262.5131.218> (visited on 02/18/2019).
- [2] Jagdish Mehra and Helmut Rechenberg. *The Historical Development of Quantum Theory*. 1st ed. New York: Springer-Verlag New York, Mar. 1986. ISBN: 978-0-387-95174-4.
- [3] J. Bardeen. “Tunnelling from a Many-Particle Point of View”. In: *Phys. Rev. Lett.* 6 (2 Jan. 1961), pp. 57–59. DOI: 10.1103/PhysRevLett.6.57. URL: <https://link.aps.org/doi/10.1103/PhysRevLett.6.57>.
- [4] Russell Young, John Ward, and Fredric Scire. “The Topografiner: An Instrument for Measuring Surface Microtopography”. In: *Review of Scientific Instruments* 43.7 (1972), pp. 999–1011. DOI: 10.1063/1.1685846. eprint: <https://doi.org/10.1063/1.1685846>. URL: <https://doi.org/10.1063/1.1685846>.
- [5] G. Binnig et al. “Tunneling through a controllable vacuum gap”. In: *Applied Physics Letters* 40.2 (1982), pp. 178–180. DOI: 10.1063/1.92999. eprint: <https://doi.org/10.1063/1.92999>. URL: <https://doi.org/10.1063/1.92999>.
- [6] Gerd Binnig et al. “7x7 reconstruction on Si (111) resolved in real space”. In: *Physical review letters* 50.2 (1983), p. 120. URL: <http://journals.aps.org/prl/abstract/10.1103/PhysRevLett.50.120> (visited on 07/16/2015).
- [7] *The Nobel Prize in Physics 1986*. Nov. 1, 2018. URL: <https://www.nobelprize.org/prizes/physics/1986/summary/> (visited on 11/01/2018).
- [8] Michael Schunack. “Scanning Tunneling Microscopy Studies of Organic Molecules on Metal Surfaces”. PhD thesis. Denmark: University of Aarhus. 180 pp.
- [9] Samir Lounis. “Theory of Scanning Tunneling Microscopy”. In: *arXiv:1404.0961 [cond-mat]* (Apr. 3, 2014). arXiv: 1404.0961. URL: <http://arxiv.org/abs/1404.0961> (visited on 08/09/2018).

- [10] Daniel Wortmann. “Interpretation of Scanning Tunneling Microscopy and Spectroscopy of Magnetic Metal Surfaces by Electron Theory”. PhD thesis. Dortmund: Universität Dortmund, 2000. 100 pp. URL: www.fz-juelich.de/SharedDocs/Downloads/PGI/PGI-1/EN/Wortmann.dipl_pdf.pdf?__blob=publicationFile (visited on 08/23/2018).
- [11] Dr. R. Temirov. *Versuch: Low Temperature Scanning Tunnelling Microscopy and Spectroscopy in Ultrahigh Vacuum*. Nov. 1, 2018. URL: http://www.fz-juelich.de/SharedDocs/Downloads/PGI/PGI-3/Gruppe2/NanoelectronicCourseLab/Experiments/V17Script.pdf?__blob=publicationFile (visited on 11/01/2018).
- [12] Gregor Wentzel. “Eine Verallgemeinerung der Quantenbedingungen für die Zwecke der Wellenmechanik”. In: *Zeitschrift für Physik* 38.6 (June 1926), pp. 518–529. ISSN: 1434-6001, 1434-601X. DOI: [10.1007/BF01397171](https://doi.org/10.1007/BF01397171). URL: <http://link.springer.com/10.1007/BF01397171> (visited on 08/23/2018).
- [13] H. A. Kramers. “Wellenmechanik und halbzahlige Quantisierung”. In: *Zeitschrift für Physik* 39.10 (Oct. 1926), pp. 828–840. ISSN: 1434-6001, 1434-601X. DOI: [10.1007/BF01451751](https://doi.org/10.1007/BF01451751). URL: <http://link.springer.com/10.1007/BF01451751> (visited on 08/23/2018).
- [14] Léon Brillouin. “La mécanique ondulatoire de Schrödinger: une méthode générale de resolution par approximations successives”. In: *Comptes Rendus de l'Académie des Sciences* 183 (1926), pp. 24–26.
- [15] R. M. Tromp, R. J. Hamers, and J. E. Demuth. “Atomic and electronic contributions to Si (111)-(7x7) scanning-tunneling-microscopy images”. In: *Physical Review B* 34.2 (1986), p. 1388. URL: <http://journals.aps.org/prb/abstract/10.1103/PhysRevB.34.1388> (visited on 07/16/2015).
- [16] Dawn A. Bonnell, ed. *Scanning tunneling microscopy and spectroscopy: theory, techniques, and applications*. New York, N.Y: VCH, 1993. 436 pp. ISBN: 978-0-89573-768-7.
- [17] Sven Zöphel. “Der Aufbau eines Tieftemperatur-Rastertunnelmikroskops und Strukturuntersuchungen auf vicinalen Kupferoberflächen”. PhD thesis. Freie Universität Berlin, 2000. URL: https://refubium.fu-berlin.de/bitstream/handle/fub188/6080/0_gesamt.pdf?sequence=1&isAllowed=y.
- [18] *Shematics of beetle-type STM design*. Nov. 6, 2018. URL: https://www.researchgate.net/figure/Schematics-of-the-modified-beetle-type-STM-design-employed-for-the-present-setup-Three_fig9_30514461 (visited on 11/06/2018).

- [19] Knud Seufert. “Surface anchored porphyrins - investigations of assembly, reactivity, manipulation and in-situ synthesis”. PhD thesis. München: Technische Universität München. 184 pp.
- [20] *The Bartynski Group*. 2006. URL: <http://www.physics.rutgers.edu/Bartgroup/STM.htm> (visited on 08/10/2018).
- [21] José Ignacio Urgel Tendero. “Two-dimensional lanthanide-directed metal-organic networks at surfaces”. PhD thesis. München: Technische Universität München, Dec. 17, 2015. 161 pp. URL: <http://nbn-resolving.de/urn/resolver.pl?urn:nbn:de:bvb:91-diss-20160311-1286634-1-7>.
- [22] Martin Schwarz. “Assembly and Characterization of Hybrid Nanomaterials on Noble Metal Surfaces”. PhD thesis. München: Technische Universität München, June 12, 2018. 240 pp. URL: <https://mediatum.ub.tum.de/doc/1436091/1436091.pdf>.
- [23] Alissa Wiengarten. “Scanning tunneling microscopy investigation of structure and electronic properties of surface-confined tetrapyrrolic species”. PhD thesis. München: Technische Universität München, July 21, 2015. 134 pp. URL: <http://nbn-resolving.de/urn/resolver.pl?urn:nbn:de:bvb:91-diss-20150723-1256606-1-5>.
- [24] P. Sautet and C. Joachim. “Interpretation of STM images: copper-phthalocyanine on copper”. In: *Surface Science* 271.3 (Jan. 1992), pp. 387–394. ISSN: 00396028. DOI: 10.1016/0039-6028(92)90902-I. URL: <http://linkinghub.elsevier.com/retrieve/pii/003960289290902I> (visited on 07/13/2015).
- [25] J. Tersoff and D. R. Hamann. “Theory of the scanning tunneling microscope”. In: *Physical Review B* 31.2 (Jan. 15, 1985), pp. 805–813. ISSN: 0163-1829. DOI: 10.1103/PhysRevB.31.805. URL: <https://link.aps.org/doi/10.1103/PhysRevB.31.805> (visited on 08/23/2018).
- [26] N. D. Lang. “Theory of Single-Atom Imaging in the Scanning Tunneling Microscope”. In: *Physical Review Letters* 56.11 (Mar. 17, 1986), pp. 1164–1167. ISSN: 0031-9007. DOI: 10.1103/PhysRevLett.56.1164. URL: <https://link.aps.org/doi/10.1103/PhysRevLett.56.1164> (visited on 08/23/2018).
- [27] D. M. Eigler et al. “Imaging Xe with a low-temperature scanning tunneling microscope”. In: *Physical Review Letters* 66.9 (Mar. 4, 1991), pp. 1189–1192. ISSN: 0031-9007. DOI: 10.1103/PhysRevLett.66.1189. URL: <https://link.aps.org/doi/10.1103/PhysRevLett.66.1189> (visited on 08/23/2018).

- [28] H. Hertz. “Ueber einen Einfluss des ultravioletten Lichtes auf die electrische Entladung”. In: *Annalen der Physik* 267.8 (1887), pp. 983–1000. ISSN: 1521-3889. DOI: 10.1002/andp.18872670827. URL: <http://onlinelibrary.wiley.com/doi/10.1002/andp.18872670827/abstract> (visited on 01/12/2015).
- [29] *The Nobel Prize in Physics 1921*. Jan. 15, 2015. URL: http://www.nobelprize.org/nobel_prizes/physics/laureates/1921/index.html (visited on 01/12/2015).
- [30] Dmitry Y Zemlyanov et al. “Versatile technique for assessing thickness of 2D layered materials by XPS”. In: *Nanotechnology* 29.11 (Mar. 16, 2018), p. 115705. ISSN: 0957-4484, 1361-6528. DOI: 10.1088/1361-6528/aaa6ef. URL: <http://stacks.iop.org/0957-4484/29/i=11/a=115705?key=crossref.c55893e7cb47891c5800779a12eb31ed> (visited on 08/10/2018).
- [31] *The Nobel Prize in Physics 1981*. Nov. 1, 2018. URL: <https://www.nobelprize.org/prizes/physics/1981/summary/> (visited on 11/01/2018).
- [32] *XPS_PHYSICS.png*. Jan. 12, 2015. URL: http://upload.wikimedia.org/wikipedia/commons/0/07/XPS_PHYSICS.png (visited on 08/10/2018).
- [33] Carsten Busse et al. “Graphene on Ir(111): Physisorption with Chemical Modulation”. In: *Phys. Rev. Lett.* 107.3 (July 2011), p. 036101. DOI: 10.1103/PhysRevLett.107.036101. URL: <http://link.aps.org/doi/10.1103/PhysRevLett.107.036101>.
- [34] Elin Gränäs et al. “Oxygen Intercalation under Graphene on Ir(111): Energetics, Kinetics, and the Role of Graphene Edges”. In: *ACS Nano* 6.11 (Nov. 27, 2012), pp. 9951–9963. ISSN: 1936-0851, 1936-086X. DOI: 10.1021/nn303548z. URL: <http://pubs.acs.org/doi/abs/10.1021/nn303548z> (visited on 10/15/2014).
- [35] C. D. Wanger et al. *Handbook of X-ray Photoelectron Spectroscopy*. Vol. 3. Perkin-Elmer Corp., 1979. 190 pp. URL: <http://onlinelibrary.wiley.com/doi/10.1002/sia.740030412/abstract> (visited on 12/15/2014).
- [36] J.C. Rivière. “Instrumentation”. In: *Auger and X-ray Photoelectron Spectroscopy*. Ed. by D. Briggs and M.P. Seah. Frankfurt am Main: Otto Salle Verlag GmbH & Co., 1990.
- [37] B. L. Henke, E. M. Gullikson, and J. C. Davis. “X-Ray Interactions: Photoabsorption, Scattering, Transmission, and Reflection at E = 50-30,000 eV, Z = 1-92”. In: *Atomic Data and Nuclear Data Tables* 54.2 (July 1993), pp. 181–342. ISSN: 0092-640X. DOI: 10.1006/adnd.1993.1013. (Visited on 12/05/2014).

- [38] M. P. Seah and W. A. Dench. “Quantitative electron spectroscopy of surfaces: A standard data base for electron inelastic mean free paths in solids”. In: *Surface and Interface Analysis* 1.1 (1979), pp. 2–11. DOI: 10.1002/sia.740010103. URL: <https://onlinelibrary.wiley.com/doi/abs/10.1002/sia.740010103>.
- [39] J. E. Jones. “On the Determination of Molecular Fields. II. From the Equation of State of a Gas”. In: *Proceedings of the Royal Society A: Mathematical, Physical and Engineering Sciences* 106.738 (Oct. 1, 1924), pp. 463–477. ISSN: 1364-5021, 1471-2946. DOI: 10.1098/rspa.1924.0082. URL: <http://rspa.royalsocietypublishing.org/cgi/doi/10.1098/rspa.1924.0082> (visited on 08/23/2018).
- [40] Florian Albrecht et al. “Direct Identification and Determination of Conformational Response in Adsorbed Individual Nonplanar Molecular Species Using Noncontact Atomic Force Microscopy”. In: *Nano Letters* 16.12 (Dec. 14, 2016), pp. 7703–7709. ISSN: 1530-6984, 1530-6992. DOI: 10.1021/acs.nanolett.6b03769. URL: <http://pubs.acs.org/doi/10.1021/acs.nanolett.6b03769> (visited on 08/23/2018).
- [41] Shigeki Kawai et al. “Multiple heteroatom substitution to graphene nanoribbon”. In: *Science Advances* 4.4 (Apr. 2018), eaar7181. ISSN: 2375-2548. DOI: 10.1126/sciadv.aar7181. URL: <http://advances.sciencemag.org/lookup/doi/10.1126/sciadv.aar7181> (visited on 05/28/2018).
- [42] Shigeki Kawai et al. “Atomically controlled substitutional boron-doping of graphene nanoribbons”. In: *Nature Communications* 6.1 (Dec. 2015). ISSN: 2041-1723. DOI: 10.1038/ncomms9098. URL: <http://www.nature.com/articles/ncomms9098> (visited on 05/28/2018).
- [43] Fabian Schulz et al. “Elemental Identification by Combining Atomic Force Microscopy and Kelvin Probe Force Microscopy”. In: *ACS Nano* (May 25, 2018). ISSN: 1936-0851, 1936-086X. DOI: 10.1021/acsnano.7b08997. URL: <http://pubs.acs.org/doi/10.1021/acsnano.7b08997> (visited on 06/01/2018).
- [44] L. Gross et al. “The Chemical Structure of a Molecule Resolved by Atomic Force Microscopy”. In: *Science* 325.5944 (Aug. 28, 2009), pp. 1110–1114. ISSN: 0036-8075, 1095-9203. DOI: 10.1126/science.1176210. URL: <http://www.sciencemag.org/cgi/doi/10.1126/science.1176210> (visited on 05/25/2018).
- [45] Niko Pavliček and Leo Gross. “Generation, manipulation and characterization of molecules by atomic force microscopy”. In: *Nature Reviews Chemistry* 1 (Jan. 11, 2017), p. 0005. URL: <http://dx.doi.org/10.1038/s41570-016-0005>.

- [46] Martin Schwarz et al. “Corrugation in the Weakly Interacting Hexagonal-BN/Cu(111) System: Structure Determination by Combining Noncontact Atomic Force Microscopy and X-ray Standing Waves”. In: *ACS Nano* 11.9 (Sept. 26, 2017), pp. 9151–9161. ISSN: 1936-0851, 1936-086X. DOI: 10.1021/acsnano.7b04022. URL: <http://pubs.acs.org/doi/10.1021/acsnano.7b04022> (visited on 07/20/2018).
- [47] Xiao-Ye Wang et al. “Exploration of pyrazine-embedded antiaromatic polycyclic hydrocarbons generated by solution and on-surface azomethine ylide homocoupling”. In: *Nature Communications* 8.1 (Dec. 5, 2017), p. 1948. ISSN: 2041-1723. DOI: 10.1038/s41467-017-01934-1. URL: <https://doi.org/10.1038/s41467-017-01934-1>.
- [48] Yuanqin He. “Bottom-up Construction and Direct Characterization of Porphyrin- and Graphene-based Nanostructures”. PhD thesis. München: Technische Universität München, June 19, 2017. 147 pp. URL: <http://nbn-resolving.de/urn/resolver.pl?urn=nbn:de:bvb:91-diss-20170720-1362063-1-5>.
- [49] *Technical data for the elements in the Periodic Table*. Nov. 11, 2018. URL: <http://periodictable.com/> (visited on 11/11/2018).
- [50] Ferdinand H. Farwick zum Hagen et al. “Structure and Growth of Hexagonal Boron Nitride on Ir(111)”. In: *ACS Nano* (Nov. 14, 2016). ISSN: 1936-0851. DOI: 10.1021/acsnano.6b05819. URL: <http://dx.doi.org/10.1021/acsnano.6b05819> (visited on 11/25/2016).
- [51] Zhang Jian-Min, Ma Fei, and Xu Ke-Wei. “Calculation of the surface energy of fcc metals with modified embedded-atom method”. In: *Chinese Physics* 13.7 (2004), p. 1082. ISSN: 1009-1963. DOI: 10.1088/1009-1963/13/7/020. URL: <http://stacks.iop.org/1009-1963/13/i=7/a=020> (visited on 11/12/2015).
- [52] D. M. Turley and L. E. Samuels. “The nature of mechanically polished surfaces of copper”. In: *Metallography* 14.4 (1981), pp. 275–294. ISSN: 0026-0800. DOI: [https://doi.org/10.1016/0026-0800\(81\)90001-X](https://doi.org/10.1016/0026-0800(81)90001-X). URL: <http://www.sciencedirect.com/science/article/pii/002608008190001X>.
- [53] Kenji Watanabe, Takashi Taniguchi, and Hisao Kanda. “Direct-bandgap properties and evidence for ultraviolet lasing of hexagonal boron nitride single crystal”. en. In: *Nature Materials* 3.6 (June 2004), pp. 404–409. ISSN: 1476-1122, 1476-4660. DOI: 10.1038/nmat1134. URL: <http://www.nature.com/articles/nmat1134> (visited on 11/06/2018).

- [54] G. Cassabois, P. Valvin, and B. Gil. “Hexagonal boron nitride is an indirect bandgap semiconductor”. en. In: *Nature Photonics* 10.4 (Apr. 2016), pp. 262–266. ISSN: 1749-4885, 1749-4893. DOI: 10.1038/nphoton.2015.277. URL: <http://www.nature.com/articles/nphoton.2015.277> (visited on 11/06/2018).
- [55] X. Blase et al. “Quasiparticle band structure of bulk hexagonal boron nitride and related systems”. en. In: *Physical Review B* 51.11 (Mar. 1995), pp. 6868–6875. ISSN: 0163-1829, 1095-3795. DOI: 10.1103/PhysRevB.51.6868. URL: <https://link.aps.org/doi/10.1103/PhysRevB.51.6868> (visited on 11/06/2018).
- [56] Tongwei Han, Ying Luo, and Chengyuan Wang. “Effects of temperature and strain rate on the mechanical properties of hexagonal boron nitride nanosheets”. In: *Journal of Physics D: Applied Physics* 47.2 (2014), p. 025303. URL: <http://stacks.iop.org/0022-3727/47/i=2/a=025303>.
- [57] Bohayra Mortazavi and Yves Rémond. “Investigation of tensile response and thermal conductivity of boron-nitride nanosheets using molecular dynamics simulations”. In: *Physica E: Low-dimensional Systems and Nanostructures* 44.9 (2012), pp. 1846–1852. ISSN: 1386-9477. DOI: <http://dx.doi.org/10.1016/j.physe.2012.05.007>. URL: <http://www.sciencedirect.com/science/article/pii/S1386947712001804>.
- [58] M. Topsakal, E. Aktürk, and S. Ciraci. “First-principles study of two- and one-dimensional honeycomb structures of boron nitride”. In: *Phys. Rev. B* 79.11 (Mar. 2009), p. 115442. DOI: 10.1103/PhysRevB.79.115442. URL: <http://link.aps.org/doi/10.1103/PhysRevB.79.115442>.
- [59] Qing Peng, Wei Ji, and Suvernu De. “Mechanical properties of the hexagonal boron nitride monolayer: Ab initio study”. In: *Computational Materials Science* 56.0 (2012), pp. 11–17. ISSN: 0927-0256. DOI: <http://dx.doi.org/10.1016/j.commatsci.2011.12.029>. URL: <http://www.sciencedirect.com/science/article/pii/S0927025611006902>.
- [60] W. Paszkowicz et al. “Lattice parameters and anisotropic thermal expansion of hexagonal boron nitride in the 10–297.5K temperature range”. In: *Applied Physics A* 75.3 (2002), pp. 431–435. ISSN: 0947-8396. DOI: 10.1007/s003390100999. URL: <http://dx.doi.org/10.1007/s003390100999>.
- [61] Frank Müller et al. “Epitaxial growth of hexagonal boron nitride on Ag(111)”. In: *Phys. Rev. B* 82.11 (Sept. 2010), p. 113406. DOI: 10.1103/PhysRevB.82.113406. URL: <http://link.aps.org/doi/10.1103/PhysRevB.82.113406>.

- [62] Frank Müller, Stefan Hüfner, and Hermann Sachdev. “One-dimensional structure of boron nitride on chromium (110) – a study of the growth of boron nitride by chemical vapour deposition of borazine”. en. In: *Surface Science* 602.22 (Nov. 2008), pp. 3467–3476. ISSN: 00396028. DOI: 10.1016/j.susc.2008.06.037. URL: <http://linkinghub.elsevier.com/retrieve/pii/S0039602808004287> (visited on 11/06/2018).
- [63] Ning Guo et al. “Controllable growth of triangular hexagonal boron nitride domains on copper foils by an improved low-pressure chemical vapor deposition method”. In: *Nanotechnology* 23.41 (Oct. 19, 2012), p. 415605. ISSN: 0957-4484, 1361-6528. DOI: 10.1088/0957-4484/23/41/415605. URL: <http://stacks.iop.org/0957-4484/23/i=41/a=415605?key=crossref.113b515178c834c75ca332235bf20bf1> (visited on 10/15/2014).
- [64] Gene Siegel et al. “Heterogeneous Pyrolysis: A Route for Epitaxial Growth of hBN Atomic Layers on Copper Using Separate Boron and Nitrogen Precursors”. In: *Nano Letters* 17.4 (Apr. 12, 2017), pp. 2404–2413. ISSN: 1530-6984, 1530-6992. DOI: 10.1021/acs.nanolett.6b05409. URL: <http://pubs.acs.org/doi/10.1021/acs.nanolett.6b05409> (visited on 08/14/2018).
- [65] Sushobhan Joshi et al. “Boron Nitride on Cu(111): An Electronically Corrugated Monolayer”. In: *Nano Letters* 12.11 (2012), pp. 5821–5828. DOI: 10.1021/nl303170m. URL: <http://pubs.acs.org/doi/abs/10.1021/nl303170m>.
- [66] A.B. Preobrajenski, A.S. Vinogradov, and N. Mårtensson. “Monolayer of h-BN chemisorbed on Cu(111) and Ni(111): The role of the transition metal 3d states”. In: *Surface Science* 582.1 (May 2005), pp. 21–30. ISSN: 00396028. DOI: 10.1016/j.susc.2005.02.047. URL: <http://linkinghub.elsevier.com/retrieve/pii/S0039602805002426> (visited on 10/28/2014).
- [67] N. A. Vinogradov et al. “One-Dimensional Corrugation of the *h*-BN Monolayer on Fe(110)”. en. In: *Langmuir* 28.3 (Jan. 2012), pp. 1775–1781. ISSN: 0743-7463, 1520-5827. DOI: 10.1021/la2035642. URL: <http://pubs.acs.org/doi/10.1021/la2035642> (visited on 11/06/2018).
- [68] Fabian Schulz et al. “Epitaxial hexagonal boron nitride on Ir (111): A work function template”. In: *arXiv preprint arXiv:1404.7371* (2014). URL: <http://arxiv.org/abs/1404.7371> (visited on 10/15/2014).
- [69] Fabian Schulz et al. “Templated Self-Assembly and Local Doping of Molecules on Epitaxial Hexagonal Boron Nitride”. In: *ACS Nano* 7.12 (2013). PMID: 24152095,

- pp. 11121–11128. DOI: 10.1021/nn404840h. eprint: <https://doi.org/10.1021/nn404840h>. URL: <https://doi.org/10.1021/nn404840h>.
- [70] Jaime Gómez Díaz et al. “Hexagonal boron nitride on transition metal surfaces”. In: *Theoretical Chemistry Accounts* 132.4 (Apr. 2013). ISSN: 1432-881X, 1432-2234. DOI: 10.1007/s00214-013-1350-z. URL: <http://link.springer.com/10.1007/s00214-013-1350-z> (visited on 10/23/2014).
- [71] D. Usachov et al. “Experimental and computational insight into the properties of the lattice-mismatched structures: Monolayers of \$h\$-BN and graphene on Ir(111)”. In: *Phys. Rev. B* 86.15 (Oct. 2012), p. 155151. DOI: 10.1103/PhysRevB.86.155151. URL: <http://link.aps.org/doi/10.1103/PhysRevB.86.155151>.
- [72] Fabrizio Orlando et al. “Epitaxial Growth of Hexagonal Boron Nitride on Ir(111)”. In: *The Journal of Physical Chemistry C* 116.1 (2012), pp. 157–164. DOI: 10.1021/jp207571n. URL: <http://pubs.acs.org/doi/abs/10.1021/jp207571n>.
- [73] A. B. Preobrajenski et al. “Monolayer h-BN on lattice-mismatched metal surfaces: On the formation of the nanomesh”. In: *Chemical Physics Letters* 446.1 (2007), pp. 119–123. ISSN: 0009-2614. DOI: 10.1016/j.cplett.2007.08.028. URL: <http://www.sciencedirect.com/science/article/pii/S0009261407010998>.
- [74] Willi Auwärter et al. “Synthesis of One Monolayer of Hexagonal Boron Nitride on Ni(111) from B-Trichloroborazine (ClBNH)₃”. In: *Chemistry of Materials* 16.2 (Jan. 2004), pp. 343–345. ISSN: 0897-4756, 1520-5002. DOI: 10.1021/cm034805s. URL: <http://pubs.acs.org/doi/abs/10.1021/cm034805s> (visited on 10/15/2014).
- [75] W. Auwärter et al. “XPD and STM investigation of hexagonal boron nitride on Ni(111)”. In: *Surface Science* 429.1 (June 1999), pp. 229–236. ISSN: 00396028. DOI: 10.1016/S0039-6028(99)00381-7. URL: <http://linkinghub.elsevier.com/retrieve/pii/S0039602899003817> (visited on 10/23/2014).
- [76] A. Nagashima et al. “Electronic Structure of Monolayer Hexagonal Boron Nitride Physisorbed on Metal Surfaces”. In: *Phys. Rev. Lett.* 75.21 (Nov. 1995), pp. 3918–3921. DOI: 10.1103/PhysRevLett.75.3918. URL: <http://link.aps.org/doi/10.1103/PhysRevLett.75.3918>.
- [77] Martina Corso, Thomas Greber, and Jürg Osterwalder. “h-BN on Pd(110): a tunable system for self-assembled nanostructures?” In: *Surface Science* 577.2 (Mar. 2005), pp. L78–L84. ISSN: 00396028. DOI: 10.1016/j.susc.2005.01.015. URL: <http://linkinghub.elsevier.com/retrieve/pii/S0039602805000531> (visited on 08/14/2018).

- [78] M. Morscher et al. “Formation of single layer h-BN on Pd(111)”. In: *Surface Science* 600.16 (2006), pp. 3280–3284. ISSN: 0039-6028. DOI: <http://dx.doi.org/10.1016/j.susc.2006.06.016>. URL: <http://www.sciencedirect.com/science/article/pii/S0039602806007266>.
- [79] E. Ćavar et al. “A single h-BN layer on Pt(111)”. In: *Surface Science* 602.9 (May 2008), pp. 1722–1726. ISSN: 00396028. DOI: <10.1016/j.susc.2008.03.008>. URL: <http://linkinghub.elsevier.com/retrieve/pii/S0039602808001672> (visited on 08/14/2018).
- [80] Frank Müller, Klaus Stöwe, and Hermann Sachdev. “Symmetry versus Commensurability: Epitaxial Growth of Hexagonal Boron Nitride on Pt(111) From B-Trichloroborazine (ClBNH)₃”. In: *Chemistry of Materials* 17.13 (2005), pp. 3464–3467. DOI: <10.1021/cm048629e>. URL: <http://pubs.acs.org/doi/abs/10.1021/cm048629e>.
- [81] Guocai Dong et al. “How Boron Nitride Forms a Regular Nanomesh on Rh(111)”. In: *Phys. Rev. Lett.* 104.9 (Mar. 2010), p. 096102. DOI: <10.1103/PhysRevLett.104.096102>. URL: <http://link.aps.org/doi/10.1103/PhysRevLett.104.096102>.
- [82] T. Brugger et al. “Reversible switching of surface texture by hydrogen intercalation”. In: *Angewandte Chemie International Edition* 49.35 (Aug. 16, 2010), pp. 6120–6124. ISSN: 14337851. DOI: <10.1002/anie.201001064>. arXiv: <0911.1317>. URL: <http://arxiv.org/abs/0911.1317> (visited on 05/03/2017).
- [83] Simon Berner et al. “Boron Nitride Nanomesh: Functionality from a Corrugated Monolayer”. In: *Angewandte Chemie International Edition* 46.27 (July 2, 2007), pp. 5115–5119. ISSN: 14337851, 15213773. DOI: <10.1002/anie.200700234>. URL: <http://doi.wiley.com/10.1002/anie.200700234> (visited on 10/15/2014).
- [84] Martina Corso et al. “Boron Nitride Nanomesh”. In: *Science* 303.5655 (2004), pp. 217–220. DOI: <10.1126/science.1091979>. URL: <http://www.sciencemag.org/content/303/5655/217.abstract>.
- [85] Thomas Brugger et al. “Comparison of electronic structure and template function of single-layer graphene and a hexagonal boron nitride nanomesh on Ru(0001)”. In: *Phys. Rev. B* 79.4 (Jan. 2009), p. 045407. DOI: <10.1103/PhysRevB.79.045407>. URL: <http://link.aps.org/doi/10.1103/PhysRevB.79.045407>.
- [86] Andrii Goriachko et al. “Self-Assembly of a Hexagonal Boron Nitride Nanomesh on Ru(0001)”. In: *Langmuir* 23.6 (2007). STM, pp. 2928–2931. DOI: <10.1021/la062990t>. URL: <http://pubs.acs.org/doi/abs/10.1021/la062990t>.

- [87] Willi Auwärter. "Hexagonal boron nitride monolayers on metal supports: Versatile templates for atoms, molecules and nanostructures". en. In: *Surface Science Reports* (Nov. 2018). ISSN: 01675729. DOI: 10.1016/j.surfre.2018.10.001. URL: <https://linkinghub.elsevier.com/retrieve/pii/S0167572918300517> (visited on 11/06/2018).
- [88] Kailiang Zhang et al. "Two dimensional hexagonal boron nitride (2D-hBN): Synthesis, properties and applications". In: *Journal of Materials Chemistry C* 5.46 (2017). DOI: 10.1039/C7TC04300G. URL: https://www.researchgate.net/publication/321087148_Two_dimensional_hexagonal_boron_nitride_2D-hBN_Synthesis_properties_and_applications.
- [89] Klaus Hermann. "Periodic overlayers and moire patterns: theoretical studies of geometric properties". In: *Journal of Physics: Condensed Matter* 24.31 (2012), p. 314210. ISSN: 0953-8984. DOI: 10.1088/0953-8984/24/31/314210. URL: <http://stacks.iop.org/0953-8984/24/i=31/a=314210> (visited on 10/27/2015).
- [90] Silvan Roth et al. "Chemical Vapor Deposition and Characterization of Aligned and Incommensurate Graphene/Hexagonal Boron Nitride Heterostack on Cu(111)". In: *Nano Letters* 13.6 (June 12, 2013), pp. 2668–2675. ISSN: 1530-6984, 1530-6992. DOI: 10.1021/nl400815w. URL: <http://pubs.acs.org/doi/abs/10.1021/nl400815w> (visited on 10/28/2014).
- [91] Qiucheng Li et al. "Grain Boundary Structures and Electronic Properties of Hexagonal Boron Nitride on Cu(111)". In: *Nano Letters* 15.9 (Sept. 9, 2015), pp. 5804–5810. ISSN: 1530-6984. DOI: 10.1021/acs.nanolett.5b01852. URL: <http://dx.doi.org/10.1021/acs.nanolett.5b01852> (visited on 05/03/2017).
- [92] Tanglaw Roman and Axel Groß. "Periodic Density-Functional Calculations on Work-Function Change Induced by Adsorption of Halogens on Cu(111)". In: *Physical Review Letters* 110.15 (Apr. 12, 2013). ISSN: 0031-9007, 1079-7114. DOI: 10.1103/PhysRevLett.110.156804. URL: <https://link.aps.org/doi/10.1103/PhysRevLett.110.156804> (visited on 08/14/2018).
- [93] Joshi Sushobhan. "Hexagonal Boron Nitride Monolayers as Templates for Molecular Nanostructures". PhD thesis. München: Technische Universität München. 150 pp.
- [94] H. G. Zhang et al. "Assembly of iron phthalocyanine and pentacene molecules on a graphene monolayer grown on Ru(0001)". In: *Physical Review B* 84.24 (Dec. 19, 2011), p. 245436. DOI: 10.1103/PhysRevB.84.245436. URL: <https://link.aps.org/doi/10.1103/PhysRevB.84.245436> (visited on 05/03/2017).

- [95] Wi Hyoung Lee Bin Zhang. "Low-temperature chemical vapor deposition growth of graphene from toluene on electropolished copper foils." In: *ACS nano* 6.3 (2012), pp. 2471–6. ISSN: 1936-086X. DOI: 10.1021/nm204827h.
- [96] Ki Kang Kim et al. "Synthesis of Monolayer Hexagonal Boron Nitride on Cu Foil Using Chemical Vapor Deposition". In: *Nano Letters* 12.1 (Jan. 11, 2012), pp. 161–166. ISSN: 1530-6984. DOI: 10.1021/nl203249a. (Visited on 11/10/2014).
- [97] Huo Jinshan. "Electrochemical planarization of copper for microelectronic applications". In: (2004). URL: <http://digitalcommons.ohsu.edu/cgi/viewcontent.cgi?article=1208&context=etd> (visited on 12/12/2014).
- [98] Claire Antoine et al. *Alternative Approaches for Nb Superconducting Cavities Surface Treatment (Invited paper)*. Jan. 1999.
- [99] L. Lilje et al. "Improved surface treatment of the superconducting TESLA cavities". In: *Nuclear Instruments and Methods in Physics Research Section A: Accelerators, Spectrometers, Detectors and Associated Equipment* 516.2 (2004), pp. 213–227. ISSN: 0168-9002. DOI: <https://doi.org/10.1016/j.nima.2003.08.116>. URL: <http://www.sciencedirect.com/science/article/pii/S0168900203024318>.
- [100] E Schulz et al. "Engineering solutions for the electropolishing of multi-cell superconducting accelerator structures". In: (Aug. 2018).
- [101] Matt Stables et al. "Report on the Current Surface Characterisation Research Project for the UKRF Cavity Development Programme". In: (Aug. 2018). URL: https://www.researchgate.net/publication/237827266_Report_on_the_Current_Surface_Characterisation_Research_Project_for_the_UKRF_Cavity_Development_Programme.
- [102] Zhengtang Luo et al. "Effect of Substrate Roughness and Feedstock Concentration on Growth of Wafer-Scale Graphene at Atmospheric Pressure". In: *Chemistry of Materials* 23.6 (Mar. 22, 2011), pp. 1441–1447. ISSN: 0897-4756, 1520-5002. DOI: 10.1021/cm1028854. (Visited on 12/09/2014).
- [103] Jinshan (Jason) Huo. "Electrochemistry in ECMP". In: *Microelectronic Applications of Chemical Mechanical Planarization*. Ed. by Yuzhuo Li. Hoboken, New Jersey, USA: "John Wiley & Sons, Inc.", 2007, p. 760. ISBN: 9780470180907. DOI: 10.1002/9780470180907.
- [104] J. Huo, R. Solanki, and J. McAndrew. "Electrochemical planarization of Patterned Copper Films of Microelectronic Applications". In: *Heat Treating and Surface*

- Engineering*. Ed. by Narendra B. Dahotre et al. Indianapolis, Indiana, USA: ASM International, 2003. ISBN: 0-87170-797-7.
- [105] V. Palmieri et al. “Besides the standard Niobium bath chemical polishing”. In: 10 th W orkshop on RF Su percondutivity. Tsukuba , Japan, 2001. URL: <https://accelconf.web.cern.ch/accelconf/srf01/papers/pr016.pdf> (visited on 08/11/2018).
- [106] Yaping Wu et al. “Effects of thermally-induced changes of Cu grains on domain structure and electrical performance of CVD-grown graphene”. In: *Nanoscale* 8.2 (Dec. 23, 2015), pp. 930–937. ISSN: 2040-3372. DOI: 10.1039/C5NR06195D. URL: <http://pubs.rsc.org/en/content/articlelanding/2016/nr/c5nr06195d> (visited on 04/05/2016).
- [107] Ulrich Wendt and Gert Nolze. “Correlation between Crystal Orientation, Channeling Contrast and Topography during FIB Milling of Cu Studied by FIB, EBSD, SEM, and AFM”. In: *Practical Metallography* 44.5 (May 2007), pp. 236–238. ISSN: 0032-678X, 2195-8599. DOI: 10.3139/147.100340. URL: <http://www.hanser-elibrary.com/doi/abs/10.3139/147.100340> (visited on 09/27/2019).
- [108] C. Langlois et al. “Crystal orientation mapping via ion channeling: An alternative to EBSD”. In: *Ultramicroscopy* 157 (Oct. 2015), pp. 65–72. ISSN: 03043991. DOI: 10.1016/j.ultramic.2015.05.023. URL: <https://linkinghub.elsevier.com/retrieve/pii/S0304399115001345> (visited on 09/27/2019).
- [109] Piran R. Kidambi et al. “In Situ Observations during Chemical Vapor Deposition of Hexagonal Boron Nitride on Polycrystalline Copper”. In: *Chemistry of Materials* 26.22 (2014), pp. 6380–6392. ISSN: 0897-4756. DOI: 10.1021/cm502603n. URL: <http://dx.doi.org/10.1021/cm502603n> (visited on 12/15/2014).
- [110] *Graphene Supermarket :: Boron Nitride (BN) :: Single layer h-BN (Boron Nitride) film grown on copper foil: 2" x 1"*. Dec. 11, 2014. URL: <https://graphene-supermarket.com/Single-layer-h-BN-Boron-Nitride-film-grown-in-copper-foil-2-x-1.html> (visited on 12/11/2014).
- [111] G. Deroubaix and P. Marcus. “X-ray photoelectron spectroscopy analysis of copper and zinc oxides and sulphides”. In: *Surface and Interface Analysis* 18.1 (1992), pp. 39–46. ISSN: 1096-9918. DOI: 10.1002/sia.740180107. URL: <http://onlinelibrary.wiley.com/doi/10.1002/sia.740180107/abstract> (visited on 12/15/2014).

- [112] K. A. Simonov et al. “Controllable oxidation of h-BN monolayer on Ir(111) studied by core-level spectroscopies”. In: *Surface Science* 606.3 (2012), pp. 564–570. ISSN: 0039-6028. DOI: <http://dx.doi.org/10.1016/j.susc.2011.11.031>. URL: <http://www.sciencedirect.com/science/article/pii/S003960281100464X>.
- [113] Jose I. Urgel et al. “Controlling Coordination Reactions and Assembly on a Cu(111) Supported Boron Nitride Monolayer”. In: *Journal of the American Chemical Society* 137.7 (Feb. 25, 2015), pp. 2420–2423. ISSN: 0002-7863, 1520-5126. DOI: 10.1021/ja511611r. URL: <http://pubs.acs.org/doi/abs/10.1021/ja511611r> (visited on 09/09/2015).
- [114] U. Schlickum et al. “Metal-Organic Honeycomb Nanomeshes with Tunable Cavity Size”. In: *Nano Letters* 7.12 (Dec. 1, 2007), pp. 3813–3817. ISSN: 1530-6984. DOI: 10.1021/nl072466m. URL: <http://dx.doi.org/10.1021/nl072466m> (visited on 08/26/2016).
- [115] Paweł Przychodzeń et al. “Supramolecular coordination networks based on octacyanometalates: From structure to function”. In: *Coordination Chemistry Reviews*. 20th International Conference on Coordination and Bioinorganic Chemistry 250.17 (Sept. 2006), pp. 2234–2260. ISSN: 0010-8545. DOI: 10.1016/j.ccr.2006.01.026. URL: <http://www.sciencedirect.com/science/article/pii/S0010854506000348> (visited on 08/26/2016).
- [116] Ki Kang Kim et al. “Synthesis and Characterization of Hexagonal Boron Nitride Film as a Dielectric Layer for Graphene Devices”. In: *ACS Nano* 6.10 (Oct. 23, 2012), pp. 8583–8590. ISSN: 1936-0851, 1936-086X. DOI: 10.1021/nn301675f. (Visited on 12/01/2014).
- [117] Teresa M. Figueira-Duarte and Klaus Müllen. “Pyrene-Based Materials for Organic Electronics”. In: *Chemical Reviews* 111.11 (2011), pp. 7260–7314. DOI: 10.1021/cr100428a. URL: <https://doi.org/10.1021/cr100428a>.
- [118] Jarugu Narasimha Moorthy et al. “Steric Inhibition of π -Stacking: 1,3,6,8-Tetraarylpyrenes as Efficient Blue Emitters in Organic Light Emitting Diodes (OLEDs)”. In: *Organic Letters* 9.25 (2007). PMID: 17988140, pp. 5215–5218. DOI: 10.1021/o17023136. URL: <https://doi.org/10.1021/o17023136>.
- [119] Prashant Sonar et al. “1,3,6,8-tetrasubstituted pyrenes: solution-processable materials for application in organic electronics”. In: *Organic letters* 12.15 (Aug. 2010), pp. 3292–3295. ISSN: 1523-7060. DOI: 10.1021/o11007179. URL: <https://doi.org/10.1021/o11007179>.

- [120] Xing Feng et al. “Pyrene-Based Y-shaped Solid-State Blue Emitters: Synthesis, Characterization, and Photoluminescence”. In: *Chemistry – An Asian Journal* 7.12 (2012), pp. 2854–2863. DOI: 10.1002/asia.201200530. URL: <https://onlinelibrary.wiley.com/doi/abs/10.1002/asia.201200530>.
- [121] Zhengfeng Chang et al. “Efficient Electroluminescence from Excimers of 1,3,6,8-Tetrakis(3,5-dimethylphenyl)pyrene”. In: *Chemistry – An Asian Journal* 8.2 (2012), pp. 444–449. DOI: 10.1002/asia.201200932. URL: <https://onlinelibrary.wiley.com/doi/abs/10.1002/asia.201200932>.
- [122] K. R. Justin Thomas et al. “Pyrene-Fluorene Hybrids Containing Acetylene Linkage as Color-Tunable Emitting Materials for Organic Light-Emitting Diodes”. In: *The Journal of Organic Chemistry* 77.8 (2012), pp. 3921–3932. DOI: 10.1021/jo300285v. URL: <https://doi.org/10.1021/jo300285v>.
- [123] Holger Proehl et al. “Formation of Solid-State Excitons in Ultrathin Crystalline Films of PTCDA: From Single Molecules to Molecular Stacks”. In: *Phys. Rev. Lett.* 93 (9 Aug. 2004), p. 097403. DOI: 10.1103/PhysRevLett.93.097403. URL: <https://link.aps.org/doi/10.1103/PhysRevLett.93.097403>.
- [124] G. Bussetti et al. “Reflectance anisotropy spectroscopy: A probe to explore organic epitaxial growth”. In: *Journal of Vacuum Science & Technology A* 27.4 (2009), pp. 1029–1034. DOI: 10.1116/1.3155399. URL: <https://doi.org/10.1116/1.3155399>.
- [125] M. Schneider et al. “Morphology and trap luminescence in thin oligothiophene films on HOPG”. In: *Chemical Physics* 285 (Dec. 2002), pp. 345–353. DOI: 10.1016/S0301-0104(02)00819-4.
- [126] U. Heinemeyer et al. “Real-Time Changes in the Optical Spectrum of Organic Semiconducting Films and Their Thickness Regimes during Growth”. In: *Phys. Rev. Lett.* 104 (25 June 2010), p. 257401. DOI: 10.1103/PhysRevLett.104.257401. URL: <https://link.aps.org/doi/10.1103/PhysRevLett.104.257401>.
- [127] W. Gebauer et al. “Luminescence quenching of ordered π -conjugated molecules near a metal surface: Quaterthiophene and PTCDA on Ag(111)”. In: *Phys. Rev. B* 69 (15 Apr. 2004), p. 155431. DOI: 10.1103/PhysRevB.69.155431. URL: <https://link.aps.org/doi/10.1103/PhysRevB.69.155431>.
- [128] C. Chavy, C. Joachim, and A. Altibelli. “Interpretation of STM images: C60 on the gold (110) surface”. In: *Chemical Physics Letters* 214.6 (1993), pp. 569–575. ISSN: 0009-2614. DOI: [https://doi.org/10.1016/0009-2614\(93\)85685-H](https://doi.org/10.1016/0009-2614(93)85685-H). URL: <http://www.sciencedirect.com/science/article/pii/000926149385685H>.

- [129] Jascha Repp et al. “Molecules on Insulating Films: Scanning-Tunneling Microscopy Imaging of Individual Molecular Orbitals”. In: *Phys. Rev. Lett.* 94 (2 Jan. 2005), p. 026803. DOI: 10.1103/PhysRevLett.94.026803. URL: <https://link.aps.org/doi/10.1103/PhysRevLett.94.026803>.
- [130] Sebastian Koslowski et al. “Adsorption and electronic properties of pentacene on thin dielectric decoupling layers”. In: *Beilstein Journal of Nanotechnology* 8 (2017), pp. 1388–1395. ISSN: 2190-4286. DOI: 10.3762/bjnano.8.140.
- [131] Mao Kanno et al. “Electronic decoupling by h-BN layer between silicene and Cu(111): A DFT-based analysis”. In: *New Journal of Physics* 16.10 (2014), p. 105019. URL: <http://stacks.iop.org/1367-2630/16/i=10/a=105019>.
- [132] Juan M. Casas-Solvas, Joshua D. Howgego, and Anthony P. Davis. “Synthesis of substituted pyrenes by indirect methods”. In: *Org. Biomol. Chem.* 12 (2 2014), pp. 212–232. DOI: 10.1039/C3OB41993B. URL: <http://dx.doi.org/10.1039/C3OB41993B>.
- [133] Xing Feng et al. “Functionalization of Pyrene To Prepare Luminescent Materials—Typical Examples of Synthetic Methodology”. In: *Chemistry – A European Journal* 22.34 (2016), pp. 11898–11916. DOI: 10.1002/chem.201600465. URL: <https://onlinelibrary.wiley.com/doi/abs/10.1002/chem.201600465>.
- [134] Tobias Kaposi et al. “Supramolecular Spangling, Crocheting, and Knitting of Functionalized Pyrene Molecules on a Silver Surface”. In: *ACS nano* 10.8 (Aug. 2016), pp. 7665–7674. ISSN: 1936-0851. DOI: 10.1021/acsnano.6b02989. URL: <https://doi.org/10.1021/acsnano.6b02989>.
- [135] Ryohei Kurata et al. “Diaryl amino- and Diarylboryl-Substituted Donor–Acceptor Pyrene Derivatives: Influence of Substitution Pattern on Their Photophysical Properties”. In: *The Journal of Organic Chemistry* 82.10 (2017), pp. 5111–5121. DOI: 10.1021/acs.joc.7b00315. URL: <https://doi.org/10.1021/acs.joc.7b00315>.
- [136] Sushobhan Joshi et al. “Control of Molecular Organization and Energy Level Alignment by an Electronically Nanopatterned Boron Nitride Template”. In: *ACS Nano* 8.1 (2014). PMID: 24328081, pp. 430–442. DOI: 10.1021/nn406024m. eprint: <https://doi.org/10.1021/nn406024m>. URL: <https://doi.org/10.1021/nn406024m>.
- [137] Andrew G. Crawford et al. “Experimental and Theoretical Studies of the Photophysical Properties of 2- and 2,7-Functionalized Pyrene Derivatives”. In: *Journal of the American Chemical Society* 133.34 (2011). PMID: 21751803, pp. 13349–13362. DOI: 10.1021/ja2006862. URL: <https://doi.org/10.1021/ja2006862>.

- [138] Yeon Ok Lee et al. “Enhanced Electrogenerated Chemiluminescence of Phenylethynylpyrene Derivatives: Use of Weakly Electron-Donating Group as a Substituent”. In: *The Journal of Organic Chemistry* 77.24 (2012). PMID: 22881841, pp. 11007–11013. DOI: 10.1021/jo3010974. URL: <https://doi.org/10.1021/jo3010974>.
- [139] Hajime Maeda et al. “Alkynylpyrenes as Improved Pyrene-Based Biomolecular Probes with the Advantages of High Fluorescence Quantum Yields and Long Absorption/Emission Wavelengths”. In: *Chemistry – A European Journal* 12.3 (2006), pp. 824–831. DOI: 10.1002/chem.200500638. URL: <https://onlinelibrary.wiley.com/doi/abs/10.1002/chem.200500638>.
- [140] Tuan Anh Pham et al. “Self-assembly of pyrene derivatives on Au(111): substituent effects on intermolecular interactions”. In: 50.91 (Oct. 21, 2014), pp. 14089–14092. ISSN: 1364-548X. DOI: 10.1039/C4CC02753A. URL: <http://pubs.rsc.org/en/content/articlelanding/2014/cc/c4cc02753a> (visited on 02/21/2017).
- [141] Manfred Matena et al. “Aggregation and Contingent Metal/Surface Reactivity of 1,3,8,10-Tetraazaperopyrene (TAPP) on Cu(111)”. In: *Chemistry – A European Journal* 16.7 (Feb. 15, 2010), pp. 2079–2091. ISSN: 1521-3765. DOI: 10.1002/chem.200902596. URL: <http://onlinelibrary.wiley.com/doi/10.1002/chem.200902596/abstract> (visited on 02/22/2017).
- [142] Ada Della Pia et al. “Anomalous Coarsening Driven by Reversible Charge Transfer at Metal–Organic Interfaces”. In: *ACS Nano* 8.12 (Dec. 23, 2014), pp. 12356–12364. ISSN: 1936-0851. DOI: 10.1021/nn505063w. URL: <http://dx.doi.org/10.1021/nn505063w> (visited on 02/21/2017).
- [143] Tuan Anh Pham et al. “Comparing Ullmann Coupling on Noble Metal Surfaces: On-Surface Polymerization of 1,3,6,8-Tetrabromopyrene on Cu(111) and Au(111)”. In: *Chemistry – A European Journal* 22.17 (Apr. 18, 2016), pp. 5937–5944. ISSN: 1521-3765. DOI: 10.1002/chem.201504946. URL: <http://onlinelibrary.wiley.com/doi/10.1002/chem.201504946/abstract> (visited on 02/21/2017).
- [144] Emmanuel Arras et al. “Nature of the attractive interaction between proton acceptors and organic ring systems”. In: *Phys. Chem. Chem. Phys.* 14 (46 2012), pp. 15995–16001. DOI: 10.1039/C2CP42293J. URL: <http://dx.doi.org/10.1039/C2CP42293J>.
- [145] Liwei Liu et al. “Interplay between Energy-Level Position and Charging Effect of Manganese Phthalocyanines on an Atomically Thin Insulator”. In: *ACS Nano* 9.10 (2015). PMID: 26390030, pp. 10125–10132. DOI: 10.1021/acsnano.5b03741. URL: <https://doi.org/10.1021/acsnano.5b03741>.

- [146] Avijit Kumar, Kaustuv Banerjee, and Peter Liljeroth. “Molecular assembly on two-dimensional materials”. In: *Nanotechnology* 28.8 (2017), p. 082001. URL: <http://stacks.iop.org/0957-4484/28/i=8/a=082001>.
- [147] Matthias Krieg et al. “Construction of an Internally B_3N_3 -Doped Nanographene Molecule”. In: *Angewandte Chemie International Edition* 54.28 (2015), pp. 8284–8286. DOI: [10.1002/anie.201412165](https://doi.org/10.1002/anie.201412165).
- [148] F. Cicullo et al. “A Quasi-Free-Standing Single Layer of a B_3N_3 -Doped Nanographene Molecule Deposited on Au(111) Single Crystals”. In: *The Journal of Physical Chemistry C* 120.31 (2016), pp. 17645–17651. DOI: [10.1021/acs.jpcc.6b06237](https://doi.org/10.1021/acs.jpcc.6b06237).
- [149] Jacopo Dosso et al. “Synthesis and Optoelectronic Properties of Hexa- *peri* - hexabenzoborazinocoronene”. In: *Angewandte Chemie* 129.16 (Apr. 10, 2017), pp. 4554–4558. ISSN: 00448249. DOI: [10.1002/ange.201700907](https://doi.org/10.1002/ange.201700907). URL: <http://doi.wiley.com/10.1002/ange.201700907> (visited on 08/16/2018).
- [150] Paulo V. C. Medeiros, G. K. Gueorguiev, and S. Stafström. “Benzene, coronene, and circumcoronene adsorbed on gold, and a gold cluster adsorbed on graphene: Structural and electronic properties”. In: *Physical Review B* 85.20 (May 14, 2012). ISSN: 1098-0121, 1550-235X. DOI: [10.1103/PhysRevB.85.205423](https://doi.org/10.1103/PhysRevB.85.205423). URL: <https://link.aps.org/doi/10.1103/PhysRevB.85.205423> (visited on 02/28/2019).
- [151] Markus Lackinger et al. “Coronene on Ag(111) Investigated by LEED and STM in UHV”. In: *The Journal of Physical Chemistry B* 106.17 (May 2002), pp. 4482–4485. ISSN: 1520-6106, 1520-5207. DOI: [10.1021/jp014275s](https://doi.org/10.1021/jp014275s). URL: <https://pubs.acs.org/doi/10.1021/jp014275s> (visited on 02/28/2019).
- [152] Paolo Samorí et al. “Epitaxial Composite Layers of Electron Donors and Acceptors from Very Large Polycyclic Aromatic Hydrocarbons”. In: *Journal of the American Chemical Society* 124.32 (Aug. 2002), pp. 9454–9457. ISSN: 0002-7863, 1520-5126. DOI: [10.1021/ja020323q](https://doi.org/10.1021/ja020323q). URL: <https://pubs.acs.org/doi/10.1021/ja020323q> (visited on 02/28/2019).
- [153] A.W. McKinnon, M.E. Welland, and St. John Dixon Warren. “Observation of the ordered growth of coronene on Ag(111): a scanning tunnelling microscopy study of vacuum deposited molecules”. In: *Thin Solid Films* 257.1 (Feb. 1995), pp. 63–67. ISSN: 00406090. DOI: [10.1016/0040-6090\(94\)06345-1](https://doi.org/10.1016/0040-6090(94)06345-1). URL: [http://linkinghub.elsevier.com/retrieve/pii/0040609094063451](https://linkinghub.elsevier.com/retrieve/pii/0040609094063451) (visited on 02/28/2019).

- [154] U. Zimmermann and N. Karl. “Epitaxial growth of coronene and hexa-peri-benzocoronene on MoS₂(0001) and graphite (0001): a LEED study of molecular size effects”. In: *Surface Science* 268.1 (Jan. 1992), pp. 296–306. ISSN: 00396028. DOI: 10.1016/0039-6028(92)90969-D. URL: <http://linkinghub.elsevier.com/retrieve/pii/003960289290969D> (visited on 02/28/2019).
- [155] H. Glowatzki et al. “Hexa- *peri* -hexabenzocoronene on Ag(111): Monolayer/Multilayer Transition of Molecular Orientation and Electronic Structure”. In: *The Journal of Physical Chemistry C* 112.5 (Feb. 2008), pp. 1570–1574. ISSN: 1932-7447, 1932-7455. DOI: 10.1021/jp0774894. URL: <https://pubs.acs.org/doi/10.1021/jp0774894> (visited on 02/28/2019).
- [156] Takashi Yokoyama et al. “Selective assembly on a surface of supramolecular aggregates with controlled size and shape”. In: *Nature* 413 (Oct. 11, 2001), p. 619. URL: <http://dx.doi.org/10.1038/35098059>.
- [157] Alan R. Battersby. “Tetrapyrroles: the pigments of life”. In: *Natural Product Reports* 17.6 (2000), pp. 507–526. ISSN: 02650568, 14604752. DOI: 10.1039/b002635m. URL: <http://xlink.rsc.org/?DOI=b002635m> (visited on 08/21/2018).
- [158] Willi Auwärter et al. “Porphyrins at interfaces”. In: *Nature Chemistry* 7.2 (Feb. 2015), pp. 105–120. ISSN: 1755-4330. DOI: 10.1038/nchem.2159. URL: <http://www.nature.com/nchem/journal/v7/n2/full/nchem.2159.html> (visited on 11/12/2015).
- [159] Willi Auwärter et al. “Controlled Metalation of Self-Assembled Porphyrin Nanoarrays in Two Dimensions”. In: *ChemPhysChem* 8.2 (Feb. 2, 2007), pp. 250–254. ISSN: 14394235, 14397641. DOI: 10.1002/cphc.200600675. URL: <http://doi.wiley.com/10.1002/cphc.200600675> (visited on 08/21/2018).
- [160] Katharina Diller et al. “In vacuo interfacial tetrapyrrole metallation”. In: *Chemical Society Reviews* 45.6 (2016), pp. 1629–1656. ISSN: 0306-0012, 1460-4744. DOI: 10.1039/C5CS00207A. URL: <http://xlink.rsc.org/?DOI=C5CS00207A> (visited on 08/21/2018).
- [161] William P. Lustig et al. “Metal–organic frameworks: functional luminescent and photonic materials for sensing applications”. In: *Chem. Soc. Rev.* 46 (11 2017), pp. 3242–3285. DOI: 10.1039/C6CS00930A. URL: <http://dx.doi.org/10.1039/C6CS00930A>.

- [162] Francesca Moresco et al. “Conformational Changes of Single Molecules Induced by Scanning Tunneling Microscopy Manipulation: A Route to Molecular Switching”. In: *Physical Review Letters* 86.4 (Jan. 22, 2001), pp. 672–675. DOI: 10.1103/PhysRevLett.86.672. URL: <http://link.aps.org/doi/10.1103/PhysRevLett.86.672> (visited on 11/12/2015).
- [163] M. Stark et al. “Massive conformational changes during thermally induced self-metalation of 2H-tetrakis-(3,5-di-tert-butyl)-phenylporphyrin on Cu(111)”. In: *Chemical Communications* 50.71 (July 14, 2014), p. 10225. ISSN: 1359-7345, 1364-548X. DOI: 10.1039/C4CC03708A. URL: <http://xlink.rsc.org/?DOI=C4CC03708A> (visited on 11/12/2015).
- [164] Ch. Loppacher et al. “Direct Determination of the Energy Required to Operate a Single Molecule Switch”. In: *Physical Review Letters* 90.6 (Feb. 14, 2003). ISSN: 0031-9007, 1079-7114. DOI: 10.1103/PhysRevLett.90.066107. URL: <https://link.aps.org/doi/10.1103/PhysRevLett.90.066107> (visited on 08/15/2018).
- [165] Stefanie Ditze et al. “On the Energetics of Conformational Switching of Molecules at and Close to Room Temperature”. In: *Journal of the American Chemical Society* 136.4 (Jan. 29, 2014), pp. 1609–1616. ISSN: 0002-7863. DOI: 10.1021/ja411884p. URL: <http://dx.doi.org/10.1021/ja411884p> (visited on 11/12/2015).
- [166] Tuan Anh Pham et al. “Heat-induced formation of one-dimensional coordination polymers on Au(111): an STM study”. In: *Chemical Communications* 51.77 (2015), pp. 14473–14476. ISSN: 1359-7345, 1364-548X. DOI: 10.1039/C5CC04940G. URL: <http://xlink.rsc.org/?DOI=C5CC04940G> (visited on 08/21/2018).
- [167] Puneet Mishra et al. “Current-Driven Supramolecular Motor with In Situ Surface Chiral Directionality Switching”. In: *Nano Letters* 15.7 (July 8, 2015), pp. 4793–4798. ISSN: 1530-6984, 1530-6992. DOI: 10.1021/acs.nanolett.5b01908. URL: <http://pubs.acs.org/doi/abs/10.1021/acs.nanolett.5b01908> (visited on 07/13/2015).
- [168] D. Ecija et al. “Dynamics and thermal stability of surface-confined metal–organic chains”. In: *Surface Science* 643 (Jan. 2016), pp. 91–97. ISSN: 00396028. DOI: 10.1016/j.susc.2015.08.013. URL: <http://linkinghub.elsevier.com/retrieve/pii/S0039602815002332> (visited on 08/21/2018).
- [169] William L. Jorgensen and Lionel Salem. *“The Organic Chemist’s Book of Orbitals”*. New York: Academic Press, 1973. ISBN: 0-12-390250-9.

- [170] Kazuaki Kato and Hans-Jörg Schneider. “Dispersive Effects in Chemomechanical Reactions with Polyallylamine-Derived Hydrogels”. In: *European Journal of Organic Chemistry* 2008.8 (Mar. 1, 2008), pp. 1378–1382. ISSN: 1099-0690. DOI: 10.1002/ejoc.200700850. URL: <http://onlinelibrary.wiley.com/doi/10.1002/ejoc.200700850/abstract> (visited on 04/14/2016).
- [171] Daniel Heim et al. “Surface-Assisted Assembly of Discrete Porphyrin-Based Cyclic Supramolecules”. In: *Nano Letters* 10.1 (Jan. 13, 2010), pp. 122–128. ISSN: 1530-6984. DOI: 10.1021/nl9029994. URL: <http://dx.doi.org/10.1021/nl9029994> (visited on 04/14/2016).
- [172] Daniel Heim et al. “Self-Assembly of Flexible One-Dimensional Coordination Polymers on Metal Surfaces”. In: *Journal of the American Chemical Society* 132.19 (May 19, 2010), pp. 6783–6790. ISSN: 0002-7863. DOI: 10.1021/ja1010527. URL: <http://dx.doi.org/10.1021/ja1010527> (visited on 04/14/2016).
- [173] Geoffrey Rojas et al. “Surface state engineering of molecule–molecule interactions”. In: *Physical Chemistry Chemical Physics* 14.14 (2012), p. 4971. ISSN: 1463-9076, 1463-9084. DOI: 10.1039/c2cp40254h. URL: <http://xlink.rsc.org/?DOI=c2cp40254h> (visited on 08/29/2018).
- [174] Stefano Gottardi et al. “Cyano-Functionalized Triarylamines on Au(111): Competing Intermolecular versus Molecule/Substrate Interactions”. In: *Advanced Materials Interfaces* 1.1 (Feb. 2014), p. 1300025. ISSN: 21967350. DOI: 10.1002/admi.201300025. URL: <http://doi.wiley.com/10.1002/admi.201300025> (visited on 01/18/2018).
- [175] Cristian Iacovita et al. “Controlling the Dimensionality and Structure of Supramolecular Porphyrin Assemblies by their Functional Substituents: Dimers, Chains, and Close-Packed 2D Assemblies”. In: *Chemistry - A European Journal* 18.46 (Nov. 12, 2012), pp. 14610–14613. ISSN: 09476539. DOI: 10.1002/chem.201201037. URL: <http://doi.wiley.com/10.1002/chem.201201037> (visited on 07/13/2015).
- [176] Lihua Cui et al. “Self-assembly polymorphism of 2,7-bis-nonyloxy-9-fluorenone: solvent induced the diversity of intermolecular dipole–dipole interactions”. In: *Phys. Chem. Chem. Phys.* 17 (5 2015), pp. 3627–3636. DOI: 10.1039/C4CP04773G. URL: <http://dx.doi.org/10.1039/C4CP04773G>.
- [177] Li Xu et al. “Dipole-Controlled Self-Assembly of 2,7-Bis(n-alkoxy)-9-fluorenone: Odd–Even and Chain-Length Effects”. In: *The Journal of Physical Chemistry C* 117.24 (2013), pp. 12707–12714. DOI: 10.1021/jp403881t. eprint: <https://doi.org/10.1021/jp403881t>. URL: <https://doi.org/10.1021/jp403881t>.

- [178] Li Xu et al. “Two-Dimensional Self-Assembled Molecular Structures Formed by the Competition of van der Waals Forces and Dipole–Dipole Interactions”. In: *The Journal of Physical Chemistry C* 116.1 (2012), pp. 1061–1069. DOI: 10.1021/jp210000e. eprint: <https://doi.org/10.1021/jp210000e>. URL: <https://doi.org/10.1021/jp210000e>.
- [179] Yi Hu et al. “Structural transition control between dipole–dipole and hydrogen bonds induced chirality and achirality”. In: *CrystEngComm* 18 (17 2016), pp. 3019–3032. DOI: 10.1039/C5CE02321A. URL: <http://dx.doi.org/10.1039/C5CE02321A>.
- [180] Yi Hu et al. “Effects of alkyl chain number and position on 2D self-assemblies”. In: *RSC Adv.* 7 (51 2017), pp. 32391–32398. DOI: 10.1039/C7RA05811J. URL: <http://dx.doi.org/10.1039/C7RA05811J>.
- [181] Laura E Heller et al. “Self-assembly of isomeric monofunctionalized thiophenes”. In: *Langmuir : the ACS journal of surfaces and colloids* 28.42 (Oct. 2012), pp. 14855–14859. ISSN: 0743-7463. DOI: 10.1021/la3031733. URL: <https://doi.org/10.1021/la3031733>.
- [182] Yanhu Wei et al. “Dipolar Control of Monolayer Morphology: Spontaneous SAM Patterning”. In: *Journal of the American Chemical Society* 128.41 (2006). PMID: 17031941, pp. 13362–13363. DOI: 10.1021/ja065338t. eprint: <https://doi.org/10.1021/ja065338t>. URL: <https://doi.org/10.1021/ja065338t>.
- [183] Donna A. Kunkel et al. “Self-assembly of strongly dipolar molecules on metal surfaces”. In: *The Journal of Chemical Physics* 142.10 (2015), p. 101921. DOI: 10.1063/1.4907943. eprint: <https://doi.org/10.1063/1.4907943>. URL: <https://doi.org/10.1063/1.4907943>.
- [184] Zhongcheng Mu et al. “Effect of Intermolecular Dipole-Dipole Interactions on Interfacial Supramolecular Structures of C₃-Symmetric Hexa-peri-hexabenzocoronene Derivatives”. In: *Langmuir* 27.4 (2011). PMID: 21090755, pp. 1314–1318. DOI: 10.1021/la103921e. eprint: <https://doi.org/10.1021/la103921e>. URL: <https://doi.org/10.1021/la103921e>.
- [185] Melvin S. Newman and Daniel Lednicer. “The Synthesis and Resolution of Hexahelicene”. In: *Journal of the American Chemical Society* 78.18 (Sept. 1, 1956), pp. 4765–4770. ISSN: 0002-7863. DOI: 10.1021/ja01599a060. URL: <http://dx.doi.org/10.1021/ja01599a060> (visited on 06/01/2016).

- [186] H. Rau and F. Totter. “Exciplex and ion pair quenching in a chiral hexahelicene-amine system”. In: *Journal of Photochemistry and Photobiology A: Chemistry* 63.3 (1992), pp. 337–347. ISSN: 1010-6030. DOI: [https://doi.org/10.1016/1010-6030\(92\)85199-5](https://doi.org/10.1016/1010-6030(92)85199-5). URL: <http://www.sciencedirect.com/science/article/pii/1010603092851995>.
- [187] E. Vander Donckt et al. “Fluorescence of the helicenes”. In: *Chemical Physics Letters* 2.6 (1968), pp. 409–410. ISSN: 0009-2614. DOI: [https://doi.org/10.1016/0009-2614\(68\)80041-7](https://doi.org/10.1016/0009-2614(68)80041-7). URL: <http://www.sciencedirect.com/science/article/pii/0009261468800417>.
- [188] Matthias Treier et al. “An aromatic coupling motif for two-dimensional supramolecular architectures”. In: *Chem. Commun.* (38 2008), pp. 4555–4557. DOI: <10.1039/B809618J>. URL: <http://dx.doi.org/10.1039/B809618J>.
- [189] Matthew Forster et al. “Probing Conformers and Adsorption Footprints at the Single-Molecule Level in a Highly Organized Amino Acid Assembly of (S)-Proline on Cu(110)”. In: *Journal of the American Chemical Society* 131.29 (2009). PMID: 19580280, pp. 10173–10181. DOI: <10.1021/ja9020364>. eprint: <https://doi.org/10.1021/ja9020364>. URL: <https://doi.org/10.1021/ja9020364>.
- [190] Lanxia Cheng. “Role of Hydrogen Bonding in the Formation of Adenine Chains on Cu(110) Surfaces”. In: *Materials* 9.12 (2016). ISSN: 1996-1944. DOI: <10.3390/ma9121016>. URL: <http://www.mdpi.com/1996-1944/9/12/1016>.
- [191] Caroline Rabot et al. “Self-Assembly of Meta-Aminobenzoate on Cu(110)”. In: *Langmuir* 25.10 (2009), pp. 5504–5508. DOI: <10.1021/la900056n>. eprint: <https://doi.org/10.1021/la900056n>. URL: <https://doi.org/10.1021/la900056n>.
- [192] Johannes Seibel et al. “Chiral Conflict among Different Helicenes Suppresses Formation of One Enantiomorph in 2D Crystallization”. In: *Journal of the American Chemical Society* 135.20 (2013). PMID: 23638639, pp. 7434–7437. DOI: <10.1021/ja402012j>. eprint: <https://doi.org/10.1021/ja402012j>. URL: <https://doi.org/10.1021/ja402012j>.
- [193] Aneliia Shchyrba et al. “Chirality Transfer in 1D Self-Assemblies: Influence of H-Bonding vs Metal Coordination between Dicyano[7]helicene Enantiomers”. In: *Journal of the American Chemical Society* 135.41 (2013). PMID: 24090281, pp. 15270–15273. DOI: <10.1021/ja407315f>. eprint: <https://doi.org/10.1021/ja407315f>. URL: <https://doi.org/10.1021/ja407315f>.

- [194] Meike Stöhr et al. “Self-Assembly and Two-Dimensional Spontaneous Resolution of Cyano-Functionalized [7]Helicenes on Cu(111)”. In: *Angewandte Chemie International Edition* 50.42 (2011), pp. 9982–9986. DOI: 10.1002/anie.201102627. eprint: <https://onlinelibrary.wiley.com/doi/pdf/10.1002/anie.201102627>. URL: <https://onlinelibrary.wiley.com/doi/abs/10.1002/anie.201102627>.
- [195] Karl-Heinz Ernst. “Stereochemical Recognition of Helicenes on Metal Surfaces”. In: *Accounts of Chemical Research* 49.6 (2016). PMID: 27251099, pp. 1182–1190. DOI: 10.1021/acs.accounts.6b00110. eprint: <https://doi.org/10.1021/acs.accounts.6b00110>. URL: <https://doi.org/10.1021/acs.accounts.6b00110>.
- [196] Johannes Seibel, Manfred Parschau, and Karl-Heinz Ernst. “Two-Dimensional Crystallization of Enantiopure and Racemic Heptahelicene on Ag(111) and Au(111)”. In: *The Journal of Physical Chemistry C* 118.50 (2014), pp. 29135–29141. DOI: 10.1021/jp504673g. eprint: <https://doi.org/10.1021/jp504673g>. URL: <https://doi.org/10.1021/jp504673g>.
- [197] Johannes Seibel, Manfred Parschau, and Karl-Heinz Ernst. “From Homochiral Clusters to Racemate Crystals: Viable Nuclei in 2D Chiral Crystallization”. In: *Journal of the American Chemical Society* 137.25 (2015). PMID: 26069901, pp. 7970–7973. DOI: 10.1021/jacs.5b02262. eprint: <https://doi.org/10.1021/jacs.5b02262>. URL: <https://doi.org/10.1021/jacs.5b02262>.
- [198] Manfred Parschau, Roman Fasel, and Karl-Heinz Ernst. “Coverage and Enantiomeric Excess Dependent Enantiomorphism in Two-Dimensional Molecular Crystals”. In: *Crystal Growth & Design* 8.6 (2008), pp. 1890–1896. DOI: 10.1021/cg701100r. eprint: <https://doi.org/10.1021/cg701100r>. URL: <https://doi.org/10.1021/cg701100r>.
- [199] Roman Fasel, Manfred Parschau, and Karl-Heinz Ernst. “Amplification of chirality in two-dimensional enantiomorphous lattices”. In: *nature* 439 (2006), pp. 449–452. DOI: 10.1038/nature04419. URL: <https://doi.org/10.1038/nature04419>.
- [200] Johannes Seibel, Laura Zoppi, and Karl-Heinz Ernst. “2D conglomerate crystallization of heptahelicene”. In: *Chem. Commun.* 50 (63 2014), pp. 8751–8753. DOI: 10.1039/C4CC03574G. URL: <http://dx.doi.org/10.1039/C4CC03574G>.
- [201] K.-H. Ernst et al. “Two-dimensional separation of [7]helicene enantiomers on Cu(111)”. In: *Chirality* 13.10 (2001), pp. 675–678. DOI: 10.1002/chir.10006. eprint: <https://onlinelibrary.wiley.com/doi/pdf/10.1002/chir.10006>. URL: <https://onlinelibrary.wiley.com/doi/abs/10.1002/chir.10006>.

- [202] Roman Fasel, Manfred Parschau, and Karl-Heinz Ernst. “Chirality Transfer from Single Molecules into Self-Assembled Monolayers”. In: *Angewandte Chemie International Edition* 42.42 (2003), pp. 5178–5181. DOI: 10.1002/anie.200352232. eprint: <https://onlinelibrary.wiley.com/doi/pdf/10.1002/anie.200352232>. URL: <https://onlinelibrary.wiley.com/doi/abs/10.1002/anie.200352232>.
- [203] Manfred Parschau, Ursula Ellerbeck, and Karl-Heinz Ernst. “Chirality transfer by epitaxial mismatch in multi-layered homochiral molecular films”. In: *Colloids and Surfaces A: Physicochemical and Engineering Aspects* 354.1 (2010). Gibbs and Langmuir Surface Layers Thermodynamic, Kinetics and Structure, pp. 240–245. ISSN: 0927-7757. DOI: <https://doi.org/10.1016/j.colsurfa.2009.06.008>. URL: <http://www.sciencedirect.com/science/article/pii/S0927775709003641>.
- [204] Isabel Fernández Torrente, Katharina J Franke, and Jose Ignacio Pascual. “Spectroscopy of C₆₀ single molecules: the role of screening on energy level alignment”. In: *Journal of Physics: Condensed Matter* 20.18 (2008), p. 184001. URL: <http://stacks.iop.org/0953-8984/20/i=18/a=184001>.
- [205] Christian Wäckerlin et al. “Surface-assisted diastereoselective Ullmann coupling of bishelicenes”. In: *Chem. Commun.* 52 (86 2016), pp. 12694–12697. DOI: 10.1039/C6CC05849C. URL: <http://dx.doi.org/10.1039/C6CC05849C>.
- [206] R. Fasel et al. “Orientation of chiral heptahelicene C₃₀H₁₈ on copper surfaces: An x-ray photoelectron diffraction study”. In: *The Journal of Chemical Physics* 115.2 (2001), pp. 1020–1027. DOI: 10.1063/1.1377886. eprint: <https://doi.org/10.1063/1.1377886>. URL: <https://doi.org/10.1063/1.1377886>.
- [207] Yupeng Li et al. “Tight intermolecular packing through supramolecular interactions in crystals of cyano substituted oligo(para-phenylene vinylene): a key factor for aggregation-induced emission”. In: *Chem. Commun.* (3 2007), pp. 231–233. DOI: 10.1039/B612732K. URL: <http://dx.doi.org/10.1039/B612732K>.
- [208] U. Schlickum et al. “Chiral Kagomé Lattice from Simple Ditopic Molecular Bricks”. In: *Journal of the American Chemical Society* 130.35 (2008). PMID: 18693686, pp. 11778–11782. DOI: 10.1021/ja8028119. URL: <https://doi.org/10.1021/ja8028119>.
- [209] Ralph Koitz et al. “Structural and electronic properties of a large-scale Moiré pattern of hexagonal boron nitride on Cu(111) studied with density functional theory”. In: *Nanoscale* 5 (12 2013), pp. 5589–5595. DOI: 10.1039/C3NR00709J. URL: <http://dx.doi.org/10.1039/C3NR00709J>.

- [210] Andreas Riemann. “Ionic Insulators on Vicinal Metal Surfaces”. PhD thesis. Freie Universität Berlin, Freie Universität Berlin, Germany, 2002. URL: <https://refubium.fu-berlin.de/handle/fub188/624> (visited on 07/27/2015).
- [211] *PyProbe Web interface 0.2 Alpha*. Mar. 1, 2019. URL: <http://ppr.fzu.cz/> (visited on 03/01/2019).
- [212] Prokop Hapala et al. “Origin of High-Resolution IETS-STM Images of Organic Molecules with Functionalized Tips”. In: *Physical Review Letters* 113.22 (Nov. 25, 2014). ISSN: 0031-9007, 1079-7114. DOI: 10.1103/PhysRevLett.113.226101. URL: <https://link.aps.org/doi/10.1103/PhysRevLett.113.226101> (visited on 03/01/2019).
- [213] Prokop Hapala et al. “Mechanism of high-resolution STM/AFM imaging with functionalized tips”. In: *Physical Review B* 90.8 (Aug. 19, 2014). ISSN: 1098-0121, 1550-235X. DOI: 10.1103/PhysRevB.90.085421. URL: <https://link.aps.org/doi/10.1103/PhysRevB.90.085421> (visited on 03/01/2019).
- [214] Xiao-Ye Wang et al. “Heteroatom-Doped Perihexacene from a Double Helicene Precursor: On-Surface Synthesis and Properties”. In: *Journal of the American Chemical Society* 139.13 (2017). PMID: 28335591, pp. 4671–4674. DOI: 10.1021/jacs.7b02258. URL: <https://doi.org/10.1021/jacs.7b02258>.
- [215] Oleksandr Stetsovych et al. “From helical to planar chirality by on-surface chemistry”. In: *Nature Chemistry* 9 (2016), pp. 213–218. URL: <https://doi.org/10.1038/nchem.2662>.
- [216] K.-H Ernst et al. “Adsorption of helical aromatic molecules: heptahelicene on Ni(111)”. In: *Surface Science* 530.3 (2003), pp. 195–202. ISSN: 0039-6028. DOI: [https://doi.org/10.1016/S0039-6028\(03\)00489-8](https://doi.org/10.1016/S0039-6028(03)00489-8). URL: <http://www.sciencedirect.com/science/article/pii/S0039602803004898>.